Ferdowsi University of Mashhad

Journal of Agricultural Machinery

Iranian Society of Mechanical Engineers (ISME)

Vol. 14 No. 1

2024

ISSN: 2228-6829

Contents

Journal of Agricultural Machinery

Vol. 14 **No. 1** **2024**

Published by: Ferdowsi University of Mashhad, (College of Agriculture), Iran

Publisher: Ferdowsi University of Mashhad

Address: College of Agriculture, Ferdowsi University of Mashhad, Iran

P.O. BOX: 91775-1163

Fax: +98-05138787430

E-Mail: jame@um.ac.ir

Web Site: http://jame.um.ac.ir

Contents

Journal of Agricultural Machinery

Homepage: https://jame.um.ac.ir

Research Article
Vol. 14, No. 1, Spring 2024, p. 1-13

Dynamic Model of Hip and Ankle Joints Loading during Working with a Motorized Backpack Sprayer

S. Karimi Avargani[1], A. Maleki[2*], Sh. Besharati[3], R. Ebrahimi[4]

1- M.Sc. Student of Mechanical Engineering of Biosystems Department, Faculty of Agriculture, Shahrekord University, Shahrekord, Iran
2- Associate Professor of Mechanical Engineering of Biosystems Department, Faculty of Agriculture, Shahrekord University, Shahrekord, Iran
3- Lecture of Mechanical Engineering of Biosystems Department, Faculty of Agriculture, Shahrekord University, Shahrekord, Iran
4- Assistant Professor, Mechanical Engineering, Faculty of Engineering, Yasouj University, Yasouj, Iran
(*- Corresponding Author Email: maleki@sku.ac.ir)

Received: 10 June 2023
Revised: 05 August 2023
Accepted: 21 August 2023
Available Online: 21 August 2023

How to cite this article:
Karimi Avargani, S., Maleki, A., Besharati, Sh., & Ebrahimi, R. (2024). Dynamic Model of Hip and Ankle Joints Loading during Working with a Motorized Backpack Sprayer. *Journal of Agricultural Machinery, 14*(1), 1-13. https://doi.org/10.22067/jam.2023.82788.1171

Abstract

The main objective of this paper is to develop a seven-link dynamic model of the operator's body while working with a motorized backpack sprayer. This model includes the coordinates of the sprayer relative to the body, the rotational inertia of the sprayer, the muscle moments acting on the joints, and a kinematic coupling that keeps the body balanced between the two legs. The constraint functions were determined and the non-linear differential equations of motion were derived using Lagrangian equations. The results show that undesirable fluctuations in the ankle force are noticeable at the beginning and end of a swing phase. Therefore, injuries to the ankle joint are more likely due to vibrations. The effects of engine speed and sprayer mass on the hip and ankle joint forces were then investigated. It is found that the engine speed and sprayer mass have significant effects on the hip and ankle forces and can be used as effective control parameters. The results of the analysis also show that increasing the engine speed increases the frequency of the hip joint force. However, no significant effects on the frequency of the ankle joint force are observed. The results of this study may provide researchers with insight into estimating the allowable working hours with the motorized backpack sprayers, prosthesis design, and load calculations of hip implants in the future.

Keywords: Lagrange equation, Operator, Vibration, Weight of sprayer

Introduction

One of the most popular ways of crop protection against weeds and pests is applying motorized backpack sprayers. The use of the motorized backpack sprayer eliminates the need for hand pumping and is suitable for small-scale farms. However, the major disadvantage of motorized backpack sprayers is the external forces acting on the operator's body (Kouchakzadeh, & Beigzadeh, 2015).

Forces acting on the human body are important factors in the initiation and progression of joint disease (Astephen, Deluzio, Caldwell, & Dunbar, 2008). Force analysis of hip and ankle joints can be useful in the development of strategies to avoid and manage conditions such as osteoarthritis and deterioration of femoroacetabular (Correa, Crossley, Kim, & Pandy, 2010). Force analysis of hip and ankle joints requires multi-segment models.

https://doi.org/10.22067/jam.2023.82788.1171

Several researches have been done on the dynamic modeling of the human body. Kuo (2001) applied a simple model of bipedal walking to evaluate simple hypotheses for the metabolic cost of muscle activity. Tlalolini, Chevallereau, & Aoustin (2010) optimized the walking motions of a bipedal model by minimizing the value of the torque. The optimization process was carried out with and without the rotation of the supporting foot about the toe. Huang, Wang, Chen, Xie, & Wang (2012) employed a seven-link dynamic bipedal walking model with flat feet to analyze the dynamics of walking. The results indicated that ankle stiffness plays different roles in different gaits. Martin & Schmiedeler (2014) proposed four and six link planar biped models with knees and rigid circular feet; The ankle was not considered in the four link model. The results showed that the model with ankles is more accurate in predicting energy consumption during normal human walking at different speeds. Sharbafi & Seyfarth (2015) utilized a five link model with a rigid upper body and two segmented legs to extract internal relations between the joints' angles and stance leg orientation which hold the configuration harmonized during the gaits. Jena, Kumar, Singh, & Mani (2016) developed a biomechanical model to predict metabolic energy consumption for carrying load manually by varying modes (head, shoulder, and back), loads, and ground inclinations. The results indicated that frontal torque (in shoulder mode) requires higher physiological energy than sagittal torque. Ma, Xu, Fang, Lv, & Zhang (2022) present the dynamic model of the human-prosthesis heterogeneous coupled system. Ma, Xu, & Zhang (2023) also applied control strategies for prosthesis walking on stochastically uneven terrain.

Mechanical actions of muscles are necessary for dynamical modeling of the human body and can be considered as moments applied at the joints. Weiss, Kearney, & Hunter (1986) indicated that the moment–angle relationships in the hip, knee, and ankle joints are similar to that of a non-linear spring. Maletsky & Hillberry (2005) designed a dynamic knee simulator to reproduce the loading and kinematics of the human knee during different activities. Lim & Park (2018) developed a model for human locomotion with a curvy foot connected to a leg by a springy segment. Thus, the oscillations of the center of mass during walking can be described by the mechanics of a simple passive Spring Loaded Inverted Pendulum (SLIP). Kim, Lee, & Koo (2018) simulated joint reaction forces, active moments by muscles, and passive moments by connective tissues. They found that, at Chopart and Lisfranc joints, passive moments were responsible for large portions of the net moment. The passive structures and passive moments in the midfoot joints provide strength and prevent injuries.

Carrying backpack loads for long distances is common in a range of human activities. As a result, the influence of backpack carriage on physical performance has been investigated to establish guidelines for safe load limits. Liu (2007) analyzed the effect of backpack load position, walking speed, and surface grade on the physiological responses of infantry soldiers. The results confirmed that positioning the backpack mass center as near as possible to the body mass center resulted in the lowest energy consumption. Alamoudi, Travascio, Onar-Thomas, Eltoukhy, & Asfour (2018) determined the effect of different carrying methods on walking stability using motion capture analysis. The results confirmed that the lack of stability in the frontal carriage forced the body to increase the cadence to maintain stability. Additionally, to minimize the moment generated by both the upper body and the heavy load, participants tended to decrease the length of their stride. Walsh, Low, & Arkesteijn (2018) studied the effect of stable and unstable load carriage on walking gait variability, dynamic stability, and muscle activity of older adults. The results showed that unstable load carriage reduces dynamic stability compared to unloaded walking.

Reviewing the literature reveals that the investigation of the joint forces during load carrying is important for preventing joint injuries. However, to date, no research has

been published on the joint forces during the working with the motorized backpack sprayers. Therefore, the initial objective of the present study is to develop a seven-link dynamic model of the operator's body while working with a motorized backpack sprayer. The secondary goal of this research is to examine the effects of different working conditions (engine speed and mass of sprayer) on the hip and ankle joint forces. This is a continuation of our previous work, where the torque–angle relationships in the hip, knee, and ankle joints for the backpack sprayer operator body were discussed (Karimi Avargani, Maleki, Besharati, & Ebrahimi, 2020).

Materials and Methods

In this section, the principle of the Lagrange equation for nonholonomic constraints is introduced. The total kinetic energy, potential energy, generalized forces, and constraints are expressed for the proposed model. The non-linear equations of motion are formulated using Lagrangian equations and solved using Maple software (Ver 2015).

Lagrange Equation for Nonholonomic Constraints

Lagrangian equations have a special place in analytical mechanics. They represent equations of motion in terms of generalized coordinates. A holonomic constraint in the system of n generalized coordinates q_i can be written as Eq. 1.

$$g_j(q_1, q_2, ..., q_n, t) = 0 \quad (1)$$

For nonholonomic constraints, Eq. 1 changes into a differential form in Eq. 2 (D'Souza & Garg, 1984; Greenwood, 1988):

$$\sum_{\upsilon=1}^{n} a_{l\upsilon} dq_\upsilon + a_{lt} dt = 0 \quad l=1, 2, \dots, s \quad (2)$$

Where $\upsilon=1, 2, \dots, n$ and $l=1, 2, \dots, s$ are the number of coordinates and number of constraints, respectively ($n>s$). Eq. 3 expresses Lagrange's equation for constrained systems.

$$\frac{d}{dt}\left(\frac{\partial T}{\partial \dot{q}_\upsilon}\right) - \frac{\partial T}{\partial q_\upsilon} + \frac{\partial V}{\partial q_\upsilon} - \sum_{l=1}^{s} \lambda_l a_{l\upsilon} = Q_\upsilon \quad \upsilon=1, 2, \dots, n \quad (3)$$

Where T, V, λ_l, and Q_v are kinetic energy, potential energy, Lagrange's coefficients, and generalized force related to generalized coordinate q_i, respectively. These n equations have $n+s$ unknowns, namely the n coordinates (q_v) and the s Lagrange multipliers (λ_l). The additional equations (Eq. 2) are needed for the s constraint which is coupled with the q_v. However, as shown in Eq. 4, these are considered as differential equations.

$$\sum_{\upsilon=1}^{n} a_{l\upsilon} \dot{q}_\upsilon + a_{lt} = 0 \quad l=1, 2, \dots, s \quad (4)$$

Dynamic model of operator's body during spraying

Fig. 1 shows the proposed dynamical model of the operator's body during working with a motorized backpack sprayer. This model includes two rigid legs connected to the rigid upper body with hinges at the hips. Each leg includes the thigh, shank, and foot. The thigh and the shank are connected at the knee joint and the foot and the shank are connected at the ankle joint. A point mass m_h at the hip represents the pelvis. The mass of upper body m_b, leg m_l, thigh m_t, shank m_s, and foot m_f are considered lumped parameters. Longitudinal parameters c_b, c_f, c_l, c_s, c_t, l, l_s, and l_t are distances from the hip joint to the Center of Mass (CoM) of upper body, from the ankle joint to CoM of foot, from the hip joint to CoM of stance leg, from knee joint to CoM of shank, from the hip joint to CoM of thigh, stance leg length, shank length, and thigh length, respectively. The motorized backpack sprayer is located at position (x_{sp}, y_{sp}) from the CoM of the upper body.

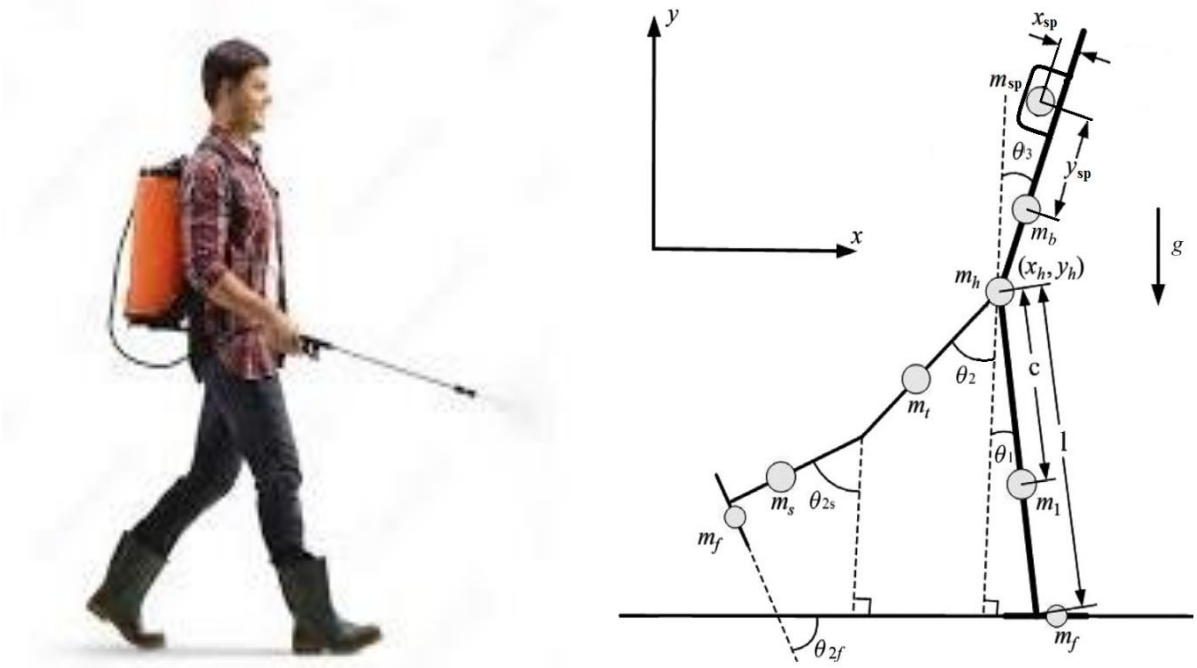

Fig.1. The proposed dynamical model of the operator's body while working with a motorized backpack sprayer

The total kinetic energy, potential energy, generalized forces, and constraints are expressed using the following assumptions (Wisse, Schwab, & van der Helm, 2004):

- The joints have no damping or friction.
- Bones do not suffer from flexible deformation.
- A kinematic coupling has been used in the model to keep the body midway between the two legs.
- The shank of the foot stance is always locked and the whole leg can be modeled as one rigid stick.
- There is enough friction between the walker and the ground. Thus, a flat foot does not deform or slip.
- The muscle moments acting on the hip, knee, and ankle joints are modeled as non-linear torsional springs.
- The sprayer engine is an unbalanced force. This can be caused by the deposition or erosion of the rotational parts.

Kinetic Energy

As shown in Fig. 1, it is assumed that the *x*-axis is along the ground while the *y*-axis is vertical to the ground pointing upward. The dynamic model for the operator's body while working with a motorized backpack sprayer can be described by the generalized coordinates (Eq. 5).

$$\tilde{q}^T = [x_h, y_h, \theta_1, \theta_2, \theta_3, \theta_{2s}, \theta_{2f}] \quad (5)$$

Where x_h, y_h, θ_1, θ_2, θ_3, θ_{2s}, and θ_{2f} are the horizontal coordinate of hip joint, vertical coordinate of hip joint, the angle between vertical axis and the stance leg, the swing angle between vertical axis and the thigh, the angle between vertical axis and the upper body, the swing angle between vertical axis, and the shank and the angle between horizontal axis and foot, respectively. The positive direction of all the angles is counterclockwise. The total kinetic energy of the system is defined as the sum of the kinetic energy of the point masses, and the translational and rotational kinetic energy of the motorized backpack sprayer. The expression for the kinetic energy is obtained in Eq. 6.

$$
\begin{aligned}
T &= T_h + T_l + T_t + T_b + T_{sp} + T_s + T_f \\
&= \frac{1}{2}[m_h + m_l + m_t + m_b + m_{sp} + m_s + m_f]\dot{x}_h^2 \\
&+ \frac{1}{2}[m_h + m_l + m_t + m_b + m_{sp} + m_s + m_f]\dot{y}_h^2 \\
&+ \frac{1}{2}m_l c_l^2 \dot{\theta}_1^2 + \frac{1}{2}\left[m_t c_t^2 + m_s l_t^2 + m_f l_t^2\right]\dot{\theta}_2^2 \\
&+ \frac{1}{2}\left[I_{sp} + m_b c_b^2 + m_{sp}\left[\left(c_b + y_{sp}\right)^2 + x_{sp}^2\right]\right]\dot{\theta}_3^2 \\
&+ \frac{1}{2}\left[m_s c_s^2 + m_f l_s^2\right]\dot{\theta}_{2s}^2 + \frac{1}{2}m_f c_f^2 \dot{\theta}_{2f}^2 + m_l c_l \dot{\theta}_1\left(\dot{x}_h \cos\theta_1 + \dot{y}_h \sin\theta_1\right) \\
&- m_t c_t \dot{\theta}_2\left(\dot{x}_h \cos\theta_2 - \dot{y}_h \sin\theta_2\right) + m_b c_b \dot{\theta}_3\left(\dot{x}_h \cos\theta_3 - \dot{y}_h \sin\theta_3\right) \\
&+ m_{sp}\dot{\theta}_3\left\{\left[\left(c_b + y_{sp}\right)\dot{x}_h + x_{sp}\dot{y}_h\right]\cos\theta_3 + \left[x_{sp}\dot{x}_h - \left(c_b + y_{sp}\right)\dot{y}_h\right]\sin\theta_3\right\} \\
&+ m_s\left\{l_t c_s \dot{\theta}_2 \dot{\theta}_{2s}\cos\left(\theta_2 - \theta_{2s}\right) - \dot{x}_h\left[l_t\dot{\theta}_2\cos\theta_2 + c_s\dot{\theta}_{2s}\cos\theta_{2s}\right] + \dot{y}_h\left[l_t\dot{\theta}_2\sin\theta_2 + c_s\dot{\theta}_{2s}\sin\theta_{2s}\right]\right\} \\
&+ m_f\left\{l_t l_s \dot{\theta}_2\dot{\theta}_{2s}\cos\left(\theta_2 - \theta_{2s}\right) + c_f l_t \dot{\theta}_2\dot{\theta}_{2f}\sin\left(\theta_{2f} - \theta_2\right) + c_f l_s \dot{\theta}_{2s}\dot{\theta}_{2f}\sin\left(\theta_{2f} - \theta_{2s}\right)\right. \\
&\quad - \dot{x}_h\left[l_t\dot{\theta}_2\cos\theta_2 + l_s\dot{\theta}_{2s}\cos\theta_{2s} + c_f\dot{\theta}_{2f}\sin\theta_{2f}\right] \\
&\quad \left. + \dot{y}_h\left[l_t\dot{\theta}_2\sin\theta_2 + l_s\dot{\theta}_{2s}\sin\theta_{2s} - c_f\dot{\theta}_{2f}\cos\theta_{2f}\right]\right\}
\end{aligned} \tag{6}
$$

Where I_{sp} is the mass moment of inertia of the sprayer about its principal axis.

Potential Energy

The total potential energy of the system is given in Eq. 7 and is defined as the sum of the gravitational energy of the point masses.

$$
\begin{aligned}
U &= U_h + U_l + U_t + U_b + U_{sp} + U_s + U_f \\
&= -\left[m_h l + m_l\left(l - c_l\right) + m_t l + m_b l + m_{sp} l + m_s l\right]g\left(1 - \cos\theta_1\right) \\
&\quad + \left[m_t c_t + m_s l_t\right]g\left(1 - \cos\theta_2\right) - \left[m_b c_b + m_{sp}\left(c_b + y_{sp}\right)\right]g\left(1 - \cos\theta_3\right) \\
&\quad + m_{sp} g x_{sp}\sin\theta_3 + m_s g c_s\left(1 - \cos\theta_{2s}\right) \\
&\quad + m_f g\left(l\cos\theta_1 - l_t\cos\theta_2 - l_s\cos\theta_{2s} - c_f\sin\theta_{2f}\right)
\end{aligned} \tag{7}
$$

Generalized Forces

The generalized forces acting on the operator's body while working with a motorized backpack sprayer include forces resulting from gravity and are unbalanced due to erosion of the sprayer engine, muscle moment acting on the hip joint, muscle moment acting on the knee joint, and muscle moment acting on the ankle joint. The generalized forces Q_{qi} are given by the following equations (Eq. 8-14).

$$Q_{x_h} = m_0 e\omega^2\cos(\omega t) \tag{8}$$

$$Q_{y_h} = m_0 e\omega^2\sin(\omega t) \tag{9}$$

$$Q_{\theta_1} = T_{1f} \tag{10}$$

$$Q_{\theta_2} = T_2 \tag{11}$$

$$
\begin{aligned}
Q_{\theta_3} &= m_0 e\omega^2\cos\omega t[(c_b + y_{sp})\cos\theta_3 + x_{sp}\sin\theta_3] \\
&\quad + m_0 e\omega^2\sin\omega t[-(c_b + y_{sp})\sin\theta_3 + x_{sp}\cos\theta_3]
\end{aligned} \tag{12}
$$

$$Q_{\theta_{2s}} = T_{2s} \tag{13}$$

$$Q_{\theta_{2f}} = 0 \tag{14}$$

Where m_0, e, and ω are the unbalanced mass of the sprayer engine, the unbalanced mass eccentricity, and the engine speed, respectively.

The muscle moment acting on the hip joint T_2 (the swing leg, Eq. 15), muscle moment acting on the knee joint T_{2s} (the swing leg, Eq. 16), and muscle moment acting on the ankle joint T_{1f} (stance leg, Eq. 17) are non-linear functions of the angle between the two segments (Karimi *et al.*, 2020).

$$T_2 = 0.0007(\theta_2 - \theta_3)^3 - 0.0258(\theta_2 - \theta_3)^2 + 0.3236(\theta_2 - \theta_3) - 1.6792 \tag{15}$$

$$T_{2s} = -0.0011(\theta_{2s} - \theta_2)^2 - 0.0029(\theta_{2s} - \theta_2) + 1.2683 \tag{16}$$

$$T_{1f} = 0.0043\theta_1^3 + 0.0429\theta_1^2 + 0.5052\theta_1 + 3.1455 \tag{17}$$

Constraints

A constraint can be expressed by a relationship between generalized coordinates and time. When foot contact with the ground is maintained, first and second constraint equations can be represented as Eq. 18 and 19.

$$y_h - l\cos\theta_1 = 0 \tag{18}$$

$$x_h + l\sin\theta_1 - x_{ankle} = 0 \tag{19}$$

Here, the x_{ankle} is the fixed position of the ankle of the stance leg. In the passive dynamical model of a walking human, the upper body can be considered as an inverted pendulum jointed at the hip. Therefore, a kinematic coupling has been used in the model to keep the upper body between the two legs and achieve stable walking (Wisse *et al.*, 2004). The equation of the kinematic coupling constraint is introduced according to Eq. 20.

$$2\theta_3 - (\theta_1 + \theta_2) = 0 \tag{20}$$

The time course of hip, knee, and ankle joint angles for the proposed model are given in Eqs. 21-23 (Karimi *et al.*, 2020).

$$\theta_2 - \theta_3 = 373.64t^3 - 762.66t^2 + 414.86t - 38.89 \tag{21}$$

$$\theta_{2s} - \theta_2 = -6357.5t^3 + 4911.3t^2 - 958.48t + 1.24 \tag{22}$$

$$\theta_1 = 451.84t^3 - 513.31t^2 + 218.5t - 27.77 \tag{23}$$

According to Eq. 4, the constraint equations (Eqs. 18-23) can be considered in differential form, as defined in Eqs. 24-29:

$$\dot{y}_h + l\sin\theta_1\dot{\theta}_1 = 0 \tag{24}$$

$$\dot{x}_h + l\cos\theta_1\dot{\theta}_1 = 0 \tag{25}$$

$$\dot{\theta}_1 + \dot{\theta}_2 - 2\dot{\theta}_3 = 0 \quad (26)$$

$$\dot{\theta}_2 - \dot{\theta}_3 - 1120.92t^2 + 1525.32t - 414.86 = 0 \quad (27)$$

$$\dot{\theta}_2 - \dot{\theta}_{2s} - 19072.5t^2 + 9822.6t - 958.48 = 0 \quad (28)$$

$$\dot{\theta}_1 - 1355.52t^2 + 1026.62t - 218.5 = 0 \quad (29)$$

By applying Lagrange's equation (Eq. 3) and introducing the constant coefficients, seven coupled non-linear differential equations of motion can be obtained (Eqs. 30-36).

$$\begin{aligned}&\eta_1\ddot{x}_h + \eta_2\cos\theta_1\ddot{\theta}_1 - \eta_3\cos\theta_2\ddot{\theta}_2 + [\eta_4\cos\theta_3 + \eta_5\sin\theta_3]\ddot{\theta}_3 - \eta_6\cos\theta_{2s}\ddot{\theta}_{2s}\\&- \eta_7\sin\theta_{2f}\ddot{\theta}_{2f} - \eta_2\sin\theta_1\dot{\theta}_1^2 + \eta_3\sin\theta_2\dot{\theta}_2^2 - [\eta_4\sin\theta_3 - \eta_5\cos\theta_3]\dot{\theta}_3^2\\&+ \eta_6\sin\theta_{2s}\dot{\theta}_{2s}^2 - \eta_7\cos\theta_{2f}\dot{\theta}_{2f}^2 + \lambda_2 = m_0 e\omega^2\cos(\omega t)\end{aligned} \quad (30)$$

$$\begin{aligned}&\eta_1\ddot{y}_h + \eta_2\sin\theta_1\ddot{\theta}_1 + \eta_3\sin\theta_2\ddot{\theta}_2 - [\eta_4\sin\theta_3 - \eta_5\cos\theta_3]\ddot{\theta}_3 + \eta_6\sin\theta_{2s}\ddot{\theta}_{2s}\\&- \eta_7\cos\theta_{2f}\ddot{\theta}_{2f} + \eta_2\cos\theta_1\dot{\theta}_1^2 + \eta_3\cos\theta_2\dot{\theta}_2^2 - [\eta_4\cos\theta_3 + \eta_5\sin\theta_3]\dot{\theta}_3^2\\&+ \eta_6\cos\theta_{2s}\dot{\theta}_{2s}^2 + \eta_7\sin\theta_{2f}\dot{\theta}_{2f}^2 + \lambda_1 = m_0 e\omega^2\sin(\omega t)\end{aligned} \quad (31)$$

$$\begin{aligned}&\eta_8\ddot{\theta}_1 + \eta_2(\cos\theta_1\ddot{x}_h + \sin\theta_1\ddot{y}_h) - \eta_9 g\sin\theta_1 + \lambda_4 l\sin\theta_1 + \lambda_2 l\cos\theta_1 + \lambda_3 + \lambda_6\\&= 0.0043\theta_1^3 + 0.0429\theta_1^2 + 0.5052\theta_1 + 3.1455\end{aligned} \quad (32)$$

$$\begin{aligned}&\eta_{10}\ddot{\theta}_2 - \eta_3\cos\theta_2\ddot{x}_h + \eta_3\sin\theta_2\ddot{y}_h + \eta_{11}\cos(\theta_2 - \theta_{2s})\ddot{\theta}_{2s} + \eta_{12}\sin(\theta_{2f} - \theta_2)\ddot{\theta}_{2f}\\&+ \eta_{11}\sin(\theta_2 - \theta_{2s})\dot{\theta}_{2s}^2 + \eta_{12}\cos(\theta_{2f} - \theta_2)\dot{\theta}_{2f}^2 + \eta_3 g\sin\theta_2 + \lambda_3 + \lambda_4 + \lambda_5\\&= 0.0007(\theta_2 - \theta_3)^3 - 0.0258(\theta_2 - \theta_3)^2 + 0.3236(\theta_2 - \theta_3) - 1.6792\end{aligned} \quad (33)$$

$$\begin{aligned}&\eta_{13}\ddot{\theta}_3 + (\eta_4\cos\theta_3 + \eta_5\sin\theta_3)\ddot{x}_h - (\eta_4\sin\theta_3 - \eta_5\cos\theta_3)\ddot{y}_h - \eta_4 g\sin\theta_3\\&+ \eta_5 g\cos\theta_3 - 2\lambda_3 - \lambda_4 = m_0 e\omega^2\cos\omega t\left[(c_b + y_{sp})\cos\theta_3 + x_{sp}\sin\theta_3\right]\\&- m_0 e\omega^2\sin\omega t\left[(c_b + y_{sp})\sin\theta_3 - x_{sp}\cos\theta_3\right]\end{aligned} \quad (34)$$

$$\begin{aligned}&\eta_{14}\ddot{\theta}_{2s} - \eta_6\cos\theta_{2s}\ddot{x}_h + \eta_6\sin\theta_{2s}\ddot{y}_h + \eta_{11}\cos(\theta_2 - \theta_{2s})\ddot{\theta}_2 + \eta_{15}\sin(\theta_{2f} - \theta_{2s})\ddot{\theta}_{2f}\\&- \eta_{11}\sin(\theta_2 - \theta_{2s})\dot{\theta}_2^2 + \eta_{15}\dot{\theta}_{2f}^2\cos(\theta_{2f} - \theta_{2s}) + \eta_6 g\sin\theta_{2s} - \lambda_5 =\\&= -0.0011(\theta_{2s} - \theta_2)^2 - 0.0029(\theta_{2s} - \theta_2) + 1.2683\end{aligned} \quad (35)$$

$$\begin{aligned}&c_f\ddot{\theta}_{2f} - \sin\theta_{2f}\ddot{x}_h - \cos\theta_{2f}\ddot{y}_h + l_t\sin(\theta_{2f} - \theta_2)\ddot{\theta}_2 + l_s\sin(\theta_{2f} - \theta_{2s})\ddot{\theta}_{2s}\\&- l_t\cos(\theta_{2f} - \theta_2)\dot{\theta}_2^2 - l_s\cos(\theta_{2f} - \theta_{2s})\dot{\theta}_{2s}^2 - g\cos\theta_{2f} = 0\end{aligned} \quad (36)$$

The constant coefficients η_i (i=1, 2, …, 15) are defined in the Appendix. Thirteen coupled non-linear differential equations (Eqs. 24-36) for x_h, y_h, θ_1, θ_2, θ_3, θ_{2s}, θ_{2f}, λ_1, λ_2, λ_3, λ_4, λ_5, and λ_6 must be solved to analyze the dynamical behavior of the operator's body during working with a motorized backpack sprayer.

Hip and ankle joint forces in the swing phase

Forces in the human joints are important factors in the initiation and progression stages of joint diseases. Investigation of the joint forces has made it possible to prevent or minimize discomfort, fatigue, or risk of injuries. In this section, the hip and ankle joint forces in the model of the operator's body while working with a motorized backpack sprayer are calculated. Considering the upper body, Newton's second law leads to Eqs. 37 and 38.

$$\sum F_x = m_b\ddot{x}_{m_b} + m_{sp}\ddot{x}_{m_{sp}} + m_0 e\omega^2\cos(\omega t) \quad (37)$$

$$\sum F_y = m_b\ddot{y}_{m_b} + m_{sp}\ddot{y}_{m_{sp}} + m_0 e\omega^2\sin(\omega t) \quad (38)$$

The components of the hip joint force then become Eqs. 39 and 40.

$$\begin{aligned}F_{x_h} &= m_b(\ddot{x}_h + c_b\cos\theta_3\ddot{\theta}_3) + m_{sp}(\ddot{x}_h + x_{sp}\sin\theta_3\ddot{\theta}_3 + (c_b + y_{sp})\cos\theta_3\ddot{\theta}_3)\\&+ m_0 e\omega^2\cos(\omega t)\end{aligned} \quad (39)$$

$$\begin{aligned}F_{y_h} &= m_b(\ddot{y}_h - c_b\sin\theta_3\ddot{\theta}_3) + m_{sp}(\ddot{y}_h + x_{sp}\cos\theta_3\ddot{\theta}_3 - (c_b + y_{sp})\sin\theta_3\ddot{\theta}_3)\\&+ m_0 e\omega^2\sin(\omega t) + (m_{sp} + m_b)g\end{aligned} \quad (40)$$

Finally, the total hip joint force can be calculated using Eq. 41.

$$F_h = \sqrt{F_{x_h}^2 + F_{y_h}^2} \quad (41)$$

Considering the full body, Newton's second law leads to Eq. 42.

$$\sum F_x = m_b\ddot{x}_{m_b} + m_f\ddot{x}_{m_f} + m_h\ddot{x}_{m_h} + m_t\ddot{x}_{m_t} + m_s\ddot{x}_{m_s} + m_{sp}\ddot{x}_{m_{sp}} + m_t\ddot{x}_{m_t} + m_0 e\omega^2\cos(\omega t) \quad (42)$$

And the x-directional force of the hip joint is expressed in Eq. 43.

$$\begin{aligned}F_{x_f} &= m_b(\ddot{x}_h + c_b\cos\theta_3\ddot{\theta}_3) + m_f(\ddot{x}_h - l_s\cos\theta_{2s}\ddot{\theta}_{2s} - l_t\cos\theta_2\ddot{\theta}_2 - c_f\sin\theta_{2f}\ddot{\theta}_{2f})\\&+ m_h\ddot{x}_h + m_l(l - c_l)\cos\theta_1\ddot{\theta}_1 + m_s(\ddot{x}_h - c_s\cos\theta_{2s}\ddot{\theta}_{2s} - l_t\cos\theta_2\ddot{\theta}_2)\\&+ m_{sp}(\ddot{x}_h + x_{sp}\sin\theta_3\ddot{\theta}_3 + (c_b + y_{sp})\cos\theta_3\ddot{\theta}_3)\\&+ m_t(\ddot{x}_h - c_t\cos\theta_2\ddot{\theta}_2) + m_0 e\omega^2\cos(\omega t)\end{aligned} \quad (43)$$

Considering the leg stance, the calculation of the moment about the hip joint leads to Eq. 44.

$$F_{y_f} = m_l c_l(l - c_l)\ddot{\theta}_1 + m_l g c_l\sin\theta_1 - F_{x_f} l\cos\theta_1 / l\sin\theta_1 \quad (44)$$

Finally, the total ankle joint force is calculated using Eq. 45.

$$F_f = \sqrt{F_{x_f}^2 + F_{y_f}^2} \quad (45)$$

Results and Discussion

The values of the physical parameters related to this analysis are listed in Table 1. Thirteen coupled non-linear differential equations (Eqs. 24-36) are solved in Maple software. Fig. 2 illustrates the effects of engine speed and mass of the sprayer on the hip and ankle joint forces during working with a motorized backpack sprayer.

It can be observed that the ankle force fluctuates at the beginning of the swing phase (*t=[0.1-0.2]*). It remains relatively constant in the middle of the swing phase *t=[0.2-0.4]* and again fluctuates at the end of the swing phase (*t=[0.4-0.5]*). The first fluctuation occurs because of the 'toe-off'. In the 'toe-off'

instance, the toe loses contact with the ground. The second fluctuation was caused by the 'heel-strike'. In this instance, there is an impact between the leg swing and the ground when the heel of the swinging leg comes into contact with the ground. The maximum force is exerted on the joints when the operator begins to swing forward ('toe-off'). Furthermore, in the instances of 'toe-off' and 'heel-strike', undesirable variations of ankle joint force F_h are noticeable. This means that ankle injuries due to vibration exposure are more likely.

Table 1- The values of physical parameters (Huang *et al.*, 2012)

Parameter	Value
Distance from hip joint to CoM of the upper body, cb	0.262 m
Distance from the ankle joint to CoM of the foot, cf	0.017 m
Distance from the knee joint to CoM of shank, cs	0.157 m
Distance from hip joint to CoM of the thigh, ct	0.192
Unbalance mass eccentricity, e	5 mm
Gravitational acceleration, g	9.81 m s^{-2}
Mass moments of inertia of sprayer about its principal axis, I_{sp}	$kg.m^2$
Stance leg length, l	0.700 m
Shank length, l_s	0.315 m
Thigh length, l_t	0.385 m
Unbalance mass of sprayer engine, m_o	0.01 gr
Upper body mass, m_b	26.62 kg
Foot mass, m_f	2.66 kg
Hip mass, m_h	19.97 kg
Leg mass, m_l	11.53 kg
Shank mass, m_s	3.45 kg
Sprayer mass, m_{sp}	10.50 kg
Thigh mass, m_t	8.07 kg
Sprayer position from the CoM of upper body, (x_{sp}, y_{sp})	(0.175m, 0.038m)
Engine speed, ω	3000 rpm

From a comparison between Fig. 2 (a) and (b) it is revealed that the frequency of the hip joint force increases with increased engine speed (ω). However, considerable effects on the frequency of the ankle joint force have not been observed. Additionally, with increasing the engine speed (ω), amplitudes of both the hip and ankle joint forces increase.

From a comparison between Fig. 2 (a) and (c) it can be concluded that increasing the mass of the sprayer (msp) leads to a small reduction in the oscillation of the ankle joint force. Moreover, as the mass of the sprayer (msp) increases, the magnitude of both the hip and ankle joint forces increases as well.

Fig. 3 exhibits the effect of leg length on the hip and ankle joint forces while working with a motorized backpack sprayer. It can be observed that the frequency of the hip joint force increases with decreasing the leg length l. This is because the leg stance keeps contact with the ground while the leg swings and pivots about the constrained hip like a pendulum. So, shorter operators are more vulnerable to injuries due to vibration exposure.

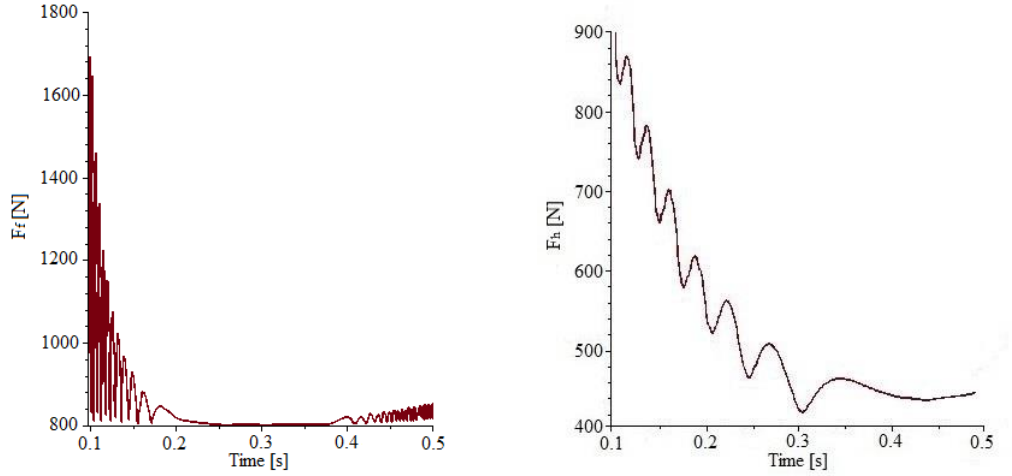

a) ω=3000 rpm, m_{sp}=10.5 kg, l=0.7 m

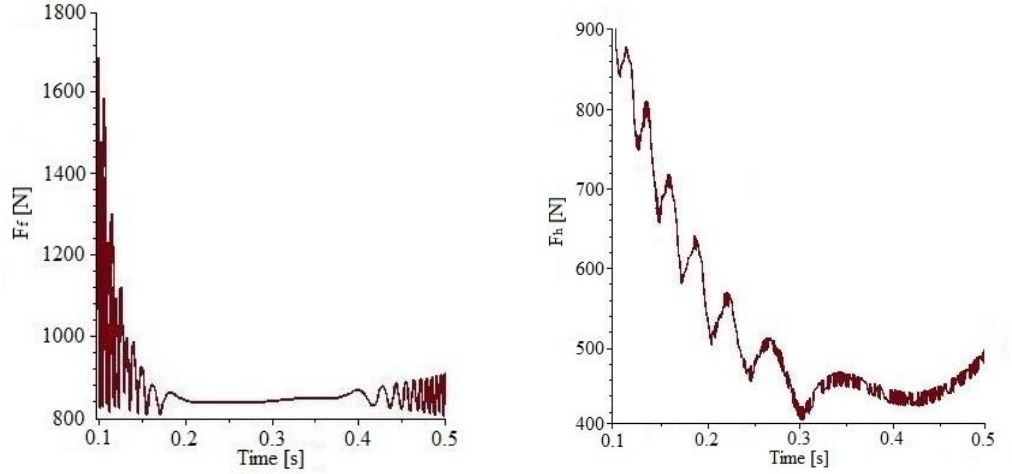

b) ω=6000 rpm, m_{sp}=10.5 kg, l=0.7 m

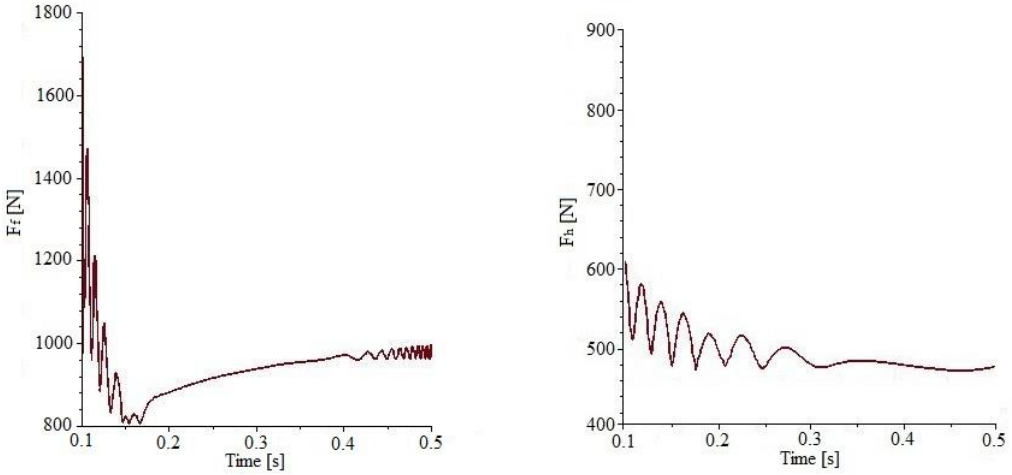

c) ω=3000 rpm, m_{sp}=12.5 kg, l=0.7 m

Fig.2. The hip joint force F_h and ankle joint force F_f for l=0.7 m and (a) m_{sp}=10.5 kg, ω=3000 rpm, (b) m_{sp}=10.5 kg, ω=6000 rpm, and (c) m_{sp}=12.5 kg, ω=3000 rpm

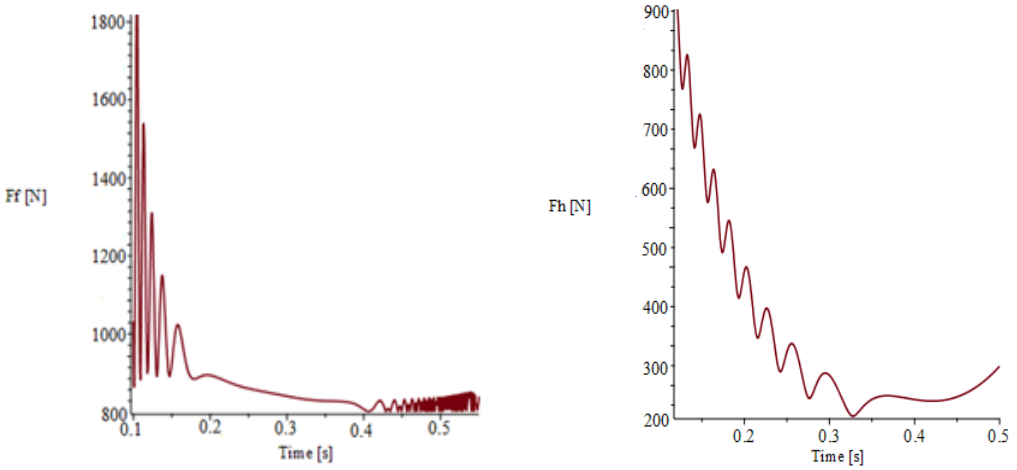

a) ω=3000 rpm, m_{sp}=10.5 kg, l=0.88 m

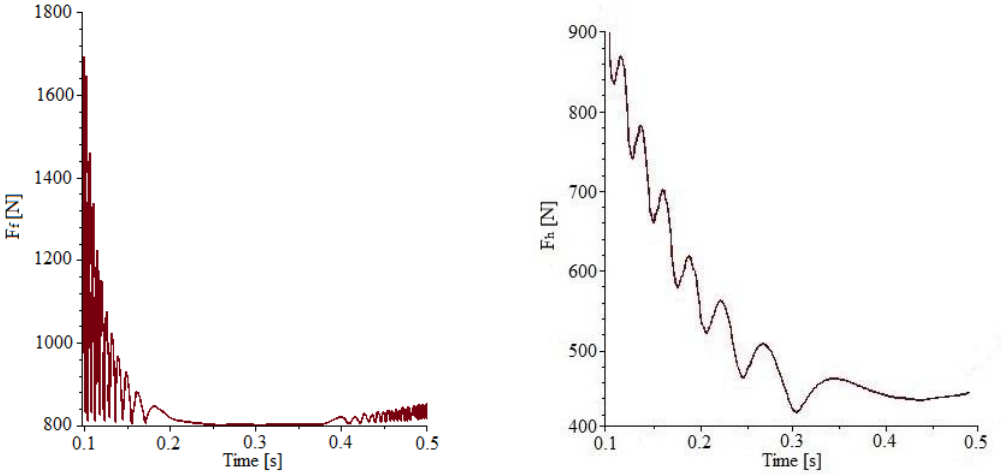

b) ω=3000 rpm, m_{sp}=10.5 kg, l=0.7 m

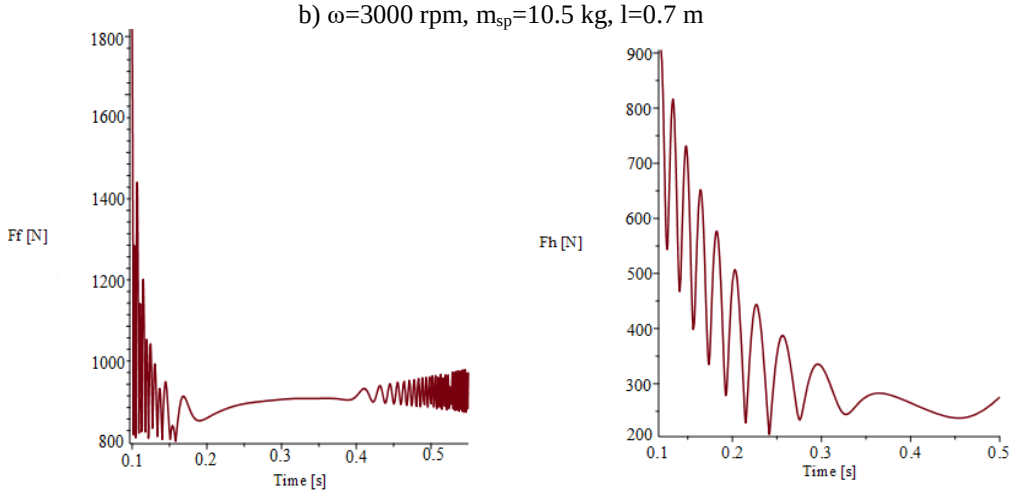

c) ω=3000 rpm, m_{sp}=10.5 kg, l=0.6 m

Fig.3. The hip joint force F_h and ankle joint force F_f for m_{sp}=10.5 kg, ω=3000 rpm, and (a) l=0.7 m, (b) l=0.7 m, and (c) l=0.7 m

Conclusion

In this study, a novel assistive dynamical model for the operator's body while working with a motorized backpack sprayer was presented. In this model, the coordinate of the

sprayer relative to the body, rotational inertia of the sprayer, muscle moments acting on joints, and a kinematic coupling confining the upper body between the two legs were considered. The dynamics of the sprayer's operator were described using seven generalized coordinates. The non-linear equations of motion were obtained using the Lagrangian equations. The results obtained from the numerical analysis indicated that, at the beginning and end of the swing phase, ankle injuries due to vibration exposure are more probable. Moreover, the maximum force is exerted on the joints at the beginning of the swing phase. Furthermore, the effects of engine speed and mass of the sprayer on the hip and ankle joint forces were studied. It was found that the larger mass of the sprayer (full capacity of the tank) can lead to higher levels of joint forces and lower oscillations. The frequency of hip and ankle joint forces increased with the increase of the engine speed. The results of this paper can be used for an estimated evaluation of a patient's condition and implant design. Investigation of the effects of anthropometric specifications and sprayer position (relative to the body) on the hip and ankle joint forces while working with a motorized backpack sprayer are valuable topics for further studies.

Key Points

- Development of a seven-link dynamic model of the operator's body while working with a motorized backpack sprayer
- The non-linear differential equations of motion are formulated using Lagrangian equations and solved in Maple software
- Study of the effects of engine speed and mass of sprayer on the hip and ankle joint forces

Acknowledgments

The authors would like to thank the University of Shahrekord for providing the laboratory facilities and financial support for this research.

Symbols and Abbreviations

Parameter	Description	Unite
c_b	Distance from hip joint to center of mass (CoM) of upper body	m
c_f	Distance from the ankle joint to CoM of the foot	m
c_s	Distance from the knee joint to the CoM of the shank	m
c_t	Distance from hip joint to CoM of the thigh	m
e	Unbalance mass eccentricity	mm
g	Gravitational acceleration	ms^{-2}
I_{sp}	Mass moments of inertia of sprayer about its principal axis	$kg.m^2$
l	Stance leg length	m
l_s	Shank length	m
l_t	Thigh length	m
m_o	Unbalance mass of sprayer engine	gr
m_b	Upper body mass	kg
m_f	Foot mass	kg
m_h	Hip mass	kg
m_l	Leg mass	kg
m_s	Shank mass	kg
m_{sp}	Sprayer mass	kg
m_t	Thigh mass	kg
(x_{sp}, y_{sp})	Sprayer position from the CoM of the upper body	(m, m)
ω	Engine speed	rpm
x_h	Horizontal coordinate of hip joint	M
y_h	Vertical coordinate of the hip joint	M
θ_1	The angle between the vertical axis and the stance leg	Radian
θ_2	The swing angle between the vertical axis and the thigh	Radian
θ_3	The angle between the vertical axis and the upper body	Radian
θ_{2s}	The swing angle between the vertical axis and the shank	Radian
θ_{2f}	The angle between the horizontal axis and the foot	Radian

Appendix

The constant coefficients for Eqs. 30-36 are as follows:

$$\eta_1 = m_h + m_l + m_t + m_b + m_{sp} + m_s + m_f \qquad \eta_2 = m_l c_l$$

$$\eta_3 = m_t c_t + m_s l_t + m_f l_t \qquad \eta_4 = m_b c_b + m_{sp}\left(c_b + y_{sp}\right)$$

$$\eta_5 = m_{sp} x_{sp} \qquad \eta_6 = m_s c_s + m_f l_s$$

$$\eta_7 = m_f c_f \qquad \eta_8 = m_l c_l^2$$

$$\eta_9 = \eta_1 l - m_l c_l \qquad \eta_{10} = m_t c_t^2 + m_s l_t^2 + m_f l_t^2$$

$$\eta_{11} = l_t \eta_6 \qquad \eta_{12} = m_f l_t c_f$$

$$\eta_{13} = I_{sp} + m_b c_b^2 + m_{sp}\left[\left(c_b + y_{sp}\right)^2 + x_{sp}^2\right] \qquad \eta_{14} = m_s c_s^2 + m_f l_s^2$$

$$\eta_{15} = m_f l_s c_f$$

References

1. Alamoudi, M., Travascio, F., Onar-Thomas, A., Eltoukhy, M., & Asfour, S. (2018). The effects of different carrying methods on locomotion stability, gait spatio-temporal parameters, and spinal stresses. *International Journal of Industrial Ergonomics*, *67*, 81-88. https://doi.org/10.1016/j.ergon.2018.04.012
2. Astephen, J. L., Deluzio, K. J., Caldwell, G. E., & Dunbar, M. J. (2008). Biomechanical changes at the hip, knee, and ankle joints during gait are associated with knee osteoarthritis severity. *Journal of Orthopaedic Research*, *26*(3), 332-341. https://doi.org/10.1002/jor.20496
3. Correa, T. A., Crossley, K. M., Kim, H. J., & Pandy, M. G. (2010). Contributions of individual muscles to hip joint contact force in normal walking. *Journal of Biomechanics*, *43*(8), 1618-1622. https://doi.org/10.1016/j.jbiomech.2010.02.008
4. D'Souza, A. F., & Garg, V. K. (1984). *Advanced dynamics: modeling and analysis*. Prentice Hall.
5. Greenwood, D. T. (1988). *Principles of dynamics* (pp. 224-226). Englewood Cliffs, NJ: Prentice-Hall.
6. Huang, Y., Wang, Q., Chen, B., Xie, G., & Wang, L. (2012). Modeling and gait selection of passivity-based seven-link bipeds with dynamic series of walking phases. *Robotica*, *30*(1), 39-51. https://doi.org/10.1017/S0263574711000397
7. Jena, S., Kumar, A., Singh, J. K., & Mani, I. (2016). Biomechanical model for energy consumption in manual load carrying on Indian farms. *International Journal of Industrial Ergonomics*, *55*, 69-76. https://doi.org/10.1017/S0263574711000397
8. Karimi Avargani, S., Maleki, A., Besharati, S., & Ebrahimi, R. (2020). Muscle moment and angle of hip, knee and ankle joints in a seven-link model of backpack sprayer operator. *Iranian Journal of Ergonomics*, *8*(3), 36-47. https://doi.org/10.30699/jergon.8.3.36
9. Kim, Y., Lee, K. M., & Koo, S. (2018). Joint moments and contact forces in the foot during walking. *Journal of biomechanics*, *74*, 79-85. https://doi.org/10.1016/j.jbiomech.2018.04.022
10. Kouchakzadeh, A., & Beigzadeh, Y. (2015). Permitted working hours with a motorised backpack sprayer. *Biosystems Engineering*, *136*, 1-7. https://doi.org/10.1016/j.biosystemseng.2015.05.005
11. Kuo, A. D. (2001). A simple model of bipedal walking predicts the preferred speed–step length relationship. *Journal of Biomechanical Engineering*, *123*(3), 264-269. https://doi.org/10.1115/1.1372322
12. Lim, H., & Park, S. (2018). Kinematics of lower limbs during walking are emulated by springy walking model with a compliantly connected, off-centered curvy foot. *Journal of*

Biomechanics, *71*, 119-126. https://doi.org/10.1016/j.jbiomech.2018.01.031
13. Liu, B. S. (2007). Backpack load positioning and walking surface slope effects on physiological responses in infantry soldiers. *International Journal of Industrial Ergonomics*, *37*(9-10), 754-760. https://doi.org/10.1016/j.ergon.2007.06.001
14. Ma, X., Xu, J., Fang, H., Lv, Y., & Zhang, X. (2022). Adaptive Neural Control for Gait Coordination of a Lower Limb Prosthesis. *International Journal of Mechanical Sciences*, *215*, 106942. https://doi.org/10.1016/j.ijmecsci.2021.106942
15. Ma, X., Xu, J., & Zhang, X. (2023). Bilateral constrained control for prosthesis walking on stochastically uneven terrain. *International Journal of Mechanical Sciences*, *239*, 107896. https://doi.org/10.1016/j.ijmecsci.2022.107896
16. Maletsky, L. P., & Hillberry, B. M. (2005). Simulating dynamic activities using a five-axis knee simulator. *Journal of Biomechanical Engineering*, *127*, 123-133. https://doi.org/10.1115/1.1846070
17. Martin, A. E., & Schmiedeler, J. P. (2014). Predicting human walking gaits with a simple planar model. *Journal of biomechanics*, *47*(6), 1416-1421. https://doi.org/10.1016/j.jbiomech.2014.01.035
18. Sharbafi, M. A., & Seyfarth, A. (2015, May). Mimicking human walking with 5-link model using HZD controller. In *2015 IEEE International Conference on Robotics and Automation (ICRA)* (pp. 6313-6319). IEEE. https://doi.org/10.1109/ICRA.2015.7140086
19. Tlalolini, D., Chevallereau, C., & Aoustin, Y. (2010). Human-like walking: Optimal motion of a bipedal robot with toe-rotation motion. *IEEE/ASME Transactions on Mechatronics*, *16*(2), 310-320. https://doi.org/10.1109/TMECH.2010.2042458
20. Walsh, G. S., Low, D. C., & Arkesteijn, M. (2018) Effect of stable and unstable load carriage on walking gait variability, dynamic stability and muscle activity of older adults. *Journal of Biomechanics*, *73*, 18-23. https://doi.org/10.1016/j.jbiomech.2018.03.018
21. Weiss, P. L., Kearney, R. E., & Hunter, I. W. (1986). Position dependence of ankle joint dynamics—I. Passive mechanics. *Journal of Biomechanics*, *19*(9), 727-735. https://doi.org/10.1016/0021-9290(86)90196-X
22. Wisse, M., Schwab, A. L., & van der Helm, F. C. (2004). Passive dynamic walking model with upper body. *Robotica*, *22*(6), 681-688. https://doi.org/10.1017/S0263574704000475

نشریه ماشین‌های کشاورزی
https://jame.um.ac.ir

مقاله پژوهشی

جلد ۱٤، شماره ۱، بهار ۱٤۰۳، ص ۱۳-۱

مدل‌سازی دینامیکی بار وارد بر مفاصل ران و مچ پا، هنگام کار با سمپاش پشتی موتوری

صدیقه کریمی آورگانی[۱]، علی ملکی[۲*]، شاهین بشارتی[۳]، رضا ابراهیمی[٤]

تاریخ دریافت: ۱۴۰۲/۰۳/۲۰
تاریخ پذیرش: ۱۴۰۲/۰۵/۳۰

چکیده

هدف اصلی این مقاله توسعه یک مدل دینامیک هفت لینکی از بدن اپراتور در هنگام کار با سمپاش کوله‌پشتی موتوری است. این مدل شامل مختصات سمپاش نسبت به بدن، اینرسی چرخشی سمپاش، گشتاور ماهیچه‌ای وارد بر روی مفاصل و یک کوپلینگ سینماتیکی است که تعادل بدن را بین دو پا حفظ می‌کند. توابع قید تعیین شدند و معادلات دیفرانسیل غیرخطی حرکت توسط معادلات لاگرانژ استخراج گردیدند. نتایج نشان می‌دهد که در ابتدا و انتهای مرحله شناوری، تغییرات نامطلوب نیروی مفصل مچ پا قابل‌توجه است. بنابراین، آسیب مچ پا به دلیل قرار گرفتن در معرض ارتعاش احتمال بیشتری دارد. سپس اثرات دور موتور و جرم سمپاش بر نیروهای مفصل ران و مچ پا بررسی شد. نتایج نشان داد که دور موتور و جرم سمپاش اثرات قابل‌توجهی بر نیروهای مفصل ران و مچ پا دارد و می‌تواند به‌عنوان پارامترهای کنترلی موثر مورد استفاده قرار گیرد. همچنین، نتایج آنالیز نشان می‌دهد که با افزایش دور موتور، فرکانس نیروی مفصل ران افزایش می‌یابد. با این حال، اثرات قابل‌توجهی بر فرکانس نیروی مفصل مچ پا مشاهده نشده است. نتایج به‌دست‌آمده از این تحقیق می‌تواند راه‌کارهایی را به محققان در برآورد ساعات کار مجاز با سمپاش‌های کوله‌پشتی موتوری، طراحی پروتز و محاسبات نیرویی ایمپلنت‌های ران در آینده ارائه دهد.

واژه‌های کلیدی: اپراتور، ارتعاش، معادله لاگرانژ، وزن سمپاش

۱- دانشجوی کارشناسی ارشد گروه مهندسی مکانیک بیوسیستم، دانشکده کشاورزی، دانشگاه شهرکرد، شهرکرد، ایران
۲- دانشیار و عضو هیات علمی گروه مهندسی مکانیک بیوسیستم، دانشکده کشاورزی، دانشگاه شهرکرد، شهرکرد، ایران
۳- مربی گروه مهندسی مکانیک بیوسیستم، دانشکده کشاورزی، دانشگاه شهرکرد، شهرکرد، ایران
۴- استادیار، گروه مهندسی مکانیک، دانشکده فنی و مهندسی، دانشگاه یاسوج، یاسوج، ایران
(*- نویسنده مسئول: Email: maleki@sku.ac.ir)

https://doi.org/10.22067/jam.2023.82788.1171

Journal of Agricultural Machinery

Homepage: https://jame.um.ac.ir

Research Article
Vol. 14, No. 1, Spring 2024, p. 15-34

Investigating the Efficiency of Drinking Water Treatment Sludge and Iron-Based Additives in Anaerobic Digestion of Dairy Manure: A Kinetic Modeling Study

J. Rezaeifar[1], A. Rohani[1*], M. A. Ebrahimi-Nik[1]

1- Department of Biosystems Engineering, Faculty of Agriculture, Ferdowsi University of Mashhad, Mashhad, Iran
(*- Corresponding Author Email: arohani@um.ac.ir)

Received: 28 June 2023
Revised: 26 July 2023
Accepted: 29 July 2023
Available Online: 29 July 2023

How to cite this article:
Rezaeifar, J., Rohani, A., & Ebrahimi-Nik, M. A. (2024). Investigating the Efficiency of Drinking Water Treatment Sludge and Iron-Based Additives in Anaerobic Digestion of Dairy Manure: A Kinetic Modeling Study. *Journal of Agricultural Machinery*, *14*(1), 15-34. https://doi.org/10.22067/jam.2023.83173.1176

Abstract

In the quest for enhanced anaerobic digestion (AD) performance and stability, iron-based additives as micro-nutrients and drinking water treatment sludge (DWTS) emerge as key players. This study investigates the kinetics of methane production during AD of dairy manure, incorporating varying concentrations of Fe and Fe_3O_4 (10, 20, and 30 mg L^{-1}) and DWTS (6, 12, and 18 mg L^{-1}). Leveraging an extensive library of non-linear regression (NLR) models, 26 candidates were scrutinized and eight emerged as robust predictors for the entire methane production process. The Michaelis-Menten model stood out as the superior choice, unraveling the kinetics of dairy manure AD with the specified additives. Fascinatingly, the findings revealed that different levels of DWTS showcased the highest methane production, while $Fe_3O_4$20 and $Fe_3O_4$30 recorded the lowest levels. Notably, DWTS6 demonstrated approximately 34% and 42% higher methane production compared to Fe20 and $Fe_3O_4$30, respectively, establishing it as the most effective treatment. Additionally, DWTS12 exhibited the highest rate of methane production, reaching an impressive 147.6 cc on the 6th day. Emphasizing the practical implications, this research underscores the applicability of the proposed model for analyzing other parameters and optimizing AD performance. By delving into the potential of iron-based additives and DWTS, this study opens doors to revolutionizing methane production from dairy manure and advancing sustainable waste management practices.

Keywords: Anaerobic digestion, Kinetic study, Livestock manure, Modeling, Trace elements

Introduction

In recent decades, the world has witnessed an unprecedented surge in population and industrial development, especially in developing countries, leading to a remarkable rise in energy demand and waste generation. Improper waste management coupled with excessive reliance on conventional fossil fuels has contributed to environmental issues such as global warming and ozone layer depletion. Nonetheless, within the vast realm of biomass waste, lies a promising solution– the potential to tap into its renewable capacity and harness clean energy resources, like biofuels and biogas (Lu & Gao, 2021). The production of biogas from livestock manure has seen widespread adoption across numerous countries worldwide. In Iran, the Ministry of Agriculture reports a staggering population of over 8.4 million cattle and an annual beef production rate that has surged by 5%. Despite these statistics, except in a few industrial farms, a significant portion of the produced manure remains untreated and is often left in the open or directly applied to the land without composting. Nevertheless, Iran has immense potential for biogas production, with an

https://doi.org/10.22067/jam.2023.83173.1176

estimated yield of 16,146.35 million m^3 from various waste sources encompassing agricultural and animal wastes, and municipal and industrial wastewater. This abundance of potential biogas could produce substantial energy, totaling approximately 323 petajoules (10^{15}) and thus positioning Iran as a country with vast and valuable biogas resources (Zareei, 2018).

The process of anaerobic digestion (AD) stands as a remarkably efficient technique, facilitating the transformation of biomass waste into highly valuable end products. Foremost among these is biogas; predominantly composed of methane, carbon dioxide, and hydrogen (Wellinger, Murphy, & Baxter, 2013). Despite the rapid development of AD technology, some of its drawbacks such as low biodegradation efficiency, poor stability, and environmental sensitivity, have hindered its commercial application. To address these challenges, approaches such as co-digestion, pretreatment, and new reactor designs, as well as the use of additives have been proposed. The additives stimulate bacterial growth and reduce inhibitory effects which can help control microbial generation time, degradation rate, and gas production (Choong, Norli, Abdullah, & Yhaya, 2016; Gkotsis, Kougias, Mitrakas, & Zouboulis, 2023). Studies conducted by Al Seadi *et al.* (2008) and Cheng *et al.* (2020) emphasize the significance of incorporating trace elements or micro-nutrients like iron (Fe), cobalt (Co), or nickel (Ni) into the anaerobic digestion process. These additives play a crucial role in facilitating the digestion process.

Dudlet's research in 2019 reveals that iron has immense potential as a cost-effective enhancer in AD methane production. Furthermore, industrial enterprises generate around 18,895 thousand tonnes of iron waste every year, but only around 8,000 thousand tonnes get recycled and the remaining iron scraps are discarded into landfills (Dudley, 2019). Iron, being an essential element in the methanogenesis process, assumes a pivotal role in elevating biogas yield. Its unique capacity to ionize Fe_2+ and Fe_3+ ions enables it to serve as both an electron donor and acceptor. Chen, Konishi, & Nomura (2018) report that iron-based additives offer numerous advantages, including nutrient supplementation, improved methane yield, enhanced substrate digestibility, and effective control of H_2S toxicity, among other benefits. A range of iron-based additives have common usage including waste iron scraps (Wiss), iron nanoparticles (Fe NPs), iron chlorides ($FeCl_2$, $FeCl_3$), zero valent scrap iron (ZVSI), iron oxides (Fe_2O_3, Fe_3O_4), iron powder (Fe powder), zero-valent iron (ZVI), iron sulfate ($FeSO_4$), and nano zero-valent iron (NZVI). Notably, waste iron scraps, iron oxides (Fe_3O_4), and iron powder emerge as prevalent and cost-effective additives due to the abundance of their sources and straightforward preparation methods. Additionally, these additives are commercially produced and readily available (Muddasar, 2022). Numerous studies have demonstrated the potential of these three types of iron-based additives to boost biogas yield and enhance process stability when utilized with diverse substrates. For instance, Cheng *et al.* (2020) observed a remarkable 64.4% increase in methane yield when rusted iron shavings were added to a mixture of food waste and municipal sludge. Furthermore, the addition of Fe powder led to a 14.46% rise in methane yield, while clean Fe scrap further elevated methane yield by 21.28% (Zhang, Feng, Yu, & Quan, 2014). Hao, Wei, Van, & Cao (2017) and Kong *et al.* (2018) have reported significant findings on the impact of adding Fe to anaerobic digesters handling the organic fraction of municipal solid waste (OFMSW) and sludge. The inclusion of Fe led to about 40% increase in CH_4 yield for OFMSW digestion and a 20% increase in sludge digestion. According to Abdelsalam *et al.* (2016), incorporating 20 mg/L Fe nanoparticles resulted in a 1.7-fold increase in biogas yield. Similarly, Ali, Mahar, Soomro, & Sherazi (2017) found that, when utilizing municipal solid waste (MSW) as a substrate for the AD process, the addition of 75 mg L^{-1} concentration of Fe_3O_4 nanoparticles can lead to 72.09% enhancement

in methane generation. In another study by Noonari, Mahar, Sahito, & Brohi (2019), it was demonstrated that the introduction of 0.81 mg of Fe_3O_4 nanoparticles as iron-based additives led to a 39.1% increase in methane generation using canola straw and buffalo dung. Additionally, Zhao, Li, Quan, & Zhang (2017) reported that Fe_3O_4 additive in the AD process had a significant impact on biogas yield, with Fe_3O_4 nanoparticles (Fe_3O_4 NPs), Iron powder, and Iron nanoparticles following suit. These additives also proved beneficial in enhancing substrate digestibility by decomposing lignocellulosic biomass into simpler structures.

While trace elements have proven to be beneficial, their widespread implementation remains limited primarily due to their high cost. To address this issue, and render their utilization economically feasible, more affordable sources of micro-nutrients could be explored (Huiliñir, Montalvo & Guerrero, 2015). Several studies (Huiliñir *et al.*, 2015; Huiliñir, Pinto-Villegas, Castillo, Montalvo, & Guerrero, 2017; Ebrahimi-Nik, Heidari, Azghandi, Mohammadi, & Younesi, 2018) have highlighted the successful utilization of fly ash and drinking water treatment sludge (DWTS). DWTS is composed of alkaline, trace, heavy metals, and clay, arising from the treatment of surface water for drinking purposes. Despite its potential, DWTS is currently disposed of as waste and even requires appropriate disposal methods (Ahmad, Ahmad, & Alam, 2016). In their research, Torres-Lozada *et al.* delved into the impact of adding drinking water sludge to domestic wastewater sludge, aiming to enhance methane production during AD. Their findings revealed that the most favorable mixtures for anaerobic co-digestion should consist of under 20% DWTS (Torres-Lozada, Diaz-Granados & Parra-Orobio, 2015). Ebrahimi-Nik *et al.* (2018) explored the impact of adding DWTS to a mixture of biogas and methane production from food waste. Their findings demonstrated that DWTS additive can lead to a substantial improvement in both biogas and methane yield, up to 65%.

While an optimal dosage of trace elements has been shown to positively impact AD performance, it is crucial to bear in mind that an excessive amount might have adverse effects on the process (Demirel & Scherer, 2011; Schmidt, Nelles, Scholwin & Proter, 2014). Therefore, the application of mathematical modeling in AD proves to be a rapid and cost-effective approach for predicting and optimizing fuel processing engineering and waste industry design (Andriamanohiarisoamanana, Ihara, Yoshida & Umetsu, 2020). In this context, AD processes exhibit compatibility with non-linear models, as the microorganisms' growth and subsequent production kinetics are frequently non-linear (Khamis, 2005). Numerous non-linear regressions (NLRs) were derived from AD experiments, emphasizing the significance of making appropriate selections from an extensive library of functions (Archontoulis & Miguez, 2015). Moreover, it is crucial to ensure that the samples are not only adequately large but also accurately representative to achieve the desired outcomes with the regression model. However, due to the method's high sensitivity, errors may arise (Wang, Tang & Tan, 2011; Wang *et al.*, 2021).

Despite extensive research in the field, there are currently no published studies exploring the potential of enhancing biogas yield by incorporating DWTS into the anaerobic digestion process of dairy manure and comparing it with iron-based additives. Thus, the present project seeks to fill this knowledge gap and aims to model the impact of iron-based additives, namely Fe, Fe_3O_4, and DWTS, as trace elements and additives for biogas production during the anaerobic digestion process of dairy manure.

Materials and Methods

Materials

The primary feedstock utilized in this study was dairy manure, sourced from the livestock farm of Ferdowsi University of Mashhad, Iran. Fe_3O_4 and iron shavings served as the trace elements in this research. The iron shavings, smaller than 1 mm, were procured from the

mechanics laboratory of Ferdowsi University of Mashhad, Iran. To remove oil and impurities, the shavings were immersed in a 14 M sodium hydroxide solution for 24 hours, followed by a day of air drying at room temperature. Additionally, drinking water treatment sludge (DWTS) was obtained from a drinking water treatment plant in Mashhad, Iran, and used as an additive. DWTS, when rich in Fe_2O_3, plays a crucial role in municipal water purification. The composition of DWTS used in this research closely resembles the one described in our previous study (Ebrahimi-Nik *et al.*, 2018). The key components of DWTS in descending order include Fe_2O_3, SiO_2, CaO, and Al_2O_3. The abundance of Fe_2O_3, as revealed by X-ray fluorescence (XRF) analysis, was a result of adding iron chloride as a flocculent during the drinking water treatment process. SiO_2 stemmed from the inclusion of suspended solids and various types of clay. Moreover, small quantities of other oxides like MgO, P_2O_5, MnO, TiO_2, P_2O, and N_2O were identified. DWTS contained trace elements such as Ni, Cr, Co, Zn, Cu, Ba, Sr, Cl, and Zr, detected in parts per million (ppm) levels as well. Before utilization, the sludge underwent air drying and was then ground and passed through specialized sieves to achieve a maximum particle size of 0.63 mm. Additionally, following the methodology outlined in recent studies, microcrystalline cellulose (MERCK-Germany) was prepared as a validation material for inspecting the inoculum's quality (Holliger *et al.*, 2016). To carry out the experiments, a complete stirred tank reactor (CSTR) was employed at Ferdowsi University of Mashhad, Iran, maintaining a stable state and receiving daily feedings of food waste, primarily consisting of rice.

Data collection and laboratory experimentation

Conducting the AD process under mesophilic conditions at 37°C, we performed three independent experimental replicates following the procedure outlined by Holliger *et al.* (2016). The essential inoculum for the AD tests was procured from an active digester within Ferdowsi University of Mashhad's biogas laboratory, which maintained a steady-state operation. To regulate its biogas production rate and ensure suitability for the AD experiments, the collected inoculum underwent 20 days of incubation at 37°C in a warm-water bath (Rosato, 2017).

The experiments were carried out using 500 mL bottles, with a working volume of 400 mL and each bottle's gas-tightness was ensured. To facilitate the gas collection, each bottle was connected to a 2 L gas collection bag via the pneumatic mediator (PUSH-FIT) attached to its lid through a plastic tube. Both the inlet and outlet were present on the gas bags, with a heparin cap connected to the outlet, enabling methane measurement using a syringe. Before sealing the digesters, carbon dioxide was purged over the solution for 30 seconds, establishing anaerobic conditions. Fig. 1 illustrates the experimental setup utilized in this study. The generated biogas was passed through a 7 M sodium hydroxide solution, effectively eliminating impurities and converting them into pure methane (Stoddard, 2010). To maintain a constant temperature of 37°C, a water bath (also known as a bain-marie) was utilized. Additionally, Eq. 1 was employed to determine the suitable materials and their ratios for each bottle.

$$ISR = \frac{V_{in}.VS_{in}}{V_{sub}.VS_{sub}} \quad (1)$$

Where V_{in} represents the volume of inoculum, VS_{in} refers to the VS of inoculum based on wet weight, V_{sub} denotes the volume of substrate, and VS_{sub} represents the VS of the substrate based on wet weight. The ratio of inoculum to substrate (ISR) was adjusted to 5%.

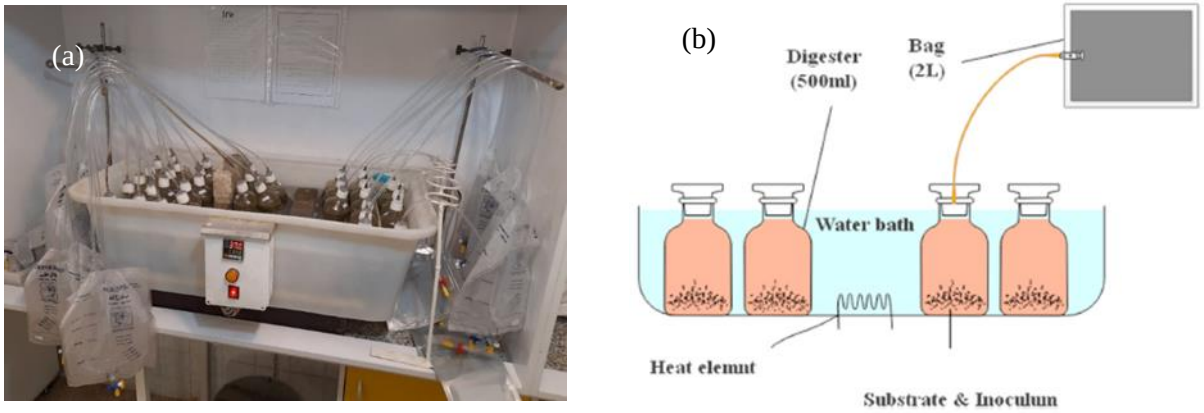

Fig.1. Digesters and the Experimental setup (a) photo and (b) schematic illustration

Using a scale with a precision of 0.001 grams, the quantities of each additive were measured. Fe and Fe_3O_4 were added at three levels: 10, 20, and 30 mg L^{-1}. DWTS was utilized at three concentrations of 6, 12, and 18 mg L^{-1}. Table 1 illustrates the experimental treatments and their corresponding symbols, as used in the subsequent section. In this experiment, cellulose was employed as a positive control and combined with the appropriate amount of inoculum to achieve an ISR ratio of 2, with three replicates. Therefore, three bottles containing only inoculum were utilized as control treatments in this study. Consequently, the difference between the methane production of the treated and the control samples ascertains the effect of each treatment on methane production.

Daily measurements of biogas and methane production resulting from the treatments were carried out using a 60cc syringe (Raposo, De la Rubia, Fernández-Cegrí, & Borja, 2012). The anaerobic digestion process spanned 43 days and was concluded when the rate of methane production dropped below 1% of the total cumulative methane production during three consecutive days (Holliger *et al.*, 2016). Throughout this period, the ambient temperature was recorded every day using a mercury thermometer, and the atmospheric pressure data was sourced from the Mashhad synoptic station. These two parameters were crucial for converting the measured biomethane volume into its corresponding standard volume (at standard conditions of temperature T=273.15 K and pressure P=101.325 kPa (Ebrahimzadeh, Ebrahimi-Nik, Rohani & Tedesco, 2021).

Table 1- Experimental treatment information

Additives	Treatment	Unit (mg L^{-1})	Treatment symbol
DWTS	DWTS 6	6	T1
	DWTS 12	12	T2
	DWTS 18	18	T3
Fe	Fe 10	10	T4
	Fe 20	20	T5
	Fe 30	30	T6
Fe_3O_4	Fe_3O_4 10	10	T7
	Fe_3O_4 20	20	T8
	Fe_3O_4 30	30	T9

Measurement of total solids (TS) and volatile solids (VS)

Throughout and after the experiment, analyses were conducted following established

standards. Specifically, the substrates' total solids (TS) and volatile solids (VS) content were determined before and after the experiments as per the American Standard for Public Health (APHA, 2005). To achieve this, a 50-gram sample comprising various materials used in the experiment (including cellulose, inoculum, and cow manure) was placed in an oven and heated at 105 degrees Celsius for a total of 24 hours. The samples were weighed initially and every hour while in the oven. This process was repeated until the weight of the samples dropped less than 4% in an hour, indicating they had reached a state of constant weight. At this point, the total solids (TS) value was calculated using Eq. 2.

$$TS = \frac{(A - B) \times 100}{(C - B)} \quad (2)$$

The percentage of total solids (TS) is represented by the variables A, B, and C corresponding to the weight of the dried sample plus petri dish, the petri dish, and the wet sample (substrate) plus petri dish, respectively. To ensure the accuracy of our results, each of these steps was triplicated. The dried materials from the previous step were utilized to calculate the content of volatile solids (VS). For this purpose, a 2-gram sample comprising the mentioned materials was placed inside an oven at a temperature of 550 degrees Celsius for one hour. Then, it was removed and weighed. This process was repeated after another 30 minutes in the oven. The experiment continued until the samples reached a steady state, with a weight change of less than 4% (APHA, 2005) and then VS was calculated using Eq. 3.

$$VS = \frac{(A - D)}{(A - B)} \times 100 \quad (3)$$

Where VS represents the percentage of total solids, while A, B, and D correspond to the weight of the petri dish plus container, the container alone, and the sample plus container after being heated in an oven, respectively.

Nonlinear regression analysis of biogas production kinetics

To examine the production of biogas through the anaerobic digestion of dairy manure and determine the relevant kinetic parameters, nonlinear regression (NLR) models were utilized. Nonlinear regression proves to be a robust instrument for estimating the parameters, including the degradation rate, the gas volume generated per nutrient degradation, and the fermentation process's lag phase of anaerobic digestion (Ebrahimzadeh, Ebrahimi-Nik, Rohani, & Tedesco, 2022). When dealing with unclear or time-dependent associations between the variables in intricate biological systems such as anaerobic digesters, NLR models offer notable advantages. The estimation process in these models incorporates iterative techniques, such as the Levenberg-Marquardt algorithm, which adjusts the model's parameters iteratively to achieve an optimal fit to the data by minimizing the discrepancy between the predicted and actual values. By employing Eq. 4 within the NLR model, the cumulative biogas production (y) as a function of digestion time (t) in the biogas reactor can be effectively assessed. This equation takes into account a random error term (ε), which captures any unexplained variation in the relationship between y and t.

$$y = f(t, \beta) + \varepsilon \quad (4)$$

To determine the β coefficients that most accurately depict the data, the objective of NLR involves the process of curve fitting. The estimation of these coefficients is usually achieved by minimizing the sum of squared errors (SSE) between the predicted and observed values of the dependent variable. To evaluate the NLR model and its coefficients' importance, researchers often employ the analysis of variance (ANOVA). There are multiple methods of determining NLR model coefficients, and a popular approach is to utilize the Levenberg-Marquardt algorithm, which incorporates a regularization term to prevent overfitting. For our study, the model coefficients were acquired by using the MATLAB function *fitnlm*, which is a built-in function capable of fitting multitudes of NLR models to data. A comprehensive summary of the NLRs analyzed in our study is presented in Table 2. It illustrates the ability to fit an

extensive range of data patterns, including exponential, logarithmic, polynomial, sinusoidal, generalized Mitscherlich, Michael Menten, and power-law functions. NLRs offer a versatile approach to fitting various data patterns.

Table 2- Nonlinear regression models for analyzing biogas production from dairy manure

Name	Equation	Symbol
Logistic-Exponential without LAG	$f(t) = a\frac{1-\exp(-bt)}{1+\exp\left(\ln\left(\frac{1}{d}\right)-bt\right)}$	M1
Logistic-Exponential with LAG	$f(t) = a\frac{1-\exp(-b(t-c))}{1+\exp\left(\ln\left(\frac{1}{d}\right)-b(t-c)\right)}$	M2
Exponential without LAG	$f(t) = a(1-\exp(-bt))$	M3
Exponential with LAG	$f(t) = a(1-\exp(-b(t-c)))$	M4
Gompertz	$f(t) = a\exp(-\exp(1-b(t-c)))$	M5
Logistic	$f(t) = a\frac{1}{1+\exp(2+b(c-t))}$	M6
Generalization of the Mitscherlich	$f(t) = a\,(1-\exp\left(-b(t-c)-d(\sqrt{t}-\sqrt{c})\right))$	M7
Michaelis-Menten (MM)	$f(t) = a\frac{t^c}{t^c+b^c}$	M8
Modified MM	$f(t) = a\frac{t^c}{t^c+b}$	M9
Two-pool exponential	$f(t) = \sum_{i=1}^{2} a_i(1-\exp(-b_i(t-c)))$	M10
Two-pool logistic	$f(t) = \sum_{i=1}^{2} a_i\frac{1}{(1+\exp(2-4b_i(t-c)))}$	M11
Modified Gompertz	$f(t) = a\exp(-\exp\left(2.71\frac{b}{a}(c-t)+1\right))$	M12
Logistic	$f(t) = a\frac{1}{1+b\exp(-ct)}$	M13
Gompertz	$f(t) = a\exp(-b\exp(-ct))$	M14
Richard	$f(t) = a\frac{1}{(1+b\times\exp(-ct))^{1/d}}$	M15
Double-Sigmoid	$f(t) = a\frac{1}{1+\exp(-(b+ct+dt^2+et^3))}$	M16
Monomolecular- logistic	$f(t) = a(1-\exp(-bt)) + \frac{c}{1+\exp(-d(t-e))}$	M17
Chapman-Richard	$f(t) = a(1-b\times\exp(-ct))^{\left(\frac{1}{1-d}\right)}$	M18
Exponential-linear	$f(t) = \frac{a}{b}\times\ln(1+\exp(b(t-ct)))$	M19
LinBiExp	$f(t) = a\times\ln\left(\exp\left(\frac{b(t-c)}{d}\right)\right)+\exp\left(\frac{e(t-f)}{g}\right)+f$	M20
Cone	$f(t) = a\left(\frac{1}{1+(bt)^{-c}}\right)$	M21
Contois	$f(t) = a\left(1-\frac{b}{ct+b-1}\right)$	M22
Fitzhugh	$f(t) = a(1-\exp(-bt)^c)$	M23
France	$f(t) = \frac{a(1-\exp^{-bt})}{(1+c\exp^{-bt})}$	M24
Monod without LAG	$f(t) = a\frac{bt}{bt+1}$	M25
Monod with LAG	$f(t) = a\frac{b(t-c)}{b(t-c)+1}$	M26

Criteria for evaluating the fit of nonlinear regression models

To assess the goodness-of-fit of nonlinear regression models, we employed Eq. 5 representing the coefficient of determination (R^2), Eq. 6 for calculating root mean square error (RMSE), and the minimum value predicted by the model (MP). The process of identifying the most fitting models was facilitated through the application of these criteria, and we were able to identify the models that most precisely depict the fundamental biogas production kinetics using them.

$$R^2 = 1 - \frac{\sum_1^N \left(B_{ai} - \hat{B}_{pi}\right)^2}{\sum_1^N (B_{ai} - \overline{B_a})^2} \quad (5)$$

$$RMSE = \sqrt{\sum_{i=1}^{n} \frac{\left|B_{ai} - \hat{B}_{pi}\right|^2}{N}} \quad (6)$$

Where B_a and B_p denote the experimental and predicted values, respectively. The $\overline{B_a}$ represents the average value of the experimental values, and N denotes the sample size. When selecting the best model, a good fit with experimental data is indicated by a low RMSE value and a high R^2 value. Because biogas production originates from zero at the start of the digestion process, the fitted model must also pass through the origin of coordinates. The model's physical interpretability and validity for predicting future biogas yields are ensured with this crucial requirement. In other words, the requirement of passing through the origin of the coordinates is crucial to guarantee the model's physical interpretability and validity for future biogas yield predictions.

Results and Discussions

This section focuses on evaluating the performance of non-linear regression models applied to the cumulative methane data gathered throughout the anaerobic digestion process. Furthermore, a comparison is made between the gas production rates and the average cumulative methane produced using the various treatments.

Finding the best-fit non-linear regression model

Accurate analysis of the cumulative methane data obtained during the anaerobic digestion process relies on selecting the most appropriate non-linear regression model. One crucial criterion for this selection is the model's ability to cross the origin of the coordinates, ensuring that it estimates a value of zero at the beginning of the digestion process. This property ensures that the model is consistent with the actual process. In Table 3, we present the predicted cumulative methane production at the start of the anaerobic digestion process for 26 non-linear regression models. Through our evaluation, out of the 26 models, we identified eight valid models that met this property. While some other models, like M22, M13, and M2, could predict zero values for specific treatments only; making them unsuitable for our analysis. Consequently, we excluded these models from further consideration and focused on the ones predicting a zero value for all treatments. Thus, we narrowed down our selection to these eight models for further analysis. In the subsequent sections, we will discuss the performance of these eight models and compare their results to identify the best-fit model for analyzing the cumulative methane data.

Table 3- Predicted minimum amounts of methane produced during the digestion time for the studied treatments, utilizing 26 non-linear regression models

Model	T1	T2	T3	T4	T5	T6	T7	T8	T9
M1	0.00	0.00	0.00	0.00	0.00	0.00	0.00	0.00	0.00
M2	-190	-203	-162	-16	-44	0	0.00	0.00	0.00
M3	0.00	0.00	0.00	0.00	0.00	0.00	0.00	0.00	0.00
M4	-155	-222	-132	-14	-197	-75	-251	-132	-40
M5	100	46	65	31	33	22	0.00	0.00	0.00
M6	263	165	202	47	109	46	14	3	21
M7	-155	-226	-171	-21	-194	-80	-154	-96	-41
M8	0.00	0.00	0.00	0.00	0.00	0.00	0.00	0.00	0.00
M9	0.00	0.00	0.00	0.00	0.00	0.00	0.00	0.00	0.00
M10	-97	-90	-73	-65	-70	-69	-44	-48	-57
M11	97	0	91	66	6	6	54	45	77
M12	100	46	65	31	33	22	0.00	0.00	0.00
M13	1	1	1	0	1	3	0.00	0.00	0.00
M14	100	46	65	34	33	22	0.00	14	18
M15	89	49	82	40	33	21	1	0.00	28.48
M16	1124	1055	886	413	712	582	633	432	352
M17	1.27	0.00	0.00	1.69	0.00	3.57	2	0.00	0.00
M18	58	63	59	3	60	68	15	6	9
M19	1039	1022	845	29	747	728	7	5	32
M20	347	258	347	50	330	318	38	58	106
M21	0.00	0.00	0.00	0.00	0.00	0.00	0.00	0.00	0.00
M22	0	0	0	0	0	0	0	0	-150
M23	0.00	0.00	0.00	0.00	0.00	0.00	0.00	0.00	0.00
M24	0.00	0.00	0.00	0.00	0.00	0.00	0.00	0.00	0.00
M25	924	951	803	286	686	645	471	322	284
M26	0.00	0.00	0.00	0.00	0.00	0.00	0.00	0.00	0.00

In Table 4, the results of RMSE and R^2 for each of the nine treatments are presented. Based on the R^2 criterion, we observed that four models (M9, M21, M24, and M26) lacked sufficient predictive ability to estimate cumulative methane production during the digestion process, as their R^2 values were the lowest. Among the remaining four models, the Michaelis-Menten model (M8) demonstrated superior predictive ability for all treatments. Although the M1 model also exhibited good predictive ability, we excluded it from the selection list due to its complexity in comparison to the M8 model. Consequently, we proceeded with the Michaelis-Menten non-linear regression model (M8) for further analyses, which will be presented in the following sections.

Iron-based additives exhibited diverse behaviors during the biodegradation process of dairy manure. Although the First-order and Gompertz models are commonly used for monitoring biodegradation in anaerobic digestion (AD) processes, they were not found to be adequately suitable for modeling the AD of dairy manure with iron-based additives. The biodegradation of starch-based bioplastic under anaerobic conditions was evaluated to determine an appropriate kinetic model. The analysis involved examining 26 nonlinear regression models, and it was found that the modified Michaelis-Menten (MM) model was the best-fitted model for the biodegradation process (Ebrahimzadeh *et al.*, 2022). The innovative multi-Gompertz model has been proposed as the most suitable model for biogas production from residual marine macroalgae biomass (Pardilhó, Pires, Boaventura, Almeida & Dias, 2022). Additionally, other models are employed for more specific conditions and additives, such as higher solids contents (e.g., Chen and Hashimoto model), or specific microorganisms (e.g., cone model) (Karki *et al.*, 2022; Lima, Adarme, Baˆeta, Gurgel, & de Aquino, 2018; Masih-Das & Tao, 2018).

Table 4- Assessment of eight selected non-linear regression models using RMSE and R^2 criteria

		T1	T2	T3	T4	T5	T6	T7	T8	T9
M1	RMSE	118	137	139	189	139	142	92	87	79
	R^2	0.97	0.96	0.95	0.75	0.92	0.87	0.97	0.94	0.92
M3	RMSE	118	149	140	190	150	145	534	138	108
	R^2	0.97	0.95	0.95	0.74	0.90	0.86	0.00	0.85	0.85
M8	RMSE	90	118	130	187	134	138	91	85	81
	R^2	0.98	0.97	0.95	0.75	0.92	0.87	0.97	0.94	0.92
M9	RMSE	674	963	130	471	746	574	709	450	325
	R^2	0.11	0.00	0.95	0.00	0.00	0.00	0.00	0.00	0.00
M13	RMSE	288	254	257	247	202	163	119	102	88
	R^2	0.84	0.86	0.82	0.57	0.82	0.82	0.95	0.92	0.90
M21	RMSE	1318	1256	1063	367	805	630	625	319	191
	R^2	0.00	0.00	0.00	0.00	0.00	0.00	0.00	0.21	0.53
M24	RMSE	1321	1259	1066	375	807	633	634	341	214
	R^2	0.00	0.00	0.00	0.00	0.00	0.00	0.00	0.10	0.41
M26	RMSE	553	528	454	321	362	277	480	320	244
	R^2	0.40	0.39	0.43	0.27	0.44	0.49	0.13	0.20	0.24

Table 5 presents the coefficients of the Michaelis-Menten nonlinear regression model, along with their standard deviation, p-values, coefficient of determination (R^2), and the adjusted coefficient of determination for each of the studied treatments. The p-value is equal to zero in all cases, indicating that the coefficients of the models are statistically significant at a significance level of one percent. The small standard deviation values of the coefficients, relative to the coefficient values, provide further evidence that the models' estimations can be trusted. Except for the T4 treatment, all other treatments have an R^2 value equal to or greater than 0.93, confirming the prediction reliability of the models. Hence, the results will be interpreted based on the estimations of the models.

Table 5- Coefficients, significance results, and coefficient of determination values for the Michaelis-Menten model

		T1	T2	T3	T4	T5	T6	T7	T8	T9
Coefficients	a	2566.0	2280.0	2158.5	1275.3	1562.9	1273.9	1325.3	893.0	736.1
	b	1.64	1.95	1.59	1.56	1.98	2.37	5.06	5.77	5.35
	c	11.50	9.83	10.76	17.46	8.41	6.50	13.31	12.90	12.62
Std	a	50.95	38.94	71.30	208.83	34.37	24.16	12.70	9.94	12.25
	b	0.07	0.10	0.12	0.35	0.16	0.26	0.29	0.44	0.59
	c	0.37	0.27	0.60	4.39	0.34	0.30	0.17	0.19	0.29
p-value	a	0.00	0.00	0.00	0.00	0.00	0.00	0.00	0.00	0.00
	b	0.00	0.00	0.00	0.00	0.00	0.00	0.00	0.00	0.00
	c	0.00	0.00	0.00	0.00	0.00	0.00	0.00	0.00	0.00
R^2	R^2	0.99	0.98	0.97	0.80	0.96	0.93	0.98	0.97	0.94
	$R^2_{Adj.}$	0.99	0.98	0.97	0.80	0.95	0.92	0.98	0.97	0.94

For a deeper understanding of the impact of coefficients in the Michaelis-Menten nonlinear regression model, a sensitivity analysis was conducted. Insights were gained by plotting the methane production trend during the digestion process and altering a single

coefficient at a time; the others were kept constant at their average values. The results of this analysis are presented in Fig. 2. The regression coefficient 'a' has a direct influence on the maximum methane production during the digestion process. Higher values of 'a' increased methane production, while lower values resulted in lower production. This coefficient represents the horizontal asymptote of the methane production curve. On the other hand, coefficient 'b' governs the slope of the methane production curve, impacting the time it takes to reach maximum methane production. A higher value of 'b' leads to a steeper slope and the methane production reaches its maximum more quickly. Conversely, an increase in coefficient 'c' slows down the rate of methane production, and requires a longer time to reach the maximum production level. Considering the behavior of these three regression coefficients, it can be concluded that the highest amount of methane production occurs when coefficients 'a' and 'b' are high, and coefficient 'c' is low. This combination results in faster methane production over a shorter period.

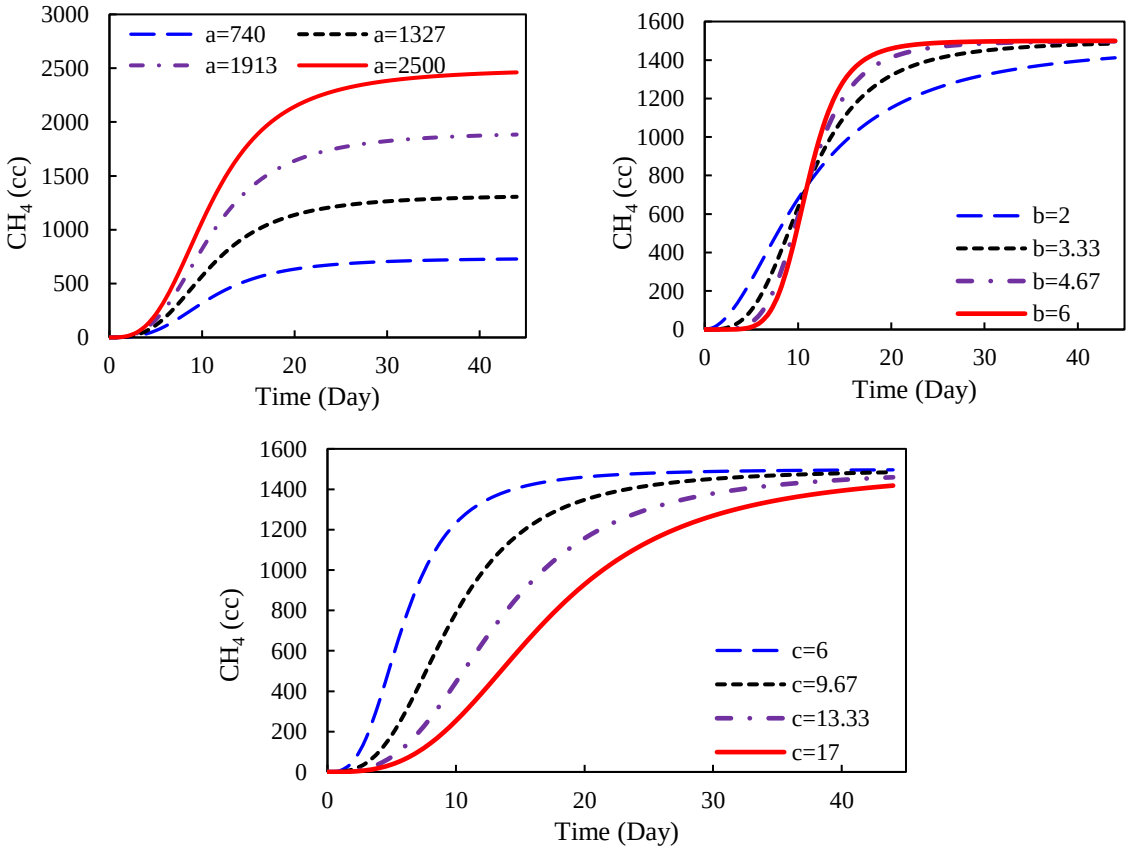

Fig.2. Sensitivity analysis investigating the effect of the Michaelis-Menten model coefficients a, b, and c on methane production

Fig. 3 presents the fitting outcomes of the Michaelis-Menten nonlinear regression model for all of the investigated treatments, along with the upper and lower limits of the fitted curve. The results indicate variations in the dispersion of experimental data among the different treatments, likely due to differences in experimental conditions. Nevertheless, considering the proximity of the upper and lower limits of the fitted curve and the model evaluation, it can be inferred that the fitted results effectively represent the variability of methane production within the studied treatments.

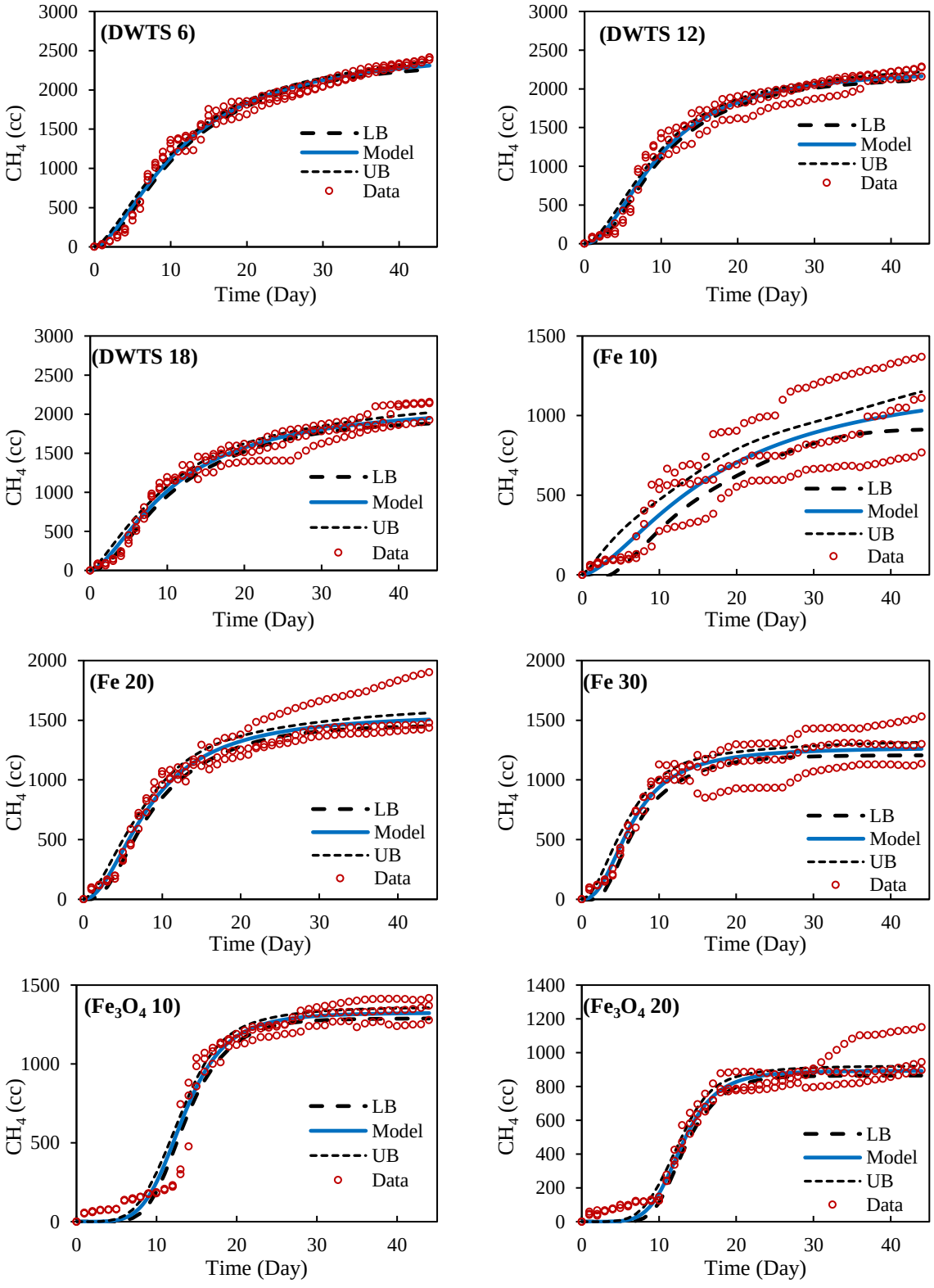
(DWTS 6)
(DWTS 12)
(DWTS 18)
(Fe 10)
(Fe 20)
(Fe 30)
(Fe3O4 10)
(Fe3O4 20)
CH4 (cc)
Time (Day)
LB
Model
UB
Data

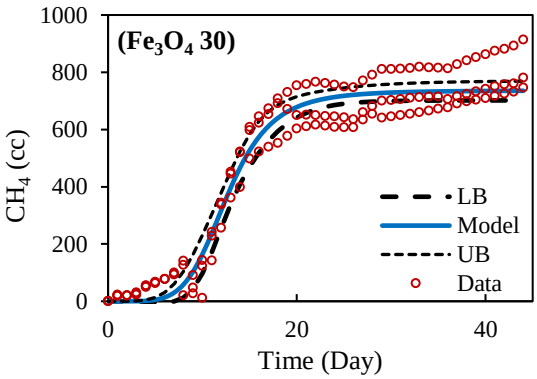

Fig.3. Curve fitting of the Michaelis-Menten nonlinear regression model for each of the studied treatments, showing the dispersion of experimental data and the upper (UB) and lower (LB) bounds of the fit

The final amount of methane production and its changes during the process were compared using non-linear regression models, as depicted in Fig. 4. Among the studied treatments, DWTS6, DWTS12, and DWTS18 showed the highest levels of methane production, while $Fe_3O_4$20 and $Fe_3O_4$30 resulted in the lowest levels. The maximum methane production for DWTS6 was approximately 34% and 42% higher than that of Fe20 and $Fe_3O_4$30, respectively, which were the best-performing levels among the Fe additives' treatments. This indicates that DWTS acts as a mixture of different trace elements with synergistic and antagonistic effects, resulting in an enhancement of methane production from dairy manure. Previous research by Ebrahimi-Nik *et al.* (2018) demonstrated that the addition of 6 mg/kg DWTS to the anaerobic digestion of food waste, compared to the control digester, resulted in a significant increase of 65% and 58% in biogas and methane yields, respectively. In Fig. 4 it is evident that until the 10th day of the digestion process, $Fe_3O_4$10 produced less methane than all levels of Fe. However, after the twelfth day, the methane production rapidly exceeded all levels of Fe, indicating a unique pattern of methane generation for $Fe_3O_4$10 compared to other levels of Fe. The addition of Fe_3O_4 to the anaerobic digestion (AD) process has been reported to have a significant positive effect on biogas yield. These additives also contribute to improving substrate digestibility by facilitating the decomposition of lignocellulosic biomass into simpler structures (Zhao *et al.*, 2017). Ali, Mahar, Soomro, & Sherazi (2017) observed a remarkable 72.1% increase in methane content when using municipal solid waste (MSW) as a substrate for the AD process with the addition of Fe_3O_4 nanoparticles. In another study, Abdelsalam *et al.* (2017) investigated the impact of iron nanoparticles and iron oxide nanoparticles on biogas and methane production using cattle dung slurry and found that Fe_3O_4 NPs with a concentration of 20 mg/L led to a substantial 65.6% increase in biogas production. Fe_3O_4 NPs additives have also been associated with the highest biogas yield reported from an AD process (Casals *et al.*, 2014). These findings highlight the potential and significance of Fe_3O_4-based additives in enhancing biogas production in anaerobic digestion processes. Regarding the slope of methane production, it is observed that the top two treatments, DWTS6 and DWTS12, have the same slope until day 20. However, after day 20, the methane production trend for DWTS6 rises above that of DWTS12. Generally, the slope of methane production varies among different treatments, with some showing an uphill start, which may also have a significant impact on their overall methane production.

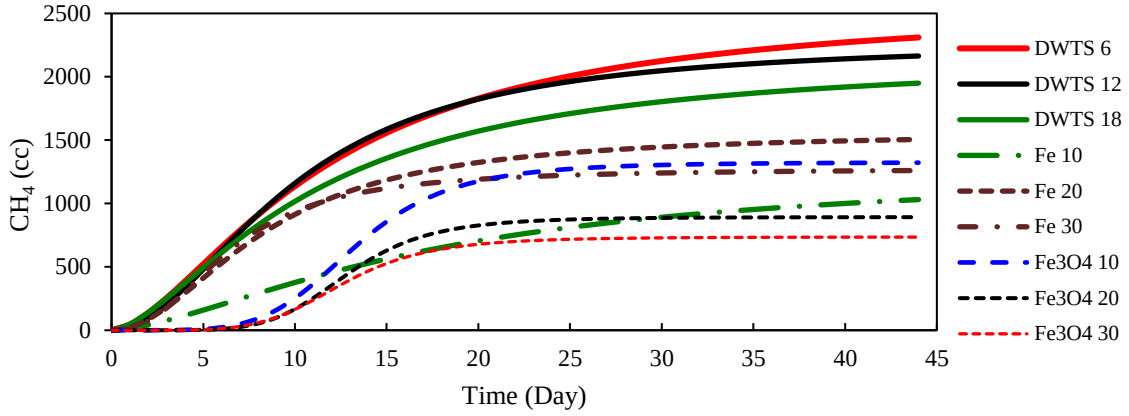

Fig.4. Methane production during the anaerobic digestion process using non-linear regression models for each of the treatments

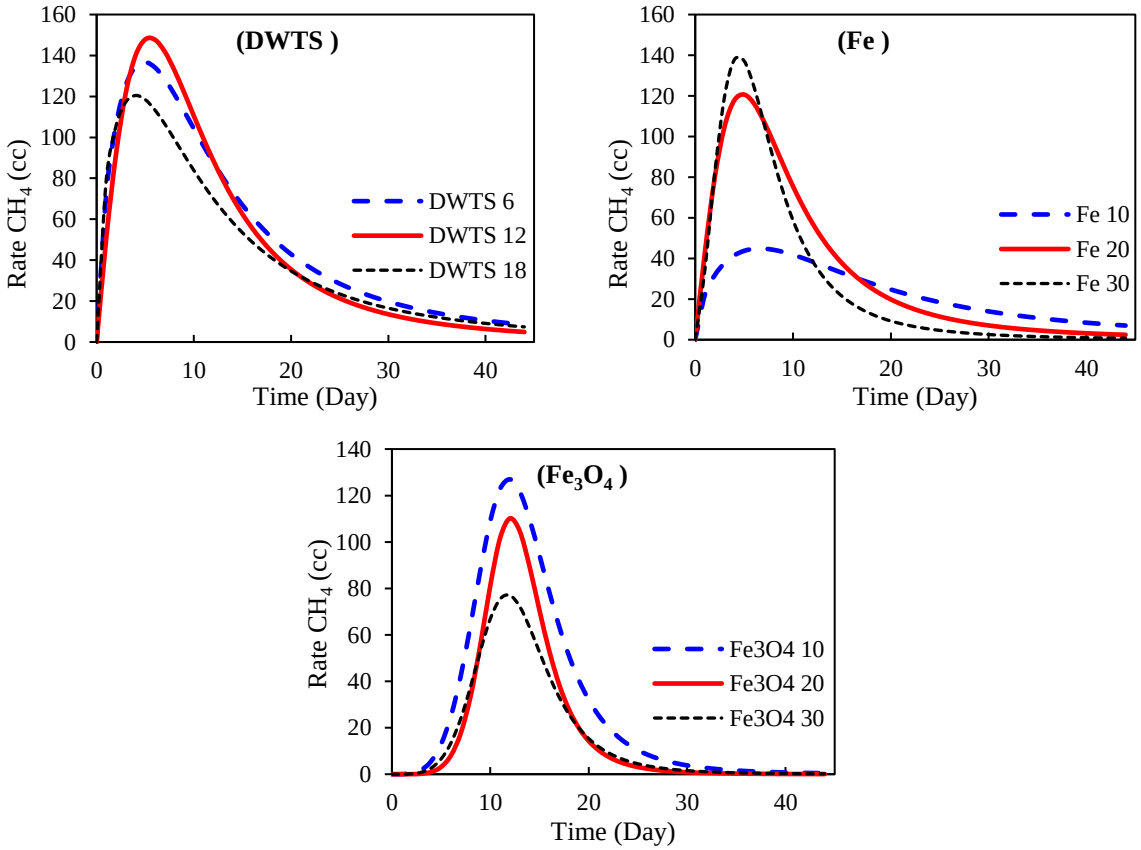

Fig.5. Changes in the production rate of methane during the anaerobic digestion process using a non-linear regression model for each of the three additives

Fig. 5 displays the methane production rate from the treatments throughout 40 days. Sigmoid gas production curves can be categorized into three stages: the initial stage with slow or no gas production, the rapid gas production stage (exponential stage), and the final stage where gas production slows down and eventually reaches zero (asymptotic stage). A comparison of the three types of treatments reveals that only the treatments with different levels of Fe_3O_4 experienced an initial stage. Consequently, these treatments

reached their maximum production rate after day ten, while other additives (DWTS and Fe) achieved their maximum rates before the 10th day. It was observed that a higher level of Fe_3O_4 corresponds to a lower methane production rate in all three stages. However, Fe20 and Fe30 exhibited increased methane rates in the first two stages. It is noteworthy that the lower level of Fe (Fe20) resulted in a higher methane production rate than Fe30 at the end of the process, particularly after the 18th day and during the third stage. When comparing different levels of DWTS, it was evident that although these treatments had similar rates during the first and final days of the process, DWTS12 exhibited the highest methane production rate during the rapid gas production stage. Specifically, the maximum methane production rate of DWTS12 in the second stage was approximately 5% and 22% higher than DWTS6 and DWTS18, respectively.

Abdelsalam *et al.* (2017) conducted a study on the impact of magnetic iron oxide nanoparticles on methane production from anaerobic digestion of manure. Their findings revealed that utilizing 20 mg L^{-1} of Fe_3O_4 resulted in the highest methane production rate, surpassing the rates observed with 5 mg L^{-1} and 10 mg L^{-1} of Fe_3O_4. The maximum methane production rate was achieved before the 5th day and reached approximately 110 cc for the AD process of food waste when 6 mg L^{-1} of DWTS was used. This result aligns closely with the findings obtained for the same treatment in one of our other studies (Ebrahimzadeh *et al.*, 2022).

Using the results obtained from the modeling analysis, we computed the quantity of methane production for each of the nine treatments at various points during the anaerobic digestion process. We calculated methane production when it reached 25%, 50%, 75%, and 90% of the final amount achieved at the end of the process. The computed values for T25, T50, T75, and T90 of each treatment are presented in Table 6. By examining these values for the treatments, we can determine the speed at which each treatment achieves its maximum methane production. Opting for a treatment that reaches its maximum methane production earlier with a higher percentage would be preferable, as it indicates a more efficient and effective process.

Table 6- Calculated methane production values for T25, T50, T75, and T90 for each treatment

Additive	Treatment	T25 (day)	T50 (day)	T75 (day)	T90 (day)
DWTS	DWTS 6	5.65	11.29	21.77	38.89
	DWTS 12	5.64	9.65	16.32	26.93
	DWTS 18	5.28	9.40	16.49	28.03
Fe	Fe 10	8.48	17.65	23.05	32.61
	Fe 20	4.73	7.94	13.20	21.57
	Fe 30	4.21	6.64	10.41	16.14
Fe_3O_4	Fe_3O_4 10	10.41	13.22	16.72	21.06
	Fe_3O_4 20	10.76	13.02	15.71	18.90
	Fe_3O_4 30	10.40	12.16	14.20	16.53

Notes: T25, T50, T75, and T90 represent the times when methane production reaches 25%, 50%, 75%, and 90% of the maximum amount achieved at the end of the anaerobic digestion process, respectively.

Lastly, Fig. 6 presents the comparison of average cumulative methane production among the studied treatments using the LSD method after the completion of the anaerobic digestion process. Notably, the figure highlights a significant difference ($P > 0.05$) in biomethane production between the different levels of DWTS, Fe, and Fe_3O_4. It can be seen that the treatment with DWTS6 exhibits the highest level of average cumulative methane production, and there is a statistically significant difference between this treatment and all the others, except DWTS12. This suggests that DWTS6 stands out as a particularly effective treatment for promoting methane production during the anaerobic

digestion process, warranting further consideration for practical applications.

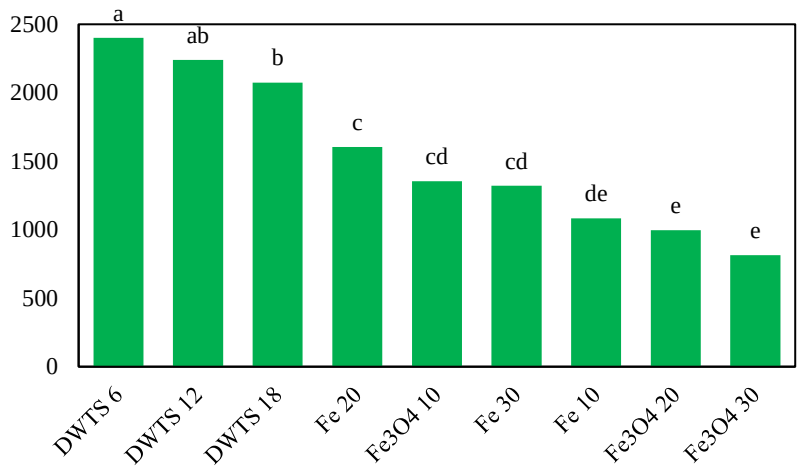

Fig.6. Comparison of average cumulative methane production among the treatments using the LSD method at 5% level after completion of the anaerobic digestion process

Conclusion

In this study, we investigated the impact of iron-based additives, including Fe, Fe_3O_4, and DWTS, at three levels, on the anaerobic digestion of dairy manure. Additionally, we introduced and evaluated 26 different non-linear models to better understand the kinetics of methane production from the AD process. Among these models, the Michaelis-Menten model (M8) demonstrated the best performance in estimating the methane production kinetics for all nine treatments over time.

The results revealed that different levels of DWTS exhibited the highest methane production compared to various levels of Fe and Fe_3O_4. Interestingly, Fe_3O_4 at level 30 displayed the lowest biomethane production among all the Fe_3O_4 treatments. Moreover, DWTS at level 6 achieved the highest average cumulative methane production among the studied treatments using the LSD method at a 5% significance level after the completion of the anaerobic digestion process.

The methane production rate for treatments with DWTS and Fe reached its maximum before the 5th day, while in Fe_3O_4 treatments, it occurred around the 12th day. Additionally, while higher levels of Fe increased the methane production rate, increasing the level of Fe_3O_4 showed the opposite effect. Notably, among all the treatments, DWTS at level 12 displayed the highest maximum methane production rate, peaking at approximately 147.6 cc on the 6th day.

These findings provide valuable insights into the kinetics of anaerobic digestion of dairy manure. However, further research is required to determine whether these results can be applied to other types of livestock manure as well. Future studies could involve applying the proposed models to different datasets to validate and refine our understanding of the anaerobic digestion process.

Acknowledgment

The authors acknowledge and appreciate the funding and technical support provided by the Ferdowsi University of Mashhad, Iran, for this project (Grant No. 49913).

Conflict of Interest

The authors declare that they have no conflict of interest.

References

1. Abdelsalam, E., Samer, M., Attia, Y., Abdel-Hadi, M., Hassan, H., & Badr, Y. (2016). Comparison of nanoparticles effects on biogas and methane production from anaerobic digestion of cattle dung slurry. *Renewable Energy, 87*, 592-598. https://doi.org/10.1016/j.renene.2015.10.053
2. Abdelsalam, E., Samer, M., Attia, Y. A., Abdel-Hadi, M. A., Hassan, H. E., & Badr, Y. (2017). Influence of zero valent iron nanoparticles and magnetic iron oxide nanoparticles on biogas and methane production from anaerobic digestion of manure. *Energy, 120*, 842-853. https://doi.org/10.1016/j.energy.2016.11.137
3. Ahmad, T., Ahmad, K., & Alam, M. (2016). Sustainable management of water treatment sludge through 3 'R'concept. *Journal of Cleaner Production, 124*, 1-13. https://doi.org/10.1016/j.jclepro.2016.02.073
4. Al Seadi, T., Rutz, D., Prassl, H., Köttner, M., Finsterwalder, T., Volk, S., & Janssen, R. (2008). Biogas Handbook; University of Southern Denmark Esbjerg: Esbjerg, Denmark, 2008. Google Scholar.
5. Ali, A., Mahar, R. B., Soomro, R. A., & Sherazi, S. T. H. (2017). Fe_3O_4 nanoparticles facilitated anaerobic digestion of organic fraction of municipal solid waste for enhancement of methane production. *Energy Sources, Part A: Recovery, Utilization, and Environmental Effects, 39*(16), 1815-1822. https://doi.org/10.1080/15567036.2017.1384866
6. Andriamanohiarisoamanana, F. J., Ihara, I., Yoshida, G., & Umetsu, K. (2020). Kinetic study of oxytetracycline and chlortetracycline inhibition in the anaerobic digestion of dairy manure. *Bioresource Technology, 315*, 123810. https://doi.org/10.1016/j.biortech.2020.123810
7. APHA. (2005). Standard Methods for the Examination of Water and Wastewater. 21st ed. American Public Health Association, Washington DC, 1220p.
8. Archontoulis, S. V., & Miguez, F. E. (2015). Nonlinear regression models and applications in agricultural research. *Agronomy Journal, 107*(2), 786-798. https://doi.org/10.2134/agronj2012.0506
9. Casals, E., Barrena, R., Garcia, A., González, E., Delgado, L., Busquets-Fité, M., Font Segura, X., Arbiol, J., Glatzel, P., Kvashnina, K., Sánchez, A., & Puntes, V. (2014). Programmed Iron Oxide Nanoparticles Disintegration in Anaerobic Digesters Boosts Biogas Production. Small (Weinheim an Der Bergstrasse, Germany), 10. https://doi.org/10.1002/smll.201303703
10. Chen, R., Konishi, Y., & Nomura, T. (2018). Enhancement of methane production by Methanosarcina barkeri using Fe_3O_4 nanoparticles as iron sustained release agent. *Advanced Powder Technology, 29*(10), 2429-2433. https://doi.org/10.1016/j.apt.2018.06.022
11. Cheng, J., Zhu, C., Zhu, J., Jing, X., Kong, F., & Zhang, C. (2020). Effects of waste rusted iron shavings on enhancing anaerobic digestion of food wastes and municipal sludge. *Journal of Cleaner Production, 242*, 118195. https://doi.org/10.1016/j.jclepro.2019.118195
12. Choong, Y. Y., Norli, I., Abdullah, A. Z., & Yhaya, M. F. (2016). Impacts of trace element supplementation on the performance of anaerobic digestion process: A critical review. *Bioresource Technology, 209*, 369-379. https://doi.org/10.1016/j.biortech.2016.03.028
13. Demirel, B., & Scherer, P. (2011). Trace element requirements of agricultural biogas digesters during biological conversion of renewable biomass to methane. *Biomass and Bioenergy, 35*(3), 992-998. https://doi.org/10.1016/j.biombioe.2010.12.022
14. Dudley, B. (2019). *BP statistical review of world energy 2016*. British Petroleum Statistical Review of World Energy, Bplc. editor, Pureprint Group Limited, UK.
15. Ebrahimi-Nik, M., Heidari, A., Azghandi, S. R., Mohammadi, F. A., & Younesi, H. (2018). Drinking water treatment sludge as an effective additive for biogas production from food waste; kinetic evaluation and biomethane potential test. *Bioresource Technology, 260*, 421-426. https://doi.org/10.1016/j.biortech.2018.03.112

16. Ebrahimzade, I., Ebrahimi-Nik, M., Rohani, A., & Tedesco, S. (2021). Higher energy conversion efficiency in anaerobic degradation of bioplastic by response surface methodology. *Journal of Cleaner Production, 290*, 125840. https://doi.org/10.1016/j.jclepro.2021.125840
17. Ebrahimzade, I., Ebrahimi-Nik, M., Rohani, A., & Tedesco, S. (2022). Towards monitoring biodegradation of starch-based bioplastic in anaerobic condition: Finding a proper kinetic model. *Bioresource Technology, 347*, 126661. https://doi.org/10.1016/j.biortech.2021.126661
18. Gkotsis, P., Kougias, P., Mitrakas, M., & Zouboulis, A. (2023). Biogas upgrading technologies–Recent advances in membrane-based processes. *International Journal of Hydrogen Energy, 48*(10), 3965-3993. https://doi.org/10.1016/j.ijhydene.2022.10.228
19. Hao, X., Wei, J., van Loosdrecht, M. C., & Cao, D. (2017). Analysing the mechanisms of sludge digestion enhanced by iron. *Water Research, 117*, 58-67. https://doi.org/10.1016/j.watres.2017.03.048
20. Holliger, C., Alves, M., Andrade, D., Angelidaki, I., Astals, S., Baier, U., Bougrier, C., Buffière, P., Carballa, M., & De Wilde, V. (2016). Towards a standardization of biomethane potential tests. *Water Science and Technology, 74*(11), 2515-2522. https://doi.org/10.2166/wst.2016.336
21. Huiliñir, C., Montalvo, S., & Guerrero, L. (2015). Biodegradability and methane production from secondary paper and pulp sludge: effect of fly ash and modeling. *Water Science and Technology, 72*(2), 230-237. https://doi.org/10.2166/wst.2015.210
22. Huiliñir, C., Pinto-Villegas, P., Castillo, A., Montalvo, S., & Guerrero, L. (2017). Biochemical methane potential from sewage sludge: Effect of an aerobic pretreatment and fly ash addition as source of trace elements. *Waste Management, 64*, 140-148. https://doi.org/10.1016/j.wasman.2017.03.023
23. Karki, R., Chuenchart, W., Surendra, K. C., Sung, S., Raskin, L., & Khanal, S. K. (2022). Anaerobic co-digestion of various organic wastes: Kinetic modeling and synergistic impact evaluation. *Bioresource Technology, 343*, 126063. https://doi.org/10.1016/j.biortech.2021.126063
24. Khamis, A. (2005). Nonlinear growth models for modeling oil palm yield growth. *Journal of Mathematics and Statistics, 1*(3), 225-233. https://doi.org/10.3844/jmssp.2005.225.232
25. Kong, X., Yu, S., Xu, S., Fang, W., Liu, J., & Li, H. (2018). Effect of FeO addition on volatile fatty acids evolution on anaerobic digestion at high organic loading rates. *Waste Management, 71*, 719-727. https://doi.org/10.1016/j.wasman.2017.03.019
26. Lima, D. R. S., Adarme, O. F. H., Baˆeta, B. E. L., Gurgel, L. V. A., & de Aquino, S. F. (2018). Influence of different thermal pretreatments and inoculum selection on the biomethanation of sugarcane bagasse by solid-state anaerobic digestion: A kinetic analysis. *Industrial Crops and Products, 111*, 684-693. https://doi.org/10.1016/j.indcrop.2017.11.048
27. Lu, J., & Gao, X. (2021). Biogas: Potential, challenges, and perspectives in a changing China. *Biomass and Bioenergy, 150*, 106127. https://doi.org/10.1016/j.biombioe.2021.106127
28. Muddasar, M. (2022). Biogas production from organic wastes and iron as an additive–a short review. Preprints.org 2022, 2022010026. https://doi.org/10.20944/preprints202201.0026.v1
29. Masih-Das, J., & Tao, W. (2018). Anaerobic co-digestion of foodwaste with liquid dairy manure or manure digestate: Co-substrate limitation and inhibition. *Journal of Environmental Management, 223*, 917-924. https://doi.org/10.1016/j.jenvman.2018.07.016
30. Noonari, A. A., Mahar, R. B., Sahito, A. R., & Brohi, K. M. (2019). Anaerobic co-digestion of canola straw and banana plant wastes with buffalo dung: Effect of Fe_3O_4 nanoparticles on methane yield. *Renewable Energy, 133*, 1046-1054. https://doi.org/10.1016/j.renene.2018.10.113
31. Pardilhó, S., Pires, J. C., Boaventura, R., Almeida, M., & Dias, J. M. (2022). Biogas production

from residual marine macroalgae biomass: Kinetic modeling approach. *Bioresource Technology, 359*, 127473. https://doi.org/10.1016/j.biortech.2022.127473
32. Raposo, F., De la Rubia, M., Fernández-Cegrí, V., & Borja, R. (2012). Anaerobic digestion of solid organic substrates in batch mode: an overview relating to methane yields and experimental procedures. *Renewable and Sustainable Energy Reviews, 16*(1), 861-877. https://doi.org/10.1016/j.rser.2011.09.008
33. Rosato, M. A. (2017). *Managing biogas plants: A practical guide*. CRC Press.
34. Schmidt, T., Nelles, M., Scholwin, F., & Proter, J. (2014). Trace element supplementation in the biogas production from wheat stillage– optimization of metal dosing. *Bioresource Technology, 168*, 80-85. https://doi.org/10.1016/j.biortech.2014.02.124
35. Stoddard, I. (2010). Communal polyethylene biogas systems: Experiences from on-farm research in rural West Java.
36. Torres-Lozada, P., Díaz-Granados, J. S., & Parra-Orobio, B. A. (2015). Effects of the incorporation of drinking water sludge on the anaerobic digestion of domestic wastewater sludge for methane production. *Water Science and Technology, 72*(6), 1016-1021. https://doi.org/10.2166/wst.2015.291
37. Wang, M., Tang, S. X., & Tan, Z. L. (2011). Modeling in vitro gas production kinetics: derivation of logistic–exponential (LE) equations and comparison of models. *Animal Feed Science and Technology, 165*(3-4), 137-150. https://doi.org/10.1016/j.anifeedsci.2010.09.016
38. Wang, K., Yun, S., Xing, T., Li, B., Abbas, Y., & Liu, X. (2021). Binary and ternary trace elements to enhance anaerobic digestion of cattle manure: Focusing on kinetic models for biogas production and digestate utilization. *Bioresource Technology, 323*, 124571. https://doi.org/10.1016/j.biortech.2020.124571
39. Wellinger, A., Murphy, J. D., & Baxter, D. (2013). *The biogas handbook: science, production and applications*. Elsevier.
40. Zareei, S. (2018). Evaluation of biogas potential from livestock manures and rural wastes using GIS in Iran. *Renewable Energy, 118*, 351-356. https://doi.org/10.1016/j.renene.2017.11.026
41. Zhang, Y., Feng, Y., Yu, Q., Xu, Z., & Quan, X. (2014). Enhanced high-solids anaerobic digestion of waste activated sludge by the addition of scrap iron. *Bioresource Technology, 159*, 297-304. https://doi.org/10.1016/j.biortech.2014.02.114
42. Zhao, Z., Li, Y., Quan, X., & Zhang, Y. (2017). Towards engineering application: Potential mechanism for enhancing anaerobic digestion of complex organic waste with different types of conductive materials. *Water Research, 115*, 266-277. https://doi.org/10.1016/j.watres.2017.02.067

نشریه ماشین‌های کشاورزی
https://jame.um.ac.ir

مقاله پژوهشی

جلد ۱٤، شماره ۱، بهار ۱٤۰۳، ص ۳٤-۱۵

بررسی کارایی افزودنی‌های بر پایه آهن در هضم بی‌هوازی کودهای دامی: مطالعه مدل‌سازی سینتیک

جواد رضائی فر[۱]، عباس روحانی[۱*]، محمدعلی ابراهیمی نیک[۱]

تاریخ دریافت: ۱۴۰۲/۰۴/۰۷
تاریخ پذیرش: ۱۴۰۲/۰۵/۰۷

چکیده

در تلاش برای بهبود عملکرد و پایداری هضم بی‌هوازی (AD)، افزودنی‌های مبتنی بر آهن به‌عنوان ریزمغذی‌ها و لجن تصفیه آب آشامیدنی (DWTS) می‌توانند نقش کلیدی داشته باشند. این مطالعه به بررسی سینتیک تولید متان در طول AD کودهای گاوی می‌پردازد که شامل غلظت‌های مختلف Fe و Fe_3O_4 (۱۰، ۲۰ و ۳۰ میلی‌گرم در لیتر) و DWTS (۶، ۱۲ و ۱۸ میلی‌گرم در لیتر) می‌شود. با استفاده از یک کتابخانه گسترده از مدل‌های رگرسیون غیرخطی (NLR)، ۲۶ نامزد مورد بررسی قرار گرفتند و هشت مورد به‌عنوان پیش‌بینی‌کننده‌های قوی برای کل فرآیند تولید متان ظاهر شدند. مدل Michaelis-Menten به‌عنوان انتخاب برتر برجسته شد و سینتیک کودهای دامی AD را با افزودنی‌های مشخص‌شده آشکار کرد. یافته‌ها نشان داد که سطوح مختلف DWTS بالاترین تولید متان را به‌همراه دارد، در حالی‌که $Fe_3O_4$20 و $Fe_3O_4$30 کمترین میزان را ثبت کردند. قابل‌ذکر است، DWTS6 تولید متان تقریباً ۳۴٪ و ۴۲٪ را در مقایسه با Fe20 و $Fe_3O_4$30 نشان داد و آن را به‌عنوان موثرترین تیمار معرفی کرد. علاوه بر این، DWTS12 بالاترین میزان تولید متان را به نمایش گذاشت و به ۱۴۷/۶ سی‌سی در روز ششم رسید. با تأکید بر مفاهیم عملی، این تحقیق بر کاربرد مدل پیشنهادی برای تجزیه و تحلیل سایر پارامترها و بهینه‌سازی عملکرد AD تأکید می‌کند. این مطالعه با بررسی پتانسیل افزودنی های مبتنی بر آهن و DWTS، مسیر را در تولید متان از کودهای گاوی و پیشبرد شیوه‌های مدیریت زباله پایدار هموار می‌سازد.

واژه‌های کلیدی: عناصر کمیاب، کود دامی، مدل‌سازی، مطالعه سینتیک، هضم بی‌هوازی

۱- گروه مهندسی بیوسیستم، دانشکده کشاورزی، دانشگاه فردوسی مشهد، مشهد، ایران
(*- نویسنده مسئول: Email: arohani@um.ac.ir)

https://doi.org/10.22067/jam.2023.83173.1176

Journal of Agricultural Machinery

Homepage: https://jame.um.ac.ir

Research Article
Vol. 14, No. 1, Spring 2024, p. 35-47

Optimization of the Mixing in a Gas-lift Anaerobic Digester of Municipal Wastewater Sludge

D. Baveli Bahmaei[1], Y. Ajabshirchi[2], Sh. Abdollahpour[3*], S. Abdanan Mehdizadeh[4]

1- PhD Student, Department of Biosystems Engineering, Faculty of Agriculture, University of Tabriz, Tabriz, Iran
2- Professor, Department of Biosystems Engineering, Faculty of Agriculture, University of Tabriz, Tabriz, Iran
3- Associate Professor, Department of Biosystems Engineering, Faculty of Agriculture, University of Tabriz, Tabriz, Iran
4- Associate Professor, Department of Mechanics of Biosystems Engineering, Faculty of Agricultural Engineering and Rural Development, Agricultural Sciences and Natural Resources University of Khuzestan, Ahvaz, Iran
(*- Corresponding Author Email: shams@tabrizu.ac.ir)

Received: 28 July 2023
Revised: 12 September 2023
Accepted: 02 October 2023
Available Online: 02 October 2023

How to cite this article:
Baveli Bahmaei, D., Ajabshirchi, Y., Abdollahpour, Sh., & Abdanan Mehdizadeh, S. (2024). Optimization of the Mixing in a Gas-lift Anaerobic Digester of Municipal Wastewater Sludge. *Journal of Agricultural Machinery, 14*(1), 35-47. https://doi.org/10.22067/jam.2023.83626.1182

Abstract

This research aims to optimize the mixing process in gas-lift anaerobic digesters of municipal sewage sludge since mixing and maintaining uniform contact between methanogenic bacteria and nutrients is essential. Wastewater municipal sludge sampling was performed at the Ahvaz West treatment plant (Chonibeh, Iran) during the summer of 2022. A Computational Fluid Dynamics (CFD) model was implemented to simulate, optimize, and confirm the simulation process using ANSYS Fluent software 19.0. The velocity of the inlet-gas into the digester was determined and a draft tube and a conical hanging baffle were added to the digester design. Different inlet-gas velocities were investigated to optimize the mixing in the digester. Furthermore, turbulence kinetic energy and other evaluation indexes related to the sludge particles such as their velocity, velocity gradient, and eddy viscosity were studied. The optimal inlet-gas velocity was determined to be 0.3 ms^{-1}. The simulation results were validated using the Particle Image Velocimetry (PIV) method and the correlation between CFD and PIV contours was statistically sufficient (98.8% at the bottom corner of the digester's wall). The results showed that the model used for simulating, optimizing, and verifying the simulation process is valid. It can be recommended for gas-lift anaerobic digesters with the following specifications: cylindrical tank with a height-to-diameter ratio of 1.5, draft tube-to-digester diameter ratio of 0.2, draft tube-to-fluid height ratio of 0.75, the conical hanging baffle distance from the fluid level equal to 0.125 of the fluid height, and its outer diameter-to-digester diameter of 2/3.

Keywords: Computational Fluid Dynamics (CFD), Digestion, Particles Image Velocimetry (PIV), Simulation

Introduction

The performance of an anaerobic digester is affected by several factors, including the retention time of the substrate within the digester and the degree of contact between the incoming substrate and the viable bacterial population. These parameters are determined by the flow pattern, or mixing, in the digester. Complete mixing of the substrate within the digester facilitates the uniform distribution of organisms and heat transfer. This is considered to be essential in high-rate anaerobic digesters (Sawyer & Grumbling, 1960; Meynell, 1976).

Three methods for mixing in anaerobic digesters include gas mixing, mechanical mixing, and pumped recirculation liquid. Gas

https://doi.org/10.22067/jam.2023.83626.1182

mixing can be performed using either unconfined or confined methods. In unconfined systems, biogas collected at the top of the digester is compressed and discharged through bottom diffusers or top-mounted lances (McFarland, 2001). To make the four gas mixing designs (Bottom diffusers, Gas lift, Cover mounted lances, and Bubble guns) comparable, MEL= 5 Wm^{-3} at TS= 5.4% was used to determine the velocity of the inlet gas. In confined systems, the biogas is released through tubes. The gas lift method in a confined system produces the highest average velocity (0.080 ms^{-1}) under the same mixing power (5 Wm^{-3}). In other words, mixing with the gas lift requires the lowest mixing power under the same average velocity of the flow field, and is the preferred method (Wu, 2014).

The flow pattern, or mixing, inside gas-mixed digesters is affected by several factors including the biogas recycling rate, the clearance of the draft tube at the bottom, the ratio of the draft tube to tank diameter, the slope of the hopper bottom, the position and design of the biogas injection (sparger), and the solids loading rate (Karim *et al*., 2005). Wei, Uijttewaal, Spanjers, Lier, & Kreuk (2023) assessed the impact on the treated sludge's rheology as an important factor affecting the flow optimization and mixing characterization in a full-scale biogas-mixed digester.

Conducting experiments to evaluate the effect of these parameters on mixing in the digester is time-consuming and costly. Therefore, simulation software like ANSYS Fluent is a suitable tool for designing and optimizing mixed gas anaerobic digesters. Wu (2010) presented an Eulerian multiphase flow model for mixing gas in digesters and proposed that the Shear Stress Transport (SST) k–w model with Low-Reynolds corrections would be an appropriate turbulence model to solve gas and non-Newtonian two-phase flows.

Researchers use different indexes to assess the performance of their simulations and to be able to evaluate simulations performed with experimental data. Varma & Al-Dahhan (2007) measured the turbulence kinetic energy and the velocity. Karim, Thoma, & Al-Dahhan (2007) measured the magnitude of axial velocity. Wu (2010) studied the velocity contour, Wu (2014) used the average velocity and the uniformity index of velocity to evaluate the mixing performance, and Daplo *et al.* (2015) used the magnitude of velocity along the vertical axis.

Validating the CFD simulation results is a necessary step. Tracer and non-invasive techniques are the traditional methods of studying gas mixing in anaerobic digesters and are usually used for verifying the CFD simulation results. Vesvikar & Al-Dahhan (2016), Karim *et al*. (2007), and Wu (2010) validated their models against the digester reported by Karim, Varma, Vesvikar, & Al-Dahhan (2004) and verified the flow fields with the measured data from Computer Automated Radioactive Particle Tracking (CARPT) and Computed Tomography (CT), a non-invasive technique. Dapelo, Alberini, & Bridgeman (2015) used Particle image velocimetry and a high-speed camera to validate an Euler-Lagrange CFD model of unconfined gas mixing in an anaerobic digestion. Hu *et al.* (2021) proposed a novel approach for experimental quantification of mass transfer in a high-solid anaerobic digestor's mixing process using Laser Induced Fluorescence (LIF) technique in a mixing tank equipped with multistage impellers. Flow field was investigated for a better illustration of the mass transfer, thus Particle Image Velocimetry (PIV) and Computational Fluid Dynamics (CFD) techniques were conducted for flow field measurement.

The quality of mixing in a gas-lift anaerobic digester depends on various factors, such as the dimensions of the draft tube and the conical hanging baffle, the position of the baffle relative to the digester bottom, and the angle of the baffle. Baveli Bahmaei, Ajabshirchi, Abdollah poor, & Abdanan Mehdizadeh (2022) performed a numerical study and examined the influence of these factors on the mixing performance using ANSYS Fluent software. The present paper

extends their work by optimizing the mixing using the same digester configuration with different inlet-gas velocities. The evaluation criteria for optimization are average velocity, turbulence kinetic energy, average velocity gradient, and eddy viscosity of the sludge. The numerical results are validated using particle image velocimetry (PIV).

Materials and Methods

Methodology

The Computational Fluid Dynamics (CFD) simulations were conducted using ANSYS Fluent software for modeling the inlet-gas anaerobic digester. The initial step involved determining the inlet-gas velocity. Subsequently, the effects of adding the draft tube and the conical hanging baffle to the digester design were analyzed. The optimization of mixing within the digester was achieved by varying the inlet-gas velocities and assessing the change in the evaluation indexes. The turbulence kinetic energy and the behavior of the sludge particles, namely their velocity, velocity gradient, and eddy viscosity were the studied indexes. The contours of the resulting evaluation indexes were analyzed to determine the optimal velocity for mixing. Following the simulation results, a transparent anaerobic digester was constructed and loaded with municipal sewage sludge, operating at optimal inlet-gas velocity. The Particle Image Velocimetry (PIV) method was employed to compare the evaluated index contours of PIV with those of the CFD and to validate the CFD simulation outcomes. A schematic representation of the simulation, optimization, and verification process is presented in Fig. 1.

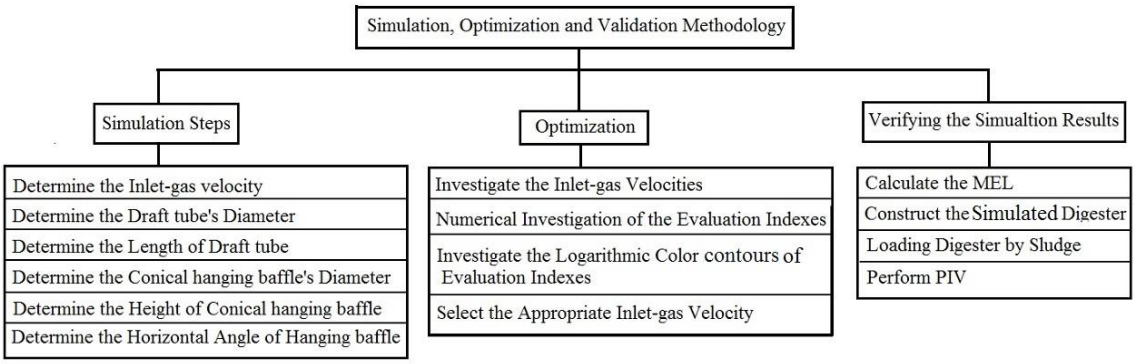

Fig.1. Steps used for the model simulation, optimization, and verification

CFD simulation

A commercial CFD software, ANSYS Fluent (version 19.0) was utilized to create a two-dimensional geometry in the design modeler, generate mesh, and solve the two-phase Eulerian model flow using the Eulerian multiphase approach. This two-dimensional model can be applied to digesters that are symmetrical around their vertical axis, like cylinders (Yang *et al.*, 2015). Simulations were performed under unsteady-state conditions using Double Precision, Serial, Pressure-Based, and Implicit settings. The two-phase liquid-gas Eulerian Model of Viscous-SST k-omega (with sludge as the primary phase and biogas as the secondary phase) and low-Re correction were employed. At each time step, the iterative calculation was accepted as converged if all residuals fell below 1×10^{-3}. Final convergence was achieved when the average velocity of the liquid phase remained unchanged (Wu, 2014).

Geometry, Computational domain, and mesh

The geometry of the digester used in this research is based on a previously simulated geometry by Baveli Bahmaei *et al*. (2022) and the six steps of digester simulation are outlined in Fig. 1. The digester consists of a cylindrical tank with a flat bottom, height of 45 cm, and a diameter of 30 cm which results in a height to

diameter ratio of 1.5. The draft tube diameter to digester diameter is 0.2 (5 cm) and the draft tube height to fluid height is 0.75 (30 cm). The conical hanging baffle distance from the fluid level is equal to 0.125 of the fluid height (5 cm), its outer diameter to digester diameter is 2/3 (20 cm) and has a horizontal angle of 15 degrees (Fig. 2). The mesh size function was set to curative, max face size was set to 0.0007, and the number of nodes and elements were 267083 and 264281, respectively. Discretization error estimation was calculated based on the method proposed by Celik *et al.* (2008).

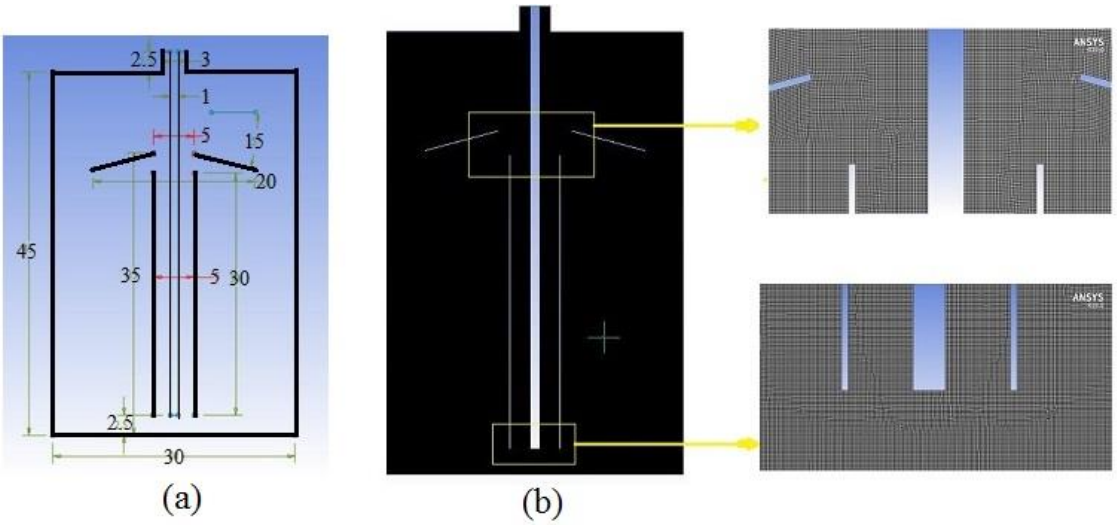

Fig.2. The digester used for mixing optimization: (a) Geometry, and (b) Meshing; values are in cm and degrees

Evaluation indexes

Sludge velocity

The velocity contour and streamlines were utilized in steps 1 to 6 of the simulation (Fig. 1) to determine the inlet-gas velocity, draft tube, and conical hanging baffle characteristics. The uniformity of contours and streamlines, as well as their contribution to uniformity within the digester, were considered (please refer to Baveli Bahmaei *et al.* (2022) for more details). Sludge velocity was used as one of the validation indexes for investigating the mixing quality in a simulated gas-lift anaerobic digester and for selecting the appropriate inlet-gas velocity. The velocity value was compared with the sludge's sedimentation velocity. Whenever the velocity was less than the sedimentation velocity, it indicated that the sludge particles would sediment in the digester.

Sludge velocity gradient

The sludge velocity gradient was used as a validation index for assessing the quality of mixing. This parameter is defined as a custom field function in the main menu of ANSYS Fluent as shown in Eq. 1 and measures the local velocity gradient of a mixture in multiphase flow using the SST k-w model as defined by Wu (2014).

$$G_L = \sqrt{\frac{\rho\omega\beta^* k}{\eta}} \quad (1)$$

Where ρ and η are the density and the non-Newtonian viscosity in the liquid phase, respectively. β^* is 0.09 and ω and k are the specific dissipation rate and the turbulence kinetic energy of the mixture, respectively. G_L is the local velocity gradient and will be called the velocity gradient hereafter.

Turbulence kinetic energy

Turbulence kinetic energy is used as one of the indexes that investigates the mixing quality in simulation results and is defined in Eq. 2.

$$G_k = -\rho\overline{u_i' u_j'}\frac{\partial u_j}{\partial x_i} \quad (2)$$

Reynolds stresses ($-\rho\overline{u_i' u_j'}$) is defined in Eq. 3 using the Boussinesq hypothesis related to the mean velocity gradient.

$$-\rho\overline{u_i' u_j'} = \mu_t\left(\frac{\partial u_i}{\partial x_j} + \frac{\partial u_j}{\partial x_i}\right) - \frac{2}{3}\left(\rho k + \mu_t\frac{\partial u_i}{\partial x_i}\right)\delta_{ij} \quad (3)$$

Where μ_t is the turbulent viscosity, k is the turbulence kinetic energy, and u (Eq. 4) is the velocity component.

$$u_i = \bar{u}_i + u_i' \quad (4)$$

Where $\bar{u}_i$ and u_i' are the mean and fluctuating velocity components respectively (i=1, 2, 3).

Sludge eddy viscosity

Mixing quality can also be investigated using sludge eddy viscosity. Sludge eddy viscosity is the proportionality factor in describing the turbulent energy transfer in the form of moving eddies, giving rise to tangential stresses. Eddy viscosity is defined in Eq. 5 (Menter, 1993):

$$v_T = \frac{\mu_T}{\rho} = \frac{k}{\omega} \quad (5)$$

Mixing Energy Level

The Mixing Energy Level (MEL) can be estimated using Eq. 6 (Stukenberg, Clark, Sandino, & Naydo, 1992).

$$MEL = \frac{E}{V} \quad (6)$$

Where V denotes the effective volume of the digester and E denotes the energy consumption. Energy consumption for the gas-sparging (Eq. 7) was evaluated based on the power input formula (McFarland, 2001).

$$E = P_1 \cdot Q \cdot ln\left(\frac{P_2}{P_1}\right) \quad (7)$$

Where Q denotes the gas flow rate, and P_1 and P_2 are the absolute pressure in the tank headspace and at the gas-sparging inlet, respectively.

Particle image velocimetry

According to the methods used by Raffel, Willert, & Kompenhans (1998) and Dawkins, Cain, & Roberts (2012), the particle image velocimetry (PIV) process involves taking two images (I_1 and I_2) separated by time Δt. Both images were then divided into smaller regions, also known as sub-windows, interrogation-windows, or interrogation-regions. Each sub-window in the first image is compared with the corresponding sub-window in the second image. The sub-window with position indexes i and j in the first image is denoted as $I_1^{i.j}$ and the corresponding sub-window in the second image is denoted as $I_2^{i.j}$. Afterward, a search algorithm was performed to identify a displacement pattern in $I_1^{i.j}$. To do this, the squared Euclidean distance between the two sub-windows was defined in Eq. 8.

$$R_e(s.t) = \sum_{m=0}^{M-1}\sum_{n=0}^{N-1}\left[I_1^{i.j}(m.n) - I_2^{i.j}(m-s.n-t)\right]^2 \quad (8)$$

This formula calculates the sum of the squared differences between all of the possible $I_1^{i.j}$ and $I_2^{i.j}$ sub-windows. In other words, it looks for the position where the sub-windows were the "least unlike". Expanding the square parentheses in Eq. 8 would result in Eq. 9.

$$\begin{aligned} R_e(s.t) = &\sum_{m=0}^{M-1}\sum_{n=0}^{N-1}\left[I_1^{i.j}(s.t) - I_2^{i.j}(m-s.n-t)\right]^2 \\ = &\sum_{m=0}^{M-1}\sum_{n=0}^{N-1} I_1^{i.j}(m.n)^2 \\ &- 2I_1^{i.j}(s.t) \cdot I_2^{i.j}(m-s.n-t) \\ &+ I_2^{i.j}(m-s.n-t)^2 \end{aligned} \quad (9)$$

It should be noted that the first term, $I_1^{i.j}(m.n)^2$, is a constant since it does not depend on s or t. The last term, $I_2^{i.j}(m-s.n-t)^2$, depends on s, t, and only the second

image. To sum up, only the middle term deals with both of the images and this term (without the -2), as defined in Eq. 10, is usually referred to as cross-correlation (or circular cross-correlation).

$$R(s.t) = \sum_{m=0}^{M-1}\sum_{n=0}^{N-1} I_1^{i.j}(m.n) \cdot I_2^{i.j}(m-s.n-t) \quad (10)$$

Results and Discussion

The mixing conditions in the digester were investigated using different inlet-gas velocities. Simulations were performed using inlet-gas velocities of 0.05, 0.1, 0.2, 0.3, 0.4, 0.5, and 0.6 ms^{-1} to study the mixing quality in a cylindrical digester, details of which are indicated in Fig. 2.

Investigation of the evaluation indexes

The values of the investigated indexes and Mixing Energy Levels (MEL) for each of the gas-inlet velocities are shown in Table 1.

Table 1- Evaluated indexes and MEL for verifying the mixing quality in the gas-lift anaerobic digester for different inlet-gas velocities

Inlet-gas velocity (ms^{-1})	Sludge velocity (ms^{-1})			Turbulence kinetic energy (m^2s^{-2})		Average velocity gradient (s^{-1})		Sludge eddy viscosity (Pa s)		MEL
	min. E-6	Ave.	max.	min. E-14	max.	min. E-6	max.	min. E-17	max.	
0.05	2.23	0.0236	0.30	1.0	3.8E-07	6.6	0.07	5.85	3.0E-08	0.505
0.1	10.72	0.0291	0.43	1.0	8.3E-07	18	0.14	5.91	8.0E-07	1.01
0.2	1.40	0.0287	0.66	1.0	64E-07	29	0.29	7.75	1.8E-05	2.02
0.3	2.61	0.0322	0.83	8.1	0.011	359	285.23	64.50	73E-05	3.03
0.4	3.92	0.0375	1.16	120	0.17	1398	449.68	974.12	0.65	4.04
0.5	2.26	0.0443	1.29	4400	0.21	8370	536.97	34911.40	0.63	5.05
0.6	9.53	0.0453	1.49	1900	0.26	5461	672.24	14858.50	0.74	6.06

Sludge velocity

Table 1 shows the minimum, average, and maximum values of sludge velocity for different inlet-gas velocities. The minimum sludge velocities were achieved in local and face options. The maximum velocity appears inside the draft tube, while the minimum value appears near the digester walls and at the bottom. The maximum velocity varies from 0.3 to 1.49 ms^{-1} for the studied inlet velocities and the average velocity only varies about 0.022 ms^{-1}. This indicates that the velocity of the particles in all internal parts of the digester does not increase proportionally with the increase in the inlet-gas velocity. This could be due to the formation of short-circuiting in the digester in areas where more mixing takes place. Because sludge is a non-Newtonian fluid and more mixing causes more decrease in its viscosity.

Since the maximum sedimentation velocity in sludge particles is 4.7E-5 ms^{-1} (Baveli Bahmaei *et al*., 2022), to prevent particle sedimentation, the minimum sludge velocity should be greater than 4.7E-5 ms^{-1}. However, when considering the minimum fluid velocities at different inlet-gas velocities, this goal is not achieved thoroughly at any of the studied inlet-gas velocities. On the other hand, increasing the inlet-gas velocity in gas-lift anaerobic digesters is limited due to the biological nature of anaerobic digestion. Therefore, a balance must be struck between increasing the mixing rate and reducing the particle sedimentation to maintain the conditions that prevent disruption of the biological process of anaerobic digestion.

Turbulence kinetic energy

The minimum and maximum values of turbulence kinetic energy for different inlet-gas velocities are shown in Table 1. Minimum turbulence kinetic energy varies between 1E-14 and 4.4E-11 m^2s^{-2} for inlet-gas velocities of

0.05 and 0.5 ms^{-1}, respectively and the maximum varies from 3.8E-7 m^2s^{-2} in 0.05 ms^{-1} velocity to 0.26 m^2s^{-2} in 0.6 ms^{-1} velocity. The produced turbulence kinetic energy is very low for the first three inlet-gas velocities (0.05, 0.1, and 0.2 ms^{-1}), has a medium value for the inlet-gas velocity of 0.3 ms^{-1}, and is high with close values for the remaining three velocities (0.4, 0.5, and 0.6 ms^{-1}). Turbulence kinetic energy of different inlet-gas velocities is presented in Fig. 3. Higher turbulence kinetic energy causes more intense mixing and the destruction of flocs, which disrupts the anaerobic digestion process.

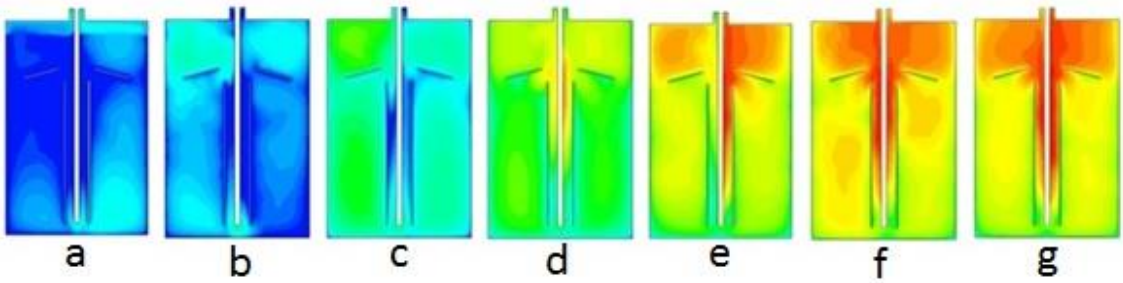

Fig.3. Turbulence kinetic energy contours (logarithmic color) for different inlet-gas velocities; (a) 0.05, (b) 0.1, (c) 0.2, (d) 0.3, (e) 0.4, (f) 0.5, and (g) 0.6 ms^{-1}

Average velocity gradient

The average velocity gradient generates the turbulence kinetic energy and therefore, their results are similar. Results of the average velocity gradient for the studied inlet-gas velocities are presented in Fig. 4. The minimum average velocity gradient varies from 6.6E-12 to 84E-10 s^{-1} for different inlet-gas velocities (Table 1). The maximum average velocity gradient varies from 0.07 to 672.24 s^{-1} for inlet-gas velocities of 0.05 to 0.6 ms^{-1}. The average velocity gradient is low for the first three inlet-gas velocities (0.05, 0.1, and 0.2 ms^{-1}) and high for the last three of them (0.4, 0.5, and 0.6 ms^{-1}). It has a medium value for the inlet-gas velocity of 0.3 ms^{-1}.

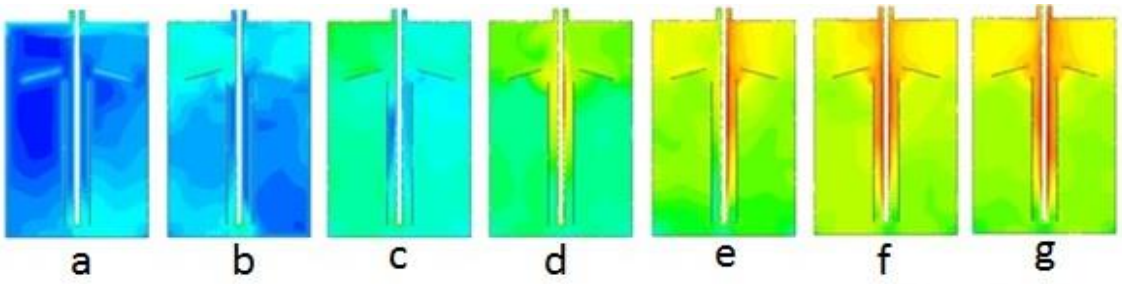

Fig.4. Average velocity gradient contours (logarithmic color) for different inlet-gas velocities; (a) 0.05, (b) 0.1, (c) 0.2, (d) 0.3, (e) 0.4, (f) 0.5, and (g) 0.6 ms^{-1}

Sludge eddy viscosity

Sludge eddy viscosity is a proportionality factor describing the turbulent energy transfer as a result of moving eddies, giving rise to tangential stresses. The results of sludge eddy viscosity for different inlet-gas velocities are presented in Fig. 5. The minimum and maximum values of sludge eddy viscosity for different inlet-gas velocities are shown in Table 1. Minimum sludge eddy viscosity varies from 5.85E-17 to 14.86E-14 Pa s, and the maximum varies from 3.0E-8 to 0.74 Pa s as the velocity increases from 0.05 to 0.6 ms^{-1}. Sludge eddy viscosity produced by the first four inlet-gas velocities (0.05, 0.1, 0.2, and 0.3 ms^{-1}) has low values and the last three velocities (0.4, 0.5, and 0.6) are high and have close values**.** Higher eddy viscosity indicates higher amounts of moving eddies and high tangential stresses in the sludge that can lead to the destruction of flocs and disrupt the biological process of digestion. Therefore, in

terms of sludge eddy viscosity index, an inlet-gas velocity of 0.3 ms^{-1} was appropriate.

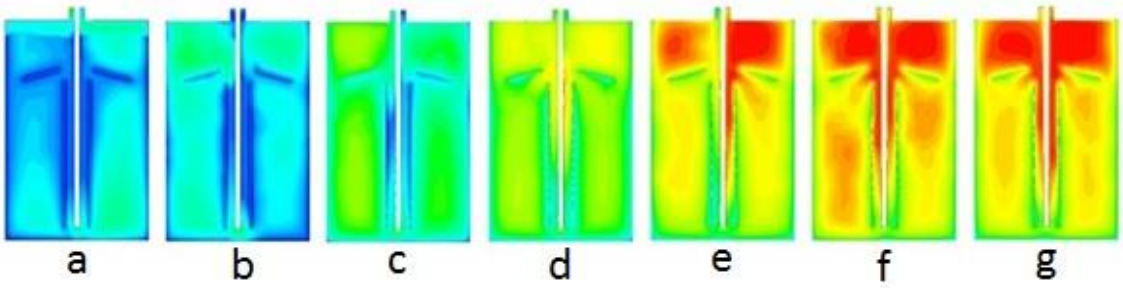

Fig.5. Sludge eddy viscosity contours (logarithmic color) for different inlet-gas velocities; (a) 0.05, (b) 0.1, (c) 0.2, (d) 0.3, (e) 0.4, (f) 0.5, and (g) 0.6 ms^{-1}

Selecting the appropriate inlet-gas velocity

The investigation of the evaluation indexes revealed that a balance between the mixing intensity and sludge sedimentation must be maintained. Higher mixing intensity can result in broken flocs and impairs anaerobic digestion. If a high inlet-gas velocity is selected for mixing, it can disrupt the biological process of anaerobic digestion. On the other hand, if the velocity is too low, the particle sedimentation rate will increase and proper mixing will not occur.

Analyzing sludge velocity, turbulence kinetic energy, average velocity gradient, and eddy viscosity showed that selecting an inlet-gas velocity of 0.3 ms^{-1} is the most appropriate option. The results of CFD simulations for the investigated evaluation indexes for an inlet-gas velocity of 0.3 ms^{-1} are shown in Fig. 6.

The sludge velocity contour presented in Fig. 6 indicates that in most of the digester zones, zones 4 and 5 with yellow and red colors, the particle velocity is greater than 1.75E-3 ms^{-1}. Considering the maximum sludge sedimentation velocity for the largest sludge particle (47 E-6 ms^{-1} for particle size of 2 mm) (Baveli Bahmaei *et al.*, 2022), particle sedimentation in the digester is very low. Even in zone 3 with a green color, the sludge velocity was larger than 9.9E-5 ms^{-1}. Only in zones 2 and 1 where sludge velocity is lower than 9.9E-5 ms^{-1}, there is a possibility of sedimentation of particles larger than 0.85 mm, which comprise 17% of the total particles in the sludge (Baveli Bahmaei *et al.*, 2022). However, zones 1 and 2 cover a very small percentage of the digester volume, indicating good mixing conditions.

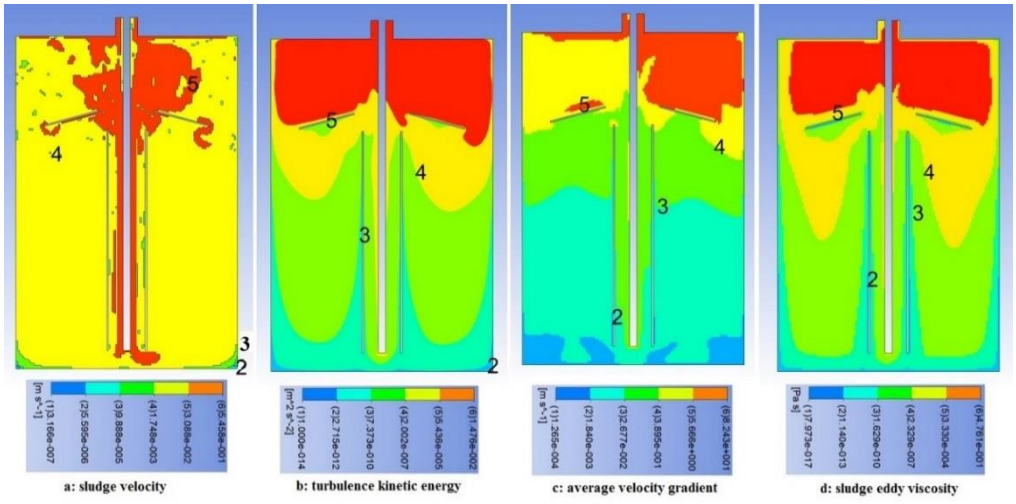

Fig.6. The resulting evaluation indexes in the digester; gas inlet velocity= 0.3 ms^{-1}

Gas-sparging intensity determines the amount of injected biogas for mixing and is an important operational assessment parameter. Based on the compressor's capacity, the injected biogas flow rate for the inlet-gas velocity of 0.3 ms^{-1} was calculated to be 0.085 m^3h^{-1} in the studied digester. In the actual experiment, 0.085 m^3h^{-1} yielded a *MEL* of 3.3 Wm^{-3}, which was close to 2.2 Wm^{-3} that was reported in another full-scale gas-mixed digester (Dapelo & Bridgeman, 2018). However, this value is still much lower than the recommended range (5-8 Wm^{-3}) needed for proper mixing (U. EPA, 1979). To match the recommended range, the inlet-gas velocity should be increased to over 0.7 ms^{-1}. This alteration requires additional investment in the studied digester, and the technical adjustments and the much higher energy consumption may challenge the biogas production process altogether. Therefore, increasing the inlet-gas velocity is not an efficient strategy for enhancing the flow and mixing, and the recommended *MEL* criterion appears unsuitable for the studied digester.

Particle image velocimetry results

To verify the results of CFD simulations, a digester was constructed with transparent material so that photos of its inside could be easily taken. The transparent pilot-scale digester was built with the optimal characteristics obtained from the CFD simulation results and is shown in Fig. 7. It is made of Polymethyl methacrylate with a thickness of 1.5 mm.

Fig.7. The transparent digester: (a) empty and (b) filled with municipal wastewater sludge

After selecting the inlet-gas velocity of 0.3 ms^{-1} as the most appropriate inlet-gas velocity, the particle image velocimetry (PIV) was performed. Due to the very dark color of the sludge (see Fig. 7b) and the indistinct particles in the images, a narrow strip of glitter was used along the height of the digester for PIV. The calculated sludge velocity, average velocity gradient, and sludge streamlines are shown in Fig. 8. The average velocity gradient (Fig. 8a) varies from 1.8E-6 to 34.3E-6 s^{-1}, while sludge velocity (Fig .8b) varies from 0 to 1.1×10^{-3} ms^{-1}. The maximum value of average velocity gradient and sludge velocity occurred between 20 to 35 cm from the top of the digester, and the streamline distance is maximum in this zone. As shown in Fig. 8b, in most parts of the digester's wall, the sludge velocity is greater than the minimum sludge velocity achieved from the simulations, indicating that particle sedimentation does not occur. Observing the velocity contour obtained

from the PIV shows that the lowest velocity is at the junction of the wall and the bottom of the digester (Fig. 8b). Furthermore since there are no streamlines in this area, the streamlines (Fig. 8c) confirm the results of CFD simulations.

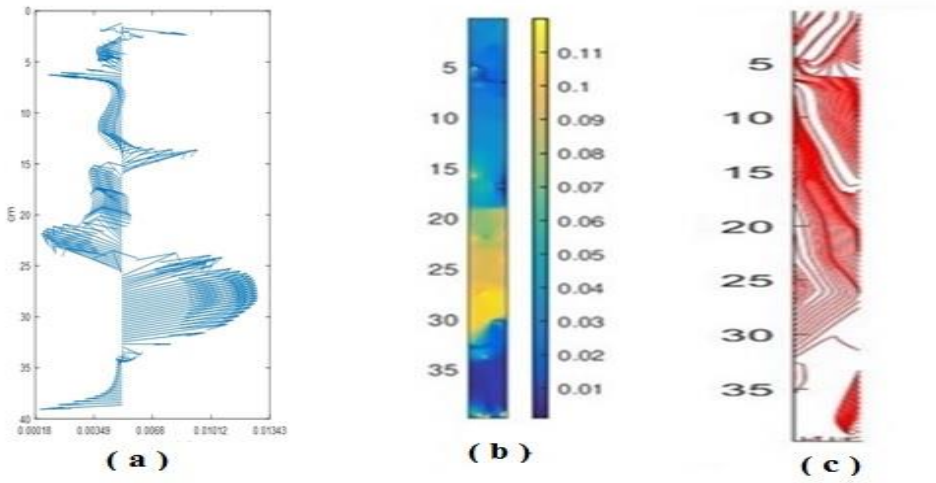

Fig.8. Results of particle image velocimetry (PIV) for inlet gas velocity of 0.3 ms^{-1}: (a) average velocity gradient (s^{-1}), (b) sludge velocity (cms^{-1}), and (c) streamline of particles in sludge

Conclusion

This study aimed to optimize mixing in gas-lift anaerobic municipal sewage sludge digesters. The model was built, simulated, and optimized, and the results were subsequently confirmed by building and testing the actual digester.

To optimize mixing in the digester, different inlet-gas velocities were investigated, and sludge particle velocity, the gradient of sludge particle velocity, the turbulence kinetic energy, and the eddy viscosity of the sludge particles were evaluated. The contours of these evaluation indexes were analyzed to determine the appropriate velocity for optimal mixing, which was found to be 0.3 ms^{-1}.

Based on the simulation results and particle sedimentation velocity in the sludge, it was expected that the sedimentation of the particles would not occur in the digester at the selected inlet-gas velocity; except for large sludge particles in the small triangular section near the junction of the wall and the bottom of the digester. Subsequently, a transparent anaerobic digester was constructed and loaded with municipal sewage sludge, operating at the optimal inlet-gas velocity of 0.3 ms^{-1}. Particle Image Velocimetry (PIV) was employed to calculate sludge velocity, average sludge gradient, and streamlines and to validate simulation outcomes. According to the results of the Particle Image Velocimetry (PIV), in most parts of the digestion wall length, the sludge velocity is greater than the minimum sludge velocity achieved in the simulations. Moreover, the velocity contour obtained from the PIV shows that the lowest velocity is at the junction of the wall to the bottom of the digester and streamlines also showed that there are no streamlines in this area. Overall, the PIV method successfully validated the CFD simulation and showed sufficient agreement between the simulation and the experiment. The results showed that the model used for simulating, optimizing, and verifying the simulation process was successful and can be recommended for similar gas-lift anaerobic digesters, which consist of a cylindrical tank with a flat bottom and a height-to-diameter ratio of 1.5. The draft tube diameter should be 0.2 times the digester diameter and the draft tube height should be 0.75 times the fluid height. The conical hanging baffle's distance from the fluid level should be equal to 0.125 times the fluid height, and its outer diameter should be 2/3 of the digester's diameter.

References

1. ANSYS-Fluent Inc. (2008). Fluent 12.0. ANSYS-Fluent Inc, Lebanon, N.H.
2. Baveli Bahmaei, D., Ajabshirchi, Y., Abdollah poor, Sh., & Abdanan Mehdizadeh, S. (2022). Step-by-step Simulation of Gas-lift Anaerobic Digester of Municipal Wastewater Sludge. *Iranian Journal of Biosystem Engineering*, *53*(1), 91-108. (In Persian). https://doi.org/10.22059/ijbse.2022.328388.665428
3. Celik, I. B., Ghia, U., Roache, P. J., Freitas, C. J., Coleman, H., & Raad, P. E. (2008). Procedure for estimation and reporting of uncertainty due to discretization in CFD applications. *Journal of Fluids Engineering*, *130*, 078001. https://doi.org/10.1115/1.2960953
4. Dapelo, D., Alberini, F., & Bridgeman, J. (2015). Euler-Lagrange CFD modeling of unconfined gas mixing in anaerobic digestion. *Water Researches*, *85*, 497-511. https://doi.org/10.1016/j.watres.2015.08.042
5. Dapelo, D., & Bridgeman, J. (2018). Euler-Lagrange Computational Fluid Dynamics simulation of a full-scale unconfined anaerobic digester for wastewater sludge treatment. *Advances in Engineering Software*, *117*, 153-169. https://doi.org/10.1016/j.advengsoft.2017.08.009
6. Dawkins, M. S., Cain, R., & Roberts, S. J. (2012). Optical flow, flock behavior and chicken welfare. *Animal Behavior*, *84*(1), 219-223. https://doi.org/10.1016/j.anbehav.2012.04.036
7. Hu, Y., Zhang, Sh., Wang, X., Peng, X., Hu, F., Wang, Ch., Wu, J., Poncin, S., & Li, H. Z. (2021). Visualization of mass transfer in mixing processes in high solid anaerobic digestion using Laser Induced Fluorescence (LIF) technique. *Waste Management*, *127*, 121-129. https://doi.org/10.1016/j.wasman.2021.04.038
8. Karim, Kh., Varma, R., Vesvikar, M., & Al-Dahhan, M. H. (2004). Flow pattern visualization of a simulated digester. *Water Research*, *38*(17), 3659-3670. https://doi.org/10.1016/j.watres.2004.06.009
9. Karim, Kh., Klasson, K. T., Hoffmann, R., Drescher, S. R., DePaoli, D. W., & Al-Dahhan, M. H. (2005). Anaerobic digestion of animal waste: Effect of mixing. *Bioresource Technology*, *96*(14), 1607-1612. https://doi.org/10.1016/j.biortech.2004.12.021
10. Karim, K., Thoma, G. J., & Al-Dahhan, M. H. (2007). Gas-lift digester configuration effects on mixing effectiveness. *Water Researches*, *41*(14), 3051-3060. https://doi.org/10.1016/j.watres.2007.03.042
11. McFarland, M. J. (2001). *Biosolids Engineering*. McGraw-Hill Education, New York.
12. Menter, F. R. (1993). *Zonal Two Equation k-cl, Turbulence Models for Aerodynamic Flows*. 24th Fluid Dynamics Conference. Orlando, Florida.
13. Meynell, P. J. (1976). *Methane: Planning a Digester*. London: Prism Press: 55-57.
14. Raffel, M., Willert, C. E., & Kompenhans, J. (1998). *Paeticle Image Velocimetry, A Practical Guide*. Springer Verlage, first edition.
15. Sawyer, C. N., & Grumbling, A. M. (1960). Fundamental consideration in high-rate digestion. Inc. Sewage Engineering Division. ASCE, 86-92.
16. Stukenberg, J. R., Clark, J. H., Sandino, J., & Naydo, W. R. (1992). Egg-shaped digesters: from Germany to the U.S. *Water Environment Technology*, *4*, 42-51.
17. U. EPA. (1979). Process design manual for sludge treatment and disposal, Center for environmental research in formation technology transfer. pp.
18. Varma, R., & Al-Dahhan, M. H. (2007). Effect of sparger design on hydrodynamics of a gas recirculation anaerobic bioreactor. *Biotechnology Bioengineering*, *98*(6), 1146-1160. https://doi.org/10.1002/bit.21500
19. Vesvikar, M. S., & Al-Dahhan, M. (2016). Hydrodynamics investigation of laboratory-scale Internal Gas-lift loop anaerobic digester using non-invasive CAPRT technique. *Biomass and*

Bioenergy, *84*, 98-106. https://doi.org/10.1016/j.biombioe.2015.11.014
20. Wei, P., Uijttewaal, W., Spanjers, H., Lier, J. B., & Kreuk, M. (2023). Optimising flow and mixing in a full-scale gas-mixed anaerobic digester by integrating sludge rheological data using computational fluid dynamics. *Chemical Engineering Journal*, 468. https://doi.org/10.1016/j.cej.2023.143647
21. Wu, B. (2010). CFD simulation of gas and non-Newtonian fluid two-phase flow in anaerobic digesters. *Water Research, 44*(13), 3861-3874. https://doi.org/10.1016/j.watres.2010.04.043
22. Wu, B. (2014). CFD simulation of gas mixing in anaerobic digesters. *Computers and Electronics in Agriculture, 109*, 278-286. https://doi.org/10.1016/j.compag.2014.10.007
23. Yang, J., Yang, Y., Ji, X., Chen, Y., Guo, J., & Fang, F. (2015). Three-Dimensional Modeling of Hydrodynamics and Biokinetics in EGSB Reactor. *Journal of Chemistry*. https://doi.org/10.1155/2015/635281

نشریه ماشین‌های کشاورزی
https://jame.um.ac.ir

مقاله پژوهشی

جلد ۱٤، شماره ۱، بهار ۱٤۰۳، ص ٤۷-۳۵

بهینه‌سازی همزنی در هاضم بی هوازی گاز- بالابر لجن فاضلاب شهری

داود باولی بهمئی[۱]، یحیی عجب شیرچی[۲]، شمس اله عبداله پور[۳*]، سامان آبدانان مهدی زاده[٤]

تاریخ دریافت: ۱۴۰۲/۰۵/۰۶
تاریخ پذیرش: ۱۴۰۲/۰۷/۱۰

چکیده

این تحقیق با هدف بهینه‌سازی همزنی در هاضم‌های بی‌هوازی گاز-بالابر لجن فاضلاب شهری انجام شد، زیرا همزنی یکنواخت برای ارتباط مؤثر بین باکتری‌های متانوژن و مواد مغذی مهم است. نمونه‌برداری لجن فاضلاب شهری در تصفیه‌خانه غرب اهواز (چنیبه) در تابستان ۱۴۰۱ انجام شد. یک مدل برای شبیه‌سازی، بهینه‌سازی و تایید فرآیند شبیه‌سازی با استفاده از دینامیک سیالات محاسباتی (CFD) توسط نرم‌افزار ANSYS Fluent 19.0 ارائه شد. سرعت گاز ورودی به هاضم تعیین شد و یک لوله گاز- بالابر و بافل آویزان مخروطی به طرح هاضم اضافه شد. سرعت‌های مختلف گاز ورودی برای بهینه‌سازی اختلاط در هاضم مورد بررسی قرار گرفت و شاخص‌های ارزیابی مانند سرعت ذرات لجن، گرادیان سرعت ذرات لجن، انرژی جنبشی تلاطم و ویسکوزیته گردابی ذرات لجن مورد ارزیابی قرار گرفت. سرعت بهینه گاز ورودی ۰/۳ ms^{-1} تعیین شد. نتایج شبیه‌سازی با استفاده از روش سرعت‌سنجی تصویری ذرات (PIV) تأیید شد و درصد همبستگی کافی بین کانتورهای CFD و PIV وجود داشت (۹۸/۸٪ در محل اتصال دیواره به کف هاضم). نتایج نشان داد که مدل مورداستفاده برای شبیه‌سازی، بهینه‌سازی و تأیید فرآیند شبیه‌سازی موفق بوده است و می‌توان آن را برای هاضم‌های بی‌هوازی گاز- بالابر استوانه‌ای شکل با نسبت ارتفاع به قطر ۱/۵، نسبت قطر لوله گاز- بالابر به قطر هاضم ۰/۲، نسبت ارتفاع لوله گاز- بالابر به ارتفاع سیال ۰/۷۵، فاصله بافل آویزان مخروطی از سطح سیال ۰/۱۲۵ برابر ارتفاع سیال و قطر بیرونی بافل به قطر هاضم ۲/۳ توصیه کرد.

واژه‌های کلیدی: دینامیک سیالات محاسباتی (CFD)، سرعت‌سنجی تصویر ذرات (PIV)، شبیه‌سازی، هضم

۱- دانشجوی دکتری، گروه مهندسی بیوسیستم، دانشکده کشاورزی، دانشگاه تبریز، تبریز، ایران
۲- استاد، گروه مهندسی بیوسیستم، دانشکده کشاورزی، دانشگاه تبریز، تبریز، ایران
۳- دانشیار، گروه مهندسی بیوسیستم، دانشکده کشاورزی، دانشگاه تبریز، تبریز، ایران
۴- دانشیار، گروه مهندسی مکانیک بیوسیستم، دانشکده مهندسی زراعی و عمران روستائی، دانشگاه علوم کشاورزی و منابع طبیعی خوزستان، اهواز، ایران
(*- نویسنده مسئول: Email: shams@tabrizu.ac.ir)

https://doi.org/10.22067/jam.2023.83626.1182

Journal of Agricultural Machinery

Homepage: https://jame.um.ac.ir

Research Article
Vol. 14, No. 1, Spring 2024, p. 49-67

A Finite Element Model of Soil-Stress Probe Interaction under a Moving Rigid Wheel

M. Naderi-Boldaji[1*], H. Azimi-Nejadian[2], M. Bahrami[1]

1- Department of Mechanical Engineering of Biosystems, Faculty of Agriculture, Shahrekord University, Shahrekord, Iran
2- Department of Mechanical Engineering of Biosystems, Faculty of Agriculture, Jahrom University, Jahrom, Iran
(*- Corresponding Authors Email: naderi.mojtaba@sku.ac.ir)

Received: 29 August 2023
Revised: 07 October 2023
Accepted: 09 October 2023
Available Online: 09 October 2023

How to cite this article:
Naderi-Boldaji, M., Azimi-Nejadian, H., & Bahrami, M. (2024). A Finite Element Model of Soil-Stress Probe Interaction under a Moving Rigid Wheel. *Journal of Agricultural Machinery, 14*(1), 49-67. https://doi.org/10.22067/jam.2023.84158.1185

Abstract

Machinery traffic is associated with the application of stress onto the soil surface and is the main reason for agricultural soil compaction. Currently, probes are used for studying the stress propagation in soil and measuring soil stress. However, because of the physical presence of a probe, the measured stress may differ from the actual stress, i.e. the stress induced in the soil under machinery traffic in the absence of a probe. Hence, we need to model the soil-stress probe interaction to study the difference in stress caused by the probe under varying loading geometries, loading time, depth, and soil properties to find correction factors for probe-measured stress. This study aims to simulate the soil-stress probe interaction under a moving rigid wheel using finite element method (FEM) to investigate the agreement between the simulated with-probe stress and the experimental measurements and to compare the resulting ratio of with/without probe stress with previous studies. The soil was modeled as an elastic-perfectly plastic material whose properties were calibrated with the simulation of cone penetration and wheel sinkage into the soil. The results showed an average 28% overestimation of FEM-simulated probe stress as compared to the experimental stress measured under the wheel loadings of 600 and 1,200 N. The average simulated ratio of with/without probe stress was found to be 1.22 for the two tests which is significantly smaller than that of plate sinkage loading (1.9). The simulation of wheel speed on soil stress showed a minor increase in stress. The stress over-estimation ratio (i.e. the ratio of with/without probe stress) noticeably increased with depth but increased slightly with speed for depths below 0.2 m.

Keywords: FEM simulation, Machinery traffic, Soil bin, Soil stress, Stress probe

Introduction

With the increase in the world's population, the need for food production has increased, which has led to more intense exploitation of the soil for more production. This was accompanied by an increase in the size and weight of farming machines to increase production capacity (Keller, Lamandé, Naderi-Boldaji, & de Lima, 2022). The increased weight of the machinery intensified soil degradation due to soil compaction. Soil compaction reduces the soil porosity, aeration, and water retention capacity and increases resistance to root penetration, surface runoff, soil erosion, and the energy required for tillage causing a series of effects that negatively affect crop yield and increase production costs (Hamza & Andersson, 2005; Nawaz, Bourrie, & Trolard, 2013; Shahgholi, Ghafouri Chiyaneh, & Mesri Gundoshmian, 2018).

It might be possible to prevent traffic-induced soil compaction by ensuring that the stress applied to the soil never exceeds the soil strength (Koolen & Kuipers, 1983). Conventionally, analytical methods based on

https://doi.org/10.22067/jam.2023.84158.1185

Boussinesq's theory of stress distribution (Boussinesq, 1885) have been used to predict soil stress propagation and the resulting compaction. Some of these models include SOCOMO (van den Akker, 2004), SoilFlex (Keller, Défossez, Weisskopf, Arvidsson, & Richard, 2007), Terranimo (Stettler *et al.*, 2014), and REPRO (Rücknagel *et al.*, 2015) all of which consider the soil as a continuum, elastic, homogeneous, and isotropic material. More accurate stress propagation models have been developed by including a stress concentration factor that varies with soil strength conditions (Frohlich, 1934; Söhne, 1953). Additionally, we need to measure the soil stress and validate the stress estimation calculated with the analytical models. Stress probes come in many shapes and forms. For example, fluid-inclusion probes i.e. Bolling probes (Bolling, 1985) or strain-gauged load cell transducers (Schjønning, Lamandé, Tøgersen, Arvidsson, & Keller, 2008; de Lima & Keller, 2021; Bahrami, Naderi-Boldaji, Ghanbarian, & Keller, 2023) cause the measured stress to deviate from the actual stress which occurs in the absence of the probe, while the actual stress causes soil compaction. The reasons for stress deviation can be the disturbance of the soil structure during the probe installation, the quality of the contact between the probe and the soil, the concentration of stress on the probe due to the arching effect, and the difference between the probe's stiffness and the stiffness of its surrounding soil (Kirby, 1999a, and 1999b). Therefore, the stress probe may under- or over-estimate the true soil stress. This difference is affected by the probe geometry, loading geometry, loading time, and mechanical properties of the soil (Weiler & Kulhawy, 1982). It is possible to correct the probe-measured stress to the soil's true stress by modeling the stress fields around the probe and finding a relationship for estimating the stress deviation due to embedding the probe into the soil.

Apart from analytical approaches, numerical simulation tools are widely applied for analyzing the stress propagation and soil compaction caused by machinery traffic. The main numerical methods used for simulation of stress propagation in soil can be categorized into finite element method (FEM), discrete elements method (DEM), and smoothed particle hydrodynamics (SPH). In FEM, considering the soil as a continuum medium using the theories of continuum mechanics, stress propagation is analyzed by calculating the stress on each element in contact with its adjacent element. In DEM, the stress transmission is analyzed by calculating the contact forces between the particles using Newton's second law, and the stress is transmitted through a chain of particles in contact with each other. In SPH, the particles are modeled in a fluid bed, and solving does not require meshing like the computational fluid dynamics method.

Several studies have used FEM to simulate stress propagation in the soil or the soil-tire interaction (e.g. Peth, Horn, Fazekas, & Richards, 2006; Cueto, Coronel, Bravo, Morfa, & Suárez, 2016; Keller, Ruiz, Stettler, & Berli, 2016; Silva *et al.*, 2018; Farhadi, Golmohammadi, Sharifi Malvajerdi, & Shahgholi, 2020; Jimenez *et al.*, 2021). Furthermore, the simulation of stress propagation in soil using DEM has been considered in multiple recent research studies (e.g. De Pue & Cornelis, 2019; De Pue, Lamandé, & Cornelis, 2020; Acquash & Chen, 2021; Bahrami, Naderi-Boldaji, Ghanbarian, & Keller, 2022; Bahrami *et al.*, 2023). However, we only found one recent study of modeling soil stress under tire traffic that used SPH (Gheshlaghi & Mardani, 2021). In most of the studies reported so far, either the propagation of soil true stress or the resulting soil compaction have been considered. However, the interaction between the soil and the stress probe and the difference between true and probe-measured stresses was studied less commonly. A recent study by de Lima and Keller (2021) investigated the probe stress deviation as affected by probe geometry (in terms of the ratio of diameter to height), difference in soil and probe material stiffness, and interference of multi-probe setups under

static loading using FEM. However, soil-probe interaction under dynamic loading (like a passing wheel) is an aspect that has been studied less frequently.

In a study conducted at Shahrekord University, Iran (Bahrami *et al.*, 2020, 2022, and 2023), Bahrami *et al.* (2022), the results of FEM and DEM for simulation of stress propagation under circular surface loading using plate sinkage test were compared. Stress was measured using a cylindrical load cell probe at 0.15 m depth in clay loam soil with 11% water content. The results showed that FEM may overestimate the probe-induced stress deviation due to the continuum nature of the soil in contact with the stress probe. The stress overestimation ratio (i.e. the ratio of with/without probe stress) was much larger in FEM than in DEM simulations. Consequently, Bahrami *et al.* (2023) investigated the interaction between soil and the stress probe under a moving rigid wheel in a soil bin for simulating the stress propagation in soil using DEM. The results showed that by modeling the soil with 10 mm diameter particles, the simulated stress with the probe was about 12% higher than the simulated true stress which was in close agreement with the results obtained from plate sinkage loading. The simulation of stress with varying wheel speed showed almost no significant effect. However, the results are still insufficient to acknowledge DEM as the best simulation approach for stress propagation for soils in different conditions. A freshly tilled or aggregated soil may be better simulated using DEM while a wet and compact soil may resemble more of a continuum nature which is better modeled using FEM. Whether using DEM or FEM, it is important to understand how the probe-induced stress deviation may vary under loading geometry, static *vs.* dynamic loading, depth, and loading time (speed).

The present study aims to simulate the stress propagation under the rigid wheel tested in a soil bin and the interaction between the soil and a stress probe using FEM to see how the stress overestimation ratio under wheel loading may differ from that of under plate sinkage loading, both simulated using FEM. It was hypothesized that the stress overestimation ratio obtained using FEM is not influenced by loading geometry, depth, and loading time (speed). Therefore, the objectives of this study are to (i) develop a FEM model of soil-probe interaction to study the stress propagation in soil under a rigid wheel and compare the simulated and measured stress, (ii) simulate the effect of wheel speed on soil stress and wheel sinkage, and (iii) evaluate the stress overestimation ratio under the moving wheel with various depths, wheel speeds, and probe geometries. The experimental data of two-wheeling tests conducted in a soil bin by Bahrami *et al.* (2023) were used for comparison with the FEM model predictions.

Materials and Methods

FEM model of soil-stress probe interaction under a moving rigid wheel

The FEM model of soil-wheel-stress probe interaction was developed in ABAQUS/CAE (Dassault Systemes Simulia Corp., Providence, RI, USA). According to the geometry and the symmetry of the model, a half-model with a plane of symmetry was generated. In this model, the soil was defined as a deformable material, and the wheel and the stress probe were modeled as rigid bodies. A wheel with a diameter of 0.27 m and a width of 0.15 m was modeled similar to the wheel used for the experimental tests in the soil bin. The stress probe was modeled in the form of a cylindrical probe consisting of two parts; the force-sensing surface (sensor) with 0.05 m diameter and the housing that is 0.07 m in diameter and 0.03 m in height (Bahrami *et al.*, 2022, and 2023). This allowed to evaluate the effect of the ratio of housing to sensor diameter on the stress overestimation ratio under loading of the moving wheel. To assemble the probe into the soil at a given depth and define the contact surfaces, a similar cylinder was cut from the soil where the probe is placed. Then, the probe is placed in the soil with an axisymmetric movement constraint.

The soil box was generated with dimensions of 2 × 1 × 1 m (length × width ×

depth). The model parts were assembled so that the wheel was placed on the soil surface and the stress probe into the soil at 0.15 m depth (Fig. 1a). The model's output is the force applied to the sensor surface during the movement of the wheel. Probe stress was calculated by dividing the force by the area of the probe sensing surface. The dependency of the FEM solution on mesh density was evaluated to select the appropriate size of the soil elements. For this purpose, six models were created with element sizes of 30, 25, 20, 15, 10, and 5 mm. In all simulations, the wheel speed was set at 1 m s^{-1} with 1,200 N vertical loading on the wheel axle. The true stress (i.e. the element vertical stress) at 0.15 soil depth was plotted against the element size for an elastic soil with 2 MPa elastic modulus and 0.3 Poisson's ratio. The stress increased sharply with elements larger than 10 mm (not shown). The stress difference in the simulations with 5 and 10 mm elements was less than 1%. Therefore, the element size of 10 mm was selected for the following simulations (Fig. 1b). The wheel-soil and stress probe-soil contacts were defined by the surface-to-surface contact method, and the value of the friction coefficient between the surfaces was assumed to be 0.5 (Ucgul, Saunders, & Fielke, 2017). The boundary conditions for the soil box and wheel were defined. The wheel was constrained to rotate and move the distance along the soil bin's length at varying speeds i.e. varying the traveling time. The wheel was free to move in the vertical direction and to sink into the soil. The wheel was free-rolling with no input torque. With-probe and without-probe stresses were analyzed under the moving wheel for each simulation. To measure the without-probe stress, the vertical stress of the soil element at a given depth was obtained from the model. For every simulation, the with-probe stress was higher than the without-probe stress which is due to the stress concentration around the probe owing to the arching effect. The arching effect occurs on the contact surface between two objects due to the difference between the yield strengths of the materials (Labuz & Theroux, 2005). The ratio of with-probe to without-probe stress was calculated as the stress overestimation ratio.

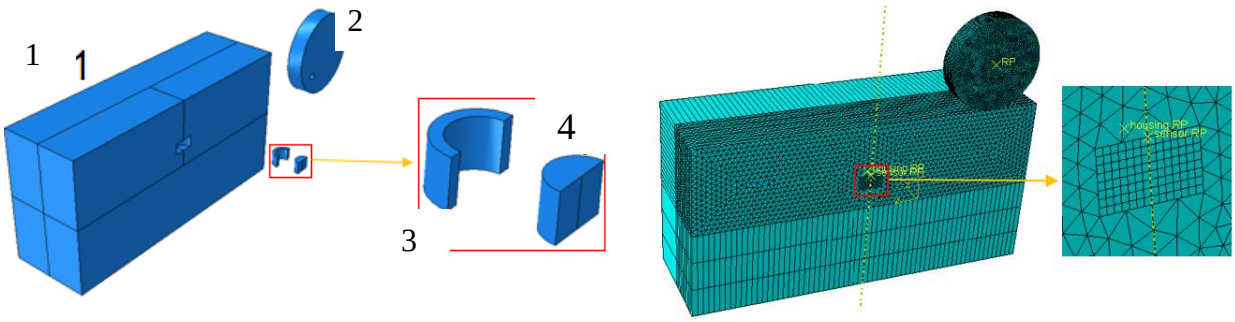

(a) (b)

Fig.1. (a) FEM model parts, 1- Soil box, 2- Rigid wheel, 3- Stress probe housing, 4- Probe sensing surface, and (b) Finite element mesh of the assembled model

In this study, soil was defined either as a pure-elastic or as an elastic-perfectly plastic material with a linear Drucker-Prager yield criterion. Drucker-Prager yield criterion has been used in many studies in the field of soil-machine interaction (Xia, 2011; Azimi-Nejadian, Karparvarfard, Naderi-Boldaji, & Rahmanian-Koushkaki, 2019; Arefi, Karparvarfard, Azimi-Nejadian, & Naderi-Boldaji, 2022; Mahboub & Mardani 2022; Naderi-Boldaji, Karparvarfard, & Azimi-Nejadian, 2023). It is necessary to define the modulus of elasticity and Poisson's ratio for elastic properties, and Drucker-Prager's internal angle of friction (β) and compressive yield stress for plastic properties. Drager-Prager friction angle can be calculated using the Mohr-Coulomb friction angle (φ) obtained

from the direct shear test (ABAQUS, 2019) defined in Eq. 1.

$$\beta = \frac{6 \sin \varphi}{3 - \sin \varphi} \quad (1)$$

The compressive yield stress (σ_c) is theoretically related to soil cohesion (c) and is given in Eq. 2.

$$\sigma_c = 2c \frac{cos\ \varphi}{1 - sin\ \varphi} \quad (2)$$

The compressive yield stress is an important parameter in determining the soil strength and analyzing the soil compressibility behavior (Khalid, Farooq, & Mujtaba, 2018). Considering the soil's elastic-perfectly plastic behavior allows us to define a distinct border between elastic and plastic deformations by defining the compressive yield stress.

Stress propagation as affected by soil elastic-plastic properties

A series of simulations were performed to evaluate the soil's true stress with changes in soil elastic-plastic properties (i.e. the model input parameters). This helps to identify the most important soil parameters affecting the stress propagation and can be used for calibrating more accurately. For this purpose, each of the model's input parameters was examined in the range shown in Table 1. Simulations were carried out for both pure-elastic soil (with varying modulus of elasticity and Poisson's ratio) and elastic-plastic soil (with varying elastic and plastic parameters). The simulations were performed with a wheel loading of 1,200 N which, as explained later, is the condition of the experimental test II.

Table 1- The range of parameters tested in sensitivity analyses.

Soil behavior	Parameter	Tested range	References
Elastic	Young's modulus of elasticity (kPa)	10,000-200,000	Naderi-Boldaji *et al.* (2013); Azimi-Nejadian *et al.* (2019)
Elastic, Elastic-plastic	Poisson's ratio	0.1-0.4	
Elastic-plastic	Compressive yield stress (kPa)	20-200	
Elastic-plastic	Young's modulus of elasticity (kPa)	1,000-10,000	
Elastic-plastic	Coefficient of soil wheel friction	0.1-0.5	
Elastic-plastic	Internal angle of friction (°)	10-50	

Experimental data of vertical stress under the moving wheel

The experimental stress data measured under a Teflon wheel for two soil conditions in a soil bin by Bahrami *et al.* (2023) were used as a reference for validating the modeling results. Fig. 2 shows a schematic of the soil bin equipped with a single testing wheel and its components. The soil bin is a 6 m long, 1 m wide, and 1 m deep soil box filled with clay loam soil (36% sand, 30% silt, and 34% clay). There is a double-sided blade on the carrier for soil movement and preparation. The testing wheel is positioned at the front of the carrier with a mechanism that allows varying the vertical loading on the wheel axle using standard weights. Further information concerning the soil bin can be found in Bahrami *et al.* (2023). Two wheeling tests were carried out in the soil bin at 11% water content at two soil compaction levels. The soil compaction levels were prepared by rolling the soil layers while preparing the soil until bulk densities of 1,200 and 1,350 kg m^{-3} were achieved for tests I and II, respectively. Test I and test II were carried out with 600 and 1,200 N wheel loading, respectively. The wheel speed for the two tests was 0.2 m s^{-1}. Soil stress was measured with a cylindrical load cell probe at 0.15 m soil depth. For each test, the soil cone index was measured in three replicates to a depth of 0.2 m before the wheeling test. Additionally, the wheel sinkage was measured with an image processing technique (Bahrami *et al.*, 2023).

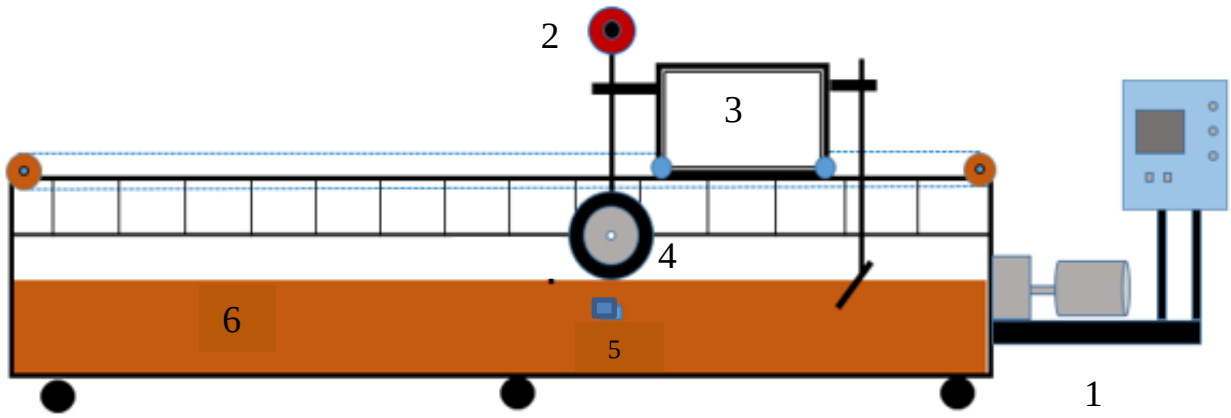

Fig.2. The schematics of the soil bin and wheel tester: 1- Drive system, 2- Weights applied to the wheel, 3- Carrier, 4- Testing wheel, 5- Load cell probe, and 6- Soil box (Bahrami *et al.*, 2023)

Calibration of the FEM input parameters

The elastic-plastic soil properties of the FEM model were calibrated using a similar approach as reported in Bahrami *et al.* (2023). Cone index and wheel sinkage into the soil were simulated and compared with the experimental results. The FEM model of cone penetration test developed by Naderi-Boldaji *et al.* (2023) was employed (Fig. 3). Naderi-Boldaji *et al.* (2023) showed the compressive yield strength and the angle of internal friction as the two parameters most affecting the soil's cone index. Hence, a simulation of the average cone index within 0-0.2 m depth was compared with the experimental cone index profile measured in the soil bin. Compressive yield strength was calibrated by matching the simulated and the experimental average cone indexes. Mohr-coulomb internal angle of friction was used by Bahrami *et al.* (2020) who measured the angle of friction for the same soil texture and water content using direct shear test. It was evaluated that the wheel sinkage into the soil is driven by the soil modulus of elasticity for a given vertical wheel loading. Matching the experimental and simulated wheel sinkage allowed the calibration of the soil's modulus of elasticity. We assumed a 0.3 value for Poisson's ratio as a routine assumption from previous studies (e.g. Ibrahmi, Bentaher, Hbaieb, Maalej, & Mouazen, 2015; Naderi-Boldaji, Hajian, Ghanbarian, & Bahrami, 2018). It was assumed that a minor difference between Poisson's ratio of the testing soil and the value assumed does not cause a significant error in prediction by the FEM model.

Table 2 gives the average values of elastic-plastic soil properties calibrated for the soil used for the two tests as well as the average experimental values for cone index and wheel sinkage. The average measured cone index values for tests I and II were 0.38 and 0.58 MPa, respectively, then the compressive yield stress values for these tests were calibrated as 75 and 90 kPa, respectively. The measured wheel sinkage for tests I and II were 30 and 15 mm, respectively. These values were obtained in the FEM simulation for the modulus of elasticity of 0.3 and 3 MPa, respectively. A decrease in the modulus of elasticity for each test increased the simulated wheel sinkage into the soil. For instance, by decreasing the modulus of elasticity from 1 to 0.1 MPa in test I, the wheel sinkage increased from 13.5 to 72.4 mm.

Finally, after calibrating the elastic-plastic parameters of the soil, stress simulation was performed for probe depths of 0.05, 0.1, 0.15, 0.2, 0.25, and 0.3 m with varying the wheel's speed in the range of 1-5 m s^{-1} to see how the soil stress and stress overestimation ratio are affected by probe depth and wheeling speed. Furthermore, the geometry of the stress probe was tested by varying the sensor diameter to

see the variations in stress overestimation ratio with the probe geometry.

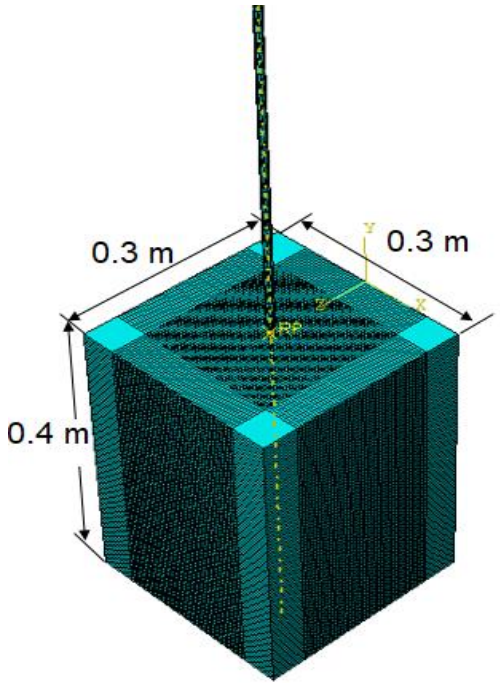

Fig.3. The FEM model of cone penetration test (Naderi-Boldaji *et al.*, 2023, Copyright 2023 by the International Society for Terrain-Vehicle Systems)

Table 2- The parameters measured in experimental tests and used for the FEM model calibration

Parameters	Test I	Test II
Measured soil density (kg m^{-3})	1,200	1,350
Measured coefficient of internal friction	0.24	0.24
Assumed Poisson's ratio	0.3	0.3
Wheel load (N)	600	1,200
Wheel speed (m s^{-1})	0.2	0.2
Measured wheel sinkage (mm)	30	15
Measured average cone index (MPa)	0.38	0.58
Calibrated Young's modulus (MPa)	0.3	3
Calibrated yield stress (kPa)	75	90

Results and Discussion

Stress propagation under the moving wheel

Figure 4a shows the simulation of the vertical stress propagation in soil under the moving wheel at a speed of 1 m s^{-1} with a wheel loading of 1,200 N. The stress bulb created under the wheel and the stress attenuation with depth can be seen. Stress transfer to the stress probe is observed when the wheel moves above the probe. A wheel rut was formed on the soil surface due to plastic deformation. The stress developed in the probe with the horizontal movement of the wheel is shown in Fig. 4b. A residual stress may be seen for elastic-plastic soils after the passing of the wheel which is attributed to the soil's plastic deformation. For pure-elastic soil, the soil's stress and deformation are expected to be fully recovered after the wheel passes.

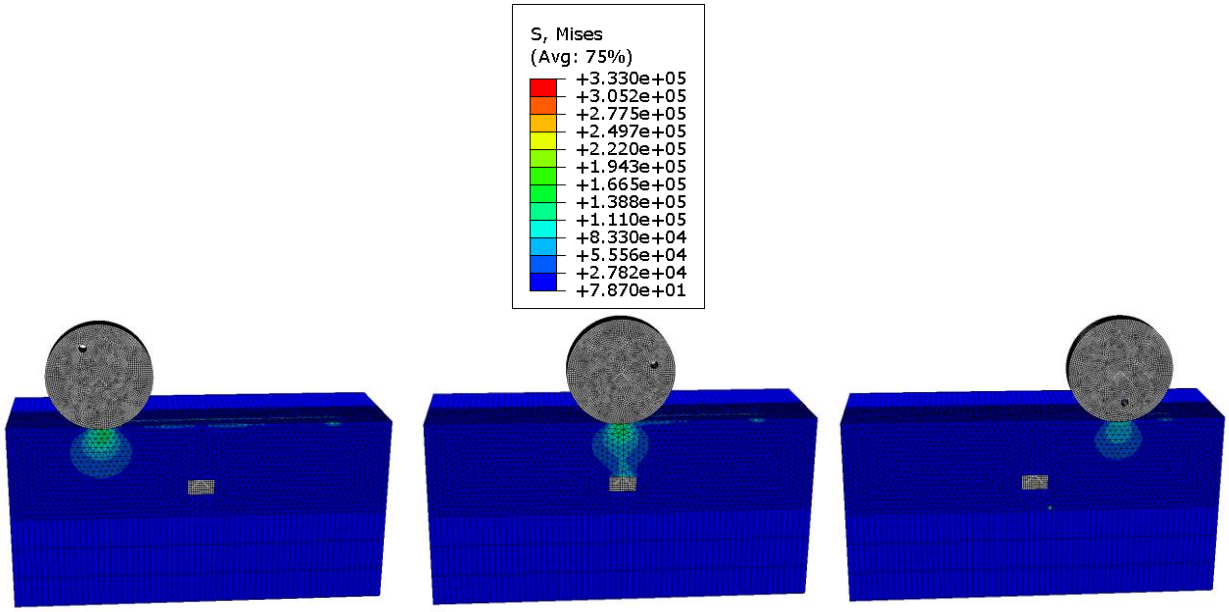

(a)

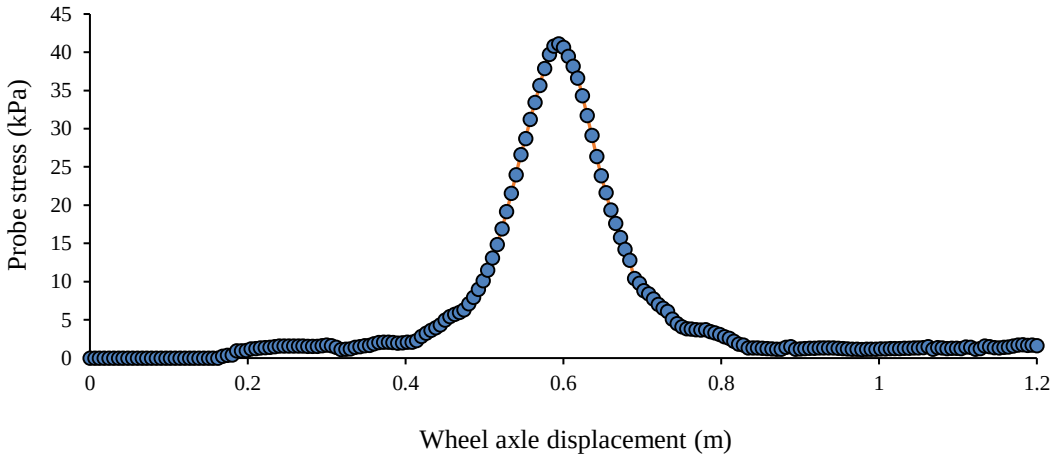

(b)

Fig.4. (a) Test II wheel movement simulation (the color bar legend indicates the Von Mises stress in soil), and (b) Variation in the simulated probe stress developed by wheel movement on the soil at a forward speed of 1 m s^{-1} and wheel loading of 1,200 N for Test II

Effect of soil elastic-plastic properties on soil stress

The results of analyses of the model parameters are first presented for pure-elastic soil (Fig. 5) and then for elastic-plastic soil (Fig. 6). As mentioned earlier, the true stress was analyzed for these analyses. For a pure-elastic soil, no effect of Young's modulus of elasticity and Poisson's ratio on soil stress was found under the wheel at a given loading (Fig. 5). This is in accordance with the analytical solution of vertical stress distribution using Boussinesq theory which is independent of soil properties.

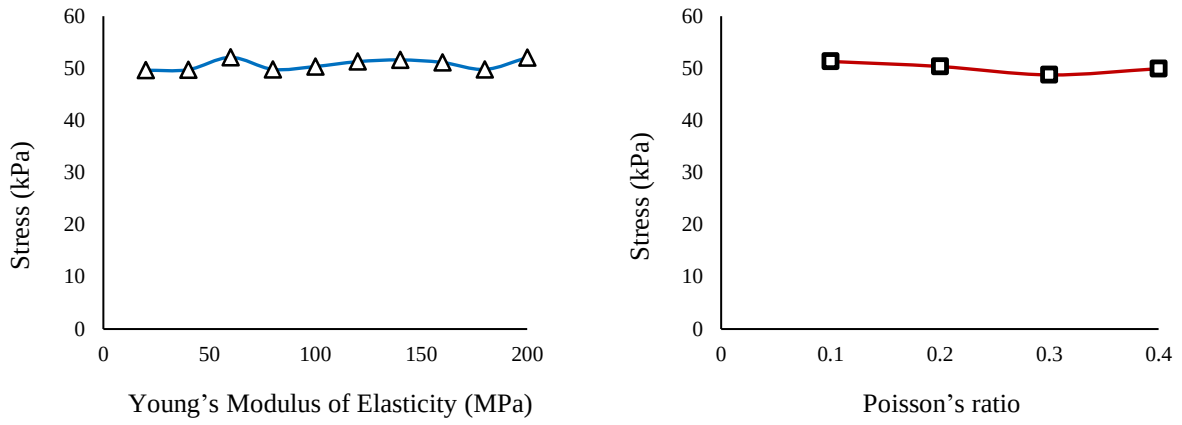

Fig.5. FEM-simulated peak true stress for a pure-elastic soil as functions of (a) Young's modulus of elasticity, and (b) Poisson's ratio at a wheel loading of 1,200 N

For the elastic-plastic soil, the stress in the soil noticeably changed with Young's modulus of elasticity (Fig. 6a) and the compressive yield stress (Fig. 6b). For ease of interpretation, the vertical axes of the plots shown in Fig. 6 are a normalized ratio of the stress simulated for the elastic-plastic soil to the corresponding stress for the pure-elastic soil, titled the stress concentration ratio. This ratio increased by increasing Young's modulus of elasticity to 6 MPa, and then decreased slightly with a further increase in the modulus of elasticity (Fig. 6a). This may be explained by the decrease in wheel sinkage into the soil and soil-wheel contact area which increases the ground normal stress at the soil-wheel interface.

With increasing the compressive yield stress, the stress concentration ratio approaches one, corresponding to a pure-elastic soil (Fig. 6b). The larger the stress concentration ratio, the higher the soil's plastic strain. At a given wheel loading, a higher plastic strain is obtained for smaller values of compressive yield stress. Soil with lower compressive strength could correspond to soil with a higher water content. For such soils, the stress concentration ratio is larger which confirms the interpretation of the stress concentration factor introduced by Frohlich (1934).

With increasing the soil-wheel coefficient of friction, the stress concentration ratio decreased slightly (Fig. 6c). This may be explained by the tangential frictional shear stresses created on the wheel-soil interface whose vertical stress components balance a portion of the wheel's load.

The stress concentration ratio decreased with increasing the internal angle of friction (Fig. 6d). With a particulate view of the soil media, larger friction between the particles attenuates the vertical stress with depth (Bahrami *et al.*, 2023). Although the Poisson's ratio had no effect on stress for pure-elastic soil, a slight increase in stress concentration ratio with increasing the Poisson's ratio was observed for elastic-plastic soil (Fig. 6e). This may be attributed to variations in the arching effect and the stress distribution on the probe's surface as affected by Poisson's ratio.

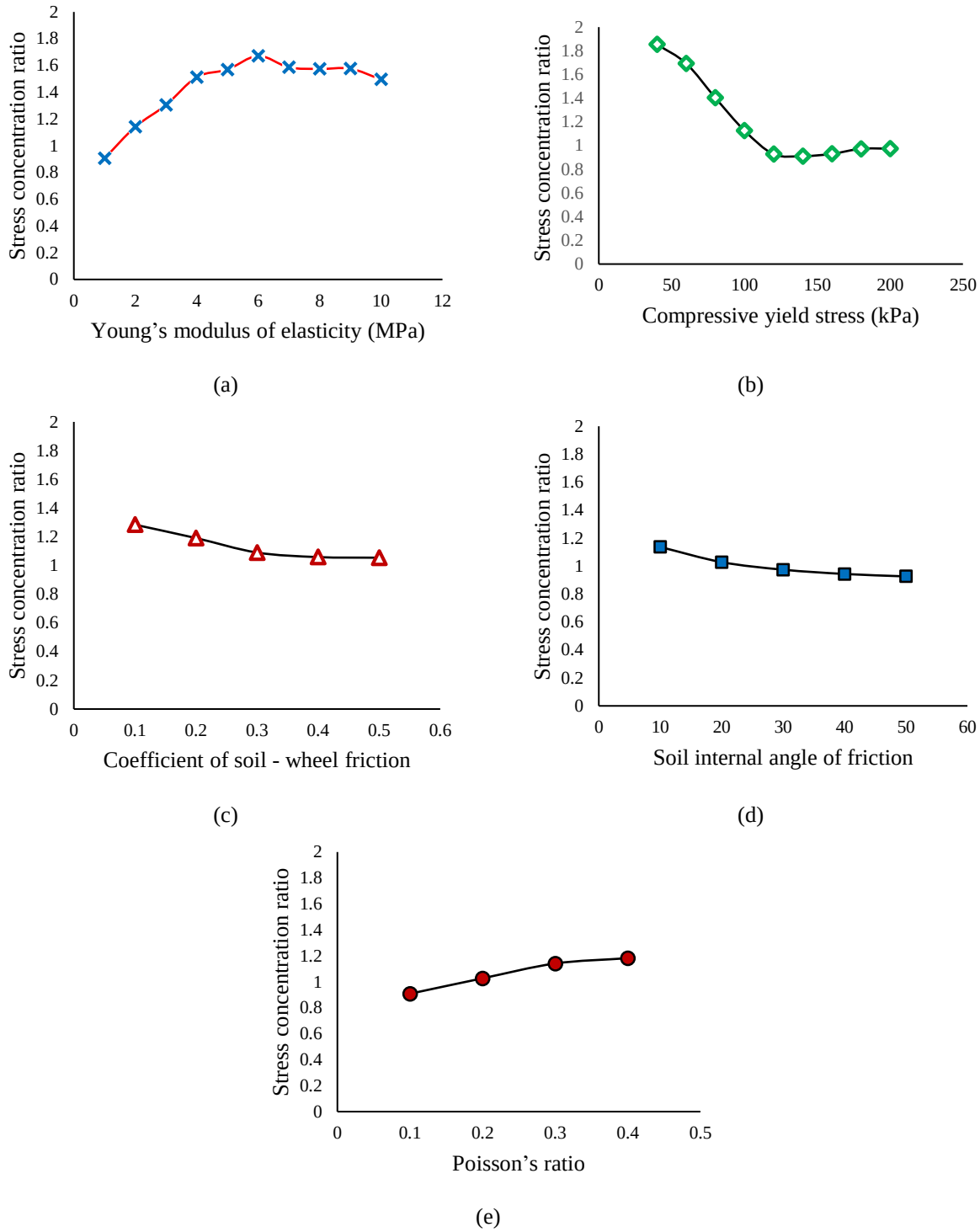

Fig.6. Stress concentration ratio, i.e. the ratio of simulated true stress of an elastic-plastic soil to the corresponding stress for a pure-elastic soil as functions of (a) Young's modulus of elasticity, (b) Compressive yield stress, (c) Coefficient of soil-wheel friction, (d) Soil internal angle of friction, and (e) Poisson's ratio.

Comparison of experimental and FEM-simulated stress

The FEM-simulated peak stress (with probe and without probe) as well as the

experimentally measured stress at the 0.15 m depth for test I (with bulk density of 1,200 kg m^{-3}) and test II (with bulk density of 1,350 kg m^{-3}) is shown in Fig. 7a and 7b, respectively. The peak stress measured under the wheel for test I and test II are 18 and 30 kPa, respectively. The larger value of stress for test II is due to the higher wheel loading. The FEM-simulated with-probe stress is larger than the experimental stress by 26.8% and 20.5% for tests I and II, respectively. The stress overestimation ratio (i.e. the ratio of simulated with-probe/without-probe stress) was found to be 1.27 and 1.17 for tests I and II, respectively. The difference in the stress overestimation ratio for test I and test II may be due to variations in the mechanical properties and plastic deformation of the soil (de Lima & Keller, 2021). The average overestimation ratio resulted here (1.22) is 0.1 larger than the DEM simulation results reported by Bahrami *et al.* (2023). However, the stress overestimation ratio is much smaller than the value obtained under FEM-simulated plate sinkage loading which was 1.9 (Bahrami *et al.*, 2022). This may be owing to the different boundary conditions or dynamic *vs.* static loading for the wheeling test and plate sinkage test, respectively.

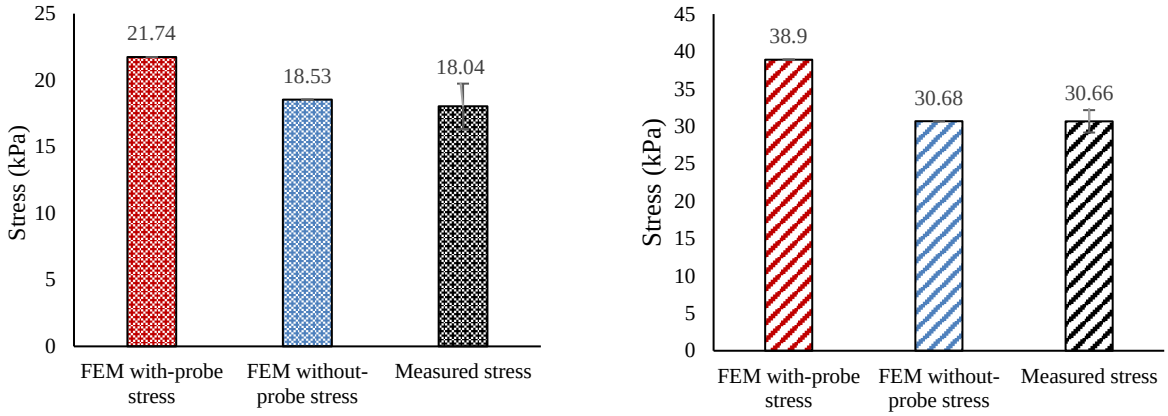

(a) (b)

Fig.7. Comparison of simulated and measured peak vertical stress for (a) test I (bulk density 12,00 kg m^{-3} and wheel loading of 600 N), and (b) test II (bulk density 1,350 kg m^{-3} and wheel loading of 1,200 N). The error bar in the measured stress column shows the standard error of replications (Bahrami *et al.*, 2023).

Stress overestimation ratio as affected by wheel speed and probe depth

Fig. 8 shows the simulated without-probe (Fig. 8a) and with-probe (Fig. 8b) stress as a function of wheel speed and depth for soil properties and wheel loading of test II. As expected, stress attenuates strongly with depth. Minor increases in without-probe stress can be seen with increasing wheel speed for any depth. However, with-probe stress slightly increases with wheel speed for depths higher than 0.15 m. For instance, at 0.3 m depth, increasing wheel speed from 1 to 5 m s^{-1} resulted in increased without-probe stress from 14.9 to 17.8 kPa and with-probe stress from 29.9 to 45.8 kPa which indicates a stronger effect of speed on with-probe stress. The slight increase in soil stress with the increased wheel speed can be explained by inertial effects. The stress overestimation ratio was plotted as a function of depth and wheel speed as shown in Fig. 9. It can be seen that, with the increasing speed of the wheel, the stress overestimation ratio at 0.3 m depth has increased to values larger than 2. The increase in stress overestimation ratio with increasing wheel speed is evident only at 0.25 and 0.3 m depths.

The results of previous literature on the

effect of traffic speed on soil stress are discrepant and almost contrasting. For instance, Naderi-Boldaji, Kazemzadeh, Hemmat, Rostami, and Keller (2018) reported that the average normal stress measured by the Bolling probe increased with tractor forward speed. On the other hand, some studies have shown a decrease in effective soil stress with increasing wheel speed (Horn, Blackwell, & White, 1989; Pytka, 2013). The variations in the experimental results may be due to the effect of pore water pressure at different soil water contents (Horn *et al.*, 1989). The effect of speed on soil stress and soil deformation is further discussed in the following section.

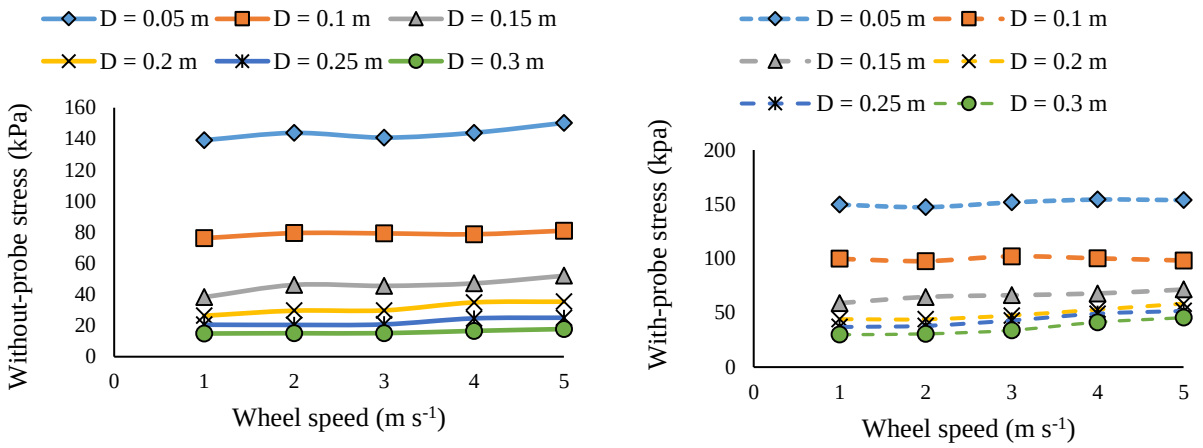

(a) (b)

Fig.8. (a) Without-probe and (b) with-probe vertical stress as functions of wheel speed and depth for soil properties and wheel loading of test II at different probe depths

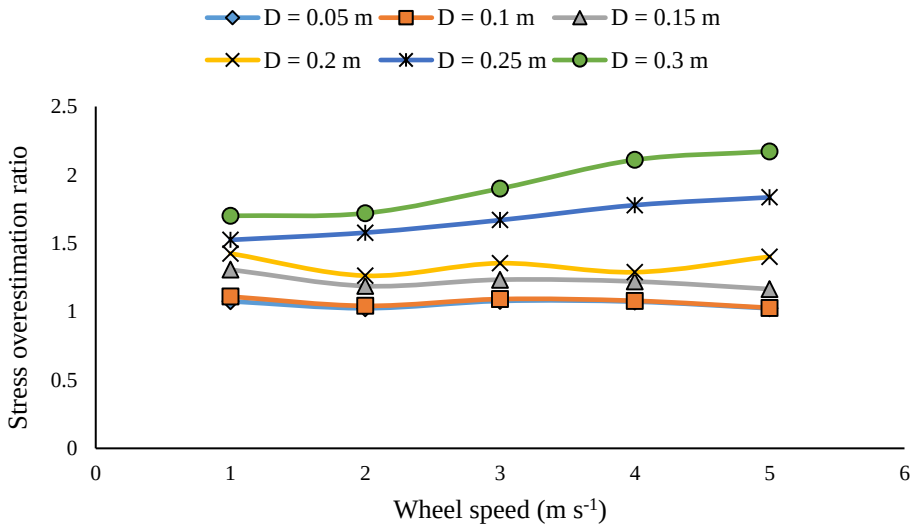

Fig.9. Stress overestimation ratio as a function of wheel speed at different probe depths

The effect of speed on wheel sinkage

Fig. 10 shows wheel sinkage as a function of wheel displacement and wheel speed for the soil properties and wheel loading of test II. Wheel sinkage increased rapidly once the wheel started moving and reached a constant value at the end of tests (Fig. 10a). The wheel speed had no significant effect on the wheel

sinkage, the average of which was calculated from wheel sinkage values of wheel displacement from 0.6 to 1 m (Fig. 10b). In this respect, the influence of forward speed on soil-wheel interaction performance such as wheel sinkage and wheel slippage was investigated by simulation. The results showed that the relative wheel sinkage decreased with forward speed (Shmulevich, Mussel, & Wolf, 1998). The effect of speed on soil compaction was investigated in field experiments by Stafford and de Carvalho Mattos (1981). In one research, the effects of forward speed, wheel load, and the number of passes on the soil density of a soil bin were investigated. Cone index and soil sinkage were considered indicators of soil compaction. The results showed the highest soil compaction occurred with the lowest wheel speed (Taghavifar & Mardani, 2014). They reported that the reason for the increase in soil compaction at low speeds is the increase in the soil-wheel contact time.

A review of soil compaction studies by machinery traffic shows that increasing the speed (or decreasing the loading time) decreases the compaction effect. Simulation of soil as an elastic-plastic material in our simulations might be the reason why wheel sinkage did not vary with wheel speed. The viscous effect in the soil is the parameter that changes the soil deformation with varying loading times where a part of external energy is dissipated due to the viscous effect. Or and Ghezzehei (2002) developed a modified Hertzian contact model of paired particles including the viscous effect. Transient loading caused by tire traffic and increasing traffic speed showed an obvious decrease in soil deformation and an increase in contact stress. This suggests that the simulation of soil as a visco-elastoplastic material is a reasonable scenario for modeling the effect of traffic speed on soil stress and soil compaction as similarly concluded by Bahrami *et al.* (2023).

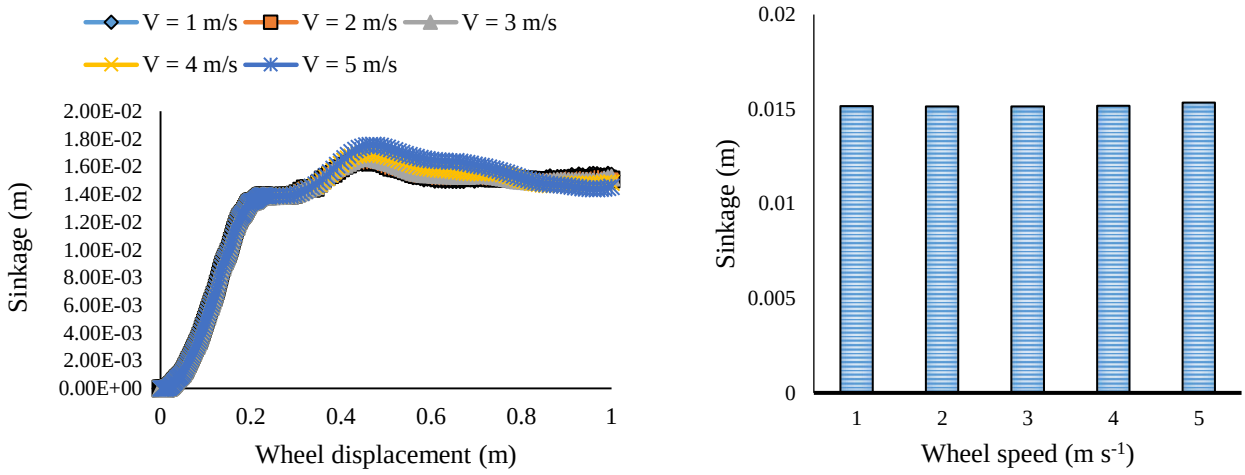

(a) (b)

Fig.10. (a) Simulated wheel sinkage as a function of wheel displacement, and (b) the average value of wheel sinkage between 0.6 and 1 m wheel displacement for different wheel speeds

Stress overestimation ratio and probe geometry

In a comparative study of the simulation of soil stress under plate sinkage loading using FEM and DEM, Bahrami *et al.* (2022) investigated the effect of probe geometry on the stress overestimation ratio. They found that the stress overestimation ratio decreased by increasing the ratio of housing diameter to sensor diameter. This suggested that a probe with a larger margin (i.e. the distance between the sensor and housing edge) has a smaller

stress concentration on the sensing surface of the probe. This is because the stress concentrates on the edge of the probe's housing. Hence, increasing the space between the probe housing edge and the sensing surface of the probe decreases the probe's stress reading. de Lima and Keller (2021) investigated the stress deviation of cylindrical probes as affected by probe design (material properties and probe height to diameter ratio), probe spacing in multi-probe setups, probe installation depth, and mechanical behavior of soil under static surface loading. However, the ratio of the probe housing diameter to the sensing's surface diameter was another factor first addressed by Bahrami *et al.* (2022) by modeling the stress probe in two pieces i.e. the probe housing and senor surface, installed under plate sinkage loading. A similar result was found under the moving wheel when the housing diameter was kept constant at 0.07 m and the sensor diameter was reduced from 0.06 m to 0.035 in 6 levels as shown in Fig. 11.

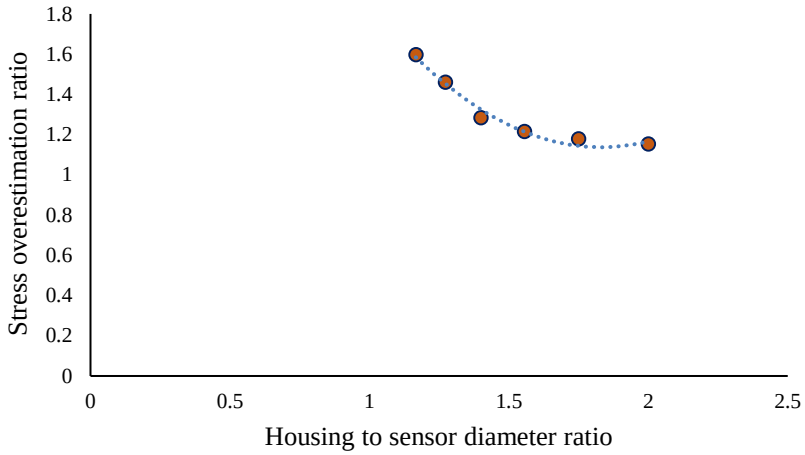

Fig.11. Stress overestimation ratio against housing to sensor diameter ratio

Conclusion

A finite element model of soil-stress probe interaction was developed to study the probe-induced stress deviation under a moving rigid wheel. Soil stress was analyzed in two conditions, with-probe stress, the stress measured or simulated with a cylindrical load cell probe, and without-probe, the soil's true stress simulated in the absence of the probe. The FEM-simulated with-probe stress was compared with the experimental stress measured in wheeling experiments in a soil bin. The following conclusions could be drawn:

1- Compared to the experimental stress, the model overestimated with-probe stress by 28.5%.
2- An average stress overestimation ratio, i.e. the ratio of simulated with-probe to without-probe stress, of 1.22 was found for the probe which is much smaller than that found under plate sinkage loading in a previous study. This was explained by the different boundary conditions and loading geometry of the wheel as compared to plate sinkage loading.
3- Wheeling speed had no noticeable effect on soil stress and stress overestimation ratio while stress overestimation ratio varied significantly with the probe's depth. Modeling the soil as an elastic-plastic material was discussed as the potential reason why soil stress and the resulting wheel sinkage did not vary with wheel speed. A minor increase in soil stress caused by increasing the speed might be due to inertial effects while the viscous effect is a more important aspect that needs further attention.

4- According to the results obtained under plate sinkage loading, increasing the ratio of the probe housing diameter to the sensor surface diameter decreased the stress overestimation ratio. This may suggest that, although the stress concentration is not only a function of probe geometry, the stress overestimation ratio could be minimized by optimizing the probe's design.
5- As compared to previous studies using DEM, a rather similar stress overestimation ratio was found under plate sinkage and wheel loading with DEM while the stress concentration ratio was significantly smaller under wheel loading than plate sinkage loading when modeled with FEM. This is likely explained by the continuum nature of FEM and the sponge effect on the soil surface which is strongly influenced by loading geometry.

Future studies could be aimed at studying soil stress propagation by parameterizing the soil as a visco-elastoplastic material to evaluate the effect of loading time on the resulting soil stress and deformation.

Acknowledgements

This study was conducted based on ideas from the third author's doctoral dissertation and the efforts of the second author who helped in FEM simulations. I, as the corresponding author, deeply regret that he (Dr. Hadi Azimi-Nejadian) passed away after the submission of this manuscript. I am sorry that we have lost an intelligent and hard-working scientist in the field of soil-machine interaction. God bless him.

References

1. ABAQUS, (2019). ABAQUS user's manuals version 6.19.1. Provid. RI ABAQUS, Inc. van den.
2. Acquah, K., & Chen, Y. (2021). Discrete element modeling of soil compaction of a press-wheel. *AgriEngineering*, *3*, 278-293. https://doi.org/10.3390/agriengineering3020019
3. Akker, J. J. (2004). SOCOMO: a soil compaction model to calculate soil stresses and the subsoil carrying capacity. *Soil and Tillage Research*, *79*, 113-127. https://doi.org/10.1016/j.still.2004.03.021
4. Arefi, M., Karparvarfard, S. H., Azimi-Nejadian, H., & Naderi-Boldaji, M. (2022). Draught force prediction from soil relative density and relative water content for a non-winged chisel blade using finite element modelling. *Journal of Terramechanics*, *100*, 73-80. https://doi.org/10.1016/j.jterra.2022.01.001
5. Azimi-Nejadian, H., Karparvarfard, S. H., Naderi-Boldaji, M., & Rahmanian-Koushkaki, H. (2019). Combined finite element and statistical models for predicting force components on a cylindrical mouldboard plough. *Biosystems Engineering*, *186*, 168-181. https://doi.org/10.1016/j.biosystemseng.2019.07.007
6. Bahrami, M., Naderi-Boldaji, M., Ghanbarian, D., & Keller, T. (2022). Simulation of soil stress under plate sinkage loading: A comparison of finite element and discrete element methods. *Soil and Tillage Research*, *223*, 105463. https://doi.org/10.1016/j.still.2022.105463
7. Bahrami, M., Naderi-Boldaji, M., Ghanbarian, D., & Keller, T. (2023). Discrete element modelling of stress propagation in soil under a rigid wheel in a soil bin: a simulation of probe inducing stress deviation and wheel speed. *Biosystems Engineering*, *230*, 159-170. https://doi.org/10.1016/j.biosystemseng.2023.04.013
8. Bolling, I. H. (1985). How to predict soil compaction from agricultural tires. *Journal of Terramechanics*, *22*(4), 205-223. https://doi.org/10.1016/0022-4898(85)90017-5
9. Boussinesq, M. J. (1885). Application Des Potentiels. Gauthier-Villars. https://books.google.com/books?id¼IYvpq89K_O8C
10. Cueto, O. G., Coronel, C. E. I., Bravo, E. L., Morfa, C. A. R., & Suárez, M. H. (2016). Modelling in FEM the soil pressures distribution caused by a tyre on a Rhodic Ferralsol

soil. *Journal of Terramechanics*, *63*, 61-67. https://doi.org/10.1016/j.jterra.2015.09.003
11. de Lima, R. P., & Keller, T. (2021). Soil stress measurement by load cell probes as influenced by probe design, probe position, and soil mechanical behavior. *Soil and Tillage Research*, *205*, 104796. https://doi.org/10.1016/j.still.2020.104796
12. De Pue, J., & Cornelis, W. M. (2019). DEM simulation of stress transmission under agricultural traffic Part 1: Comparison with continuum model and parametric study. *Soil and Tillage Research*, *195*, 104408. https://doi.org/10.1016/j.still.2019.104408
13. De Pue, J., Lamandé, M., & Cornelis, W. (2020). DEM simulation of stress transmission under agricultural traffic Part 2: Shear stress at the tyre-soil interface. *Soil and Tillage Research*, *203*, 104660. https://doi.org/10.1016/j.still.2020.104660
14. Farhadi, P., Golmohammadi, A., Sharifi Malvajerdi, A., & Shahgholi, G. (2020). Finite element modeling of the interaction of a treaded tire with clay-loam soil. *Computers and Electronics in Agriculture*, *162*, 793-806. https://doi.org/10.1016/j.compag.2019.05.031
15. Frohlich, O. K. (1934). Druckverteilung im Baugrunde. Springer Verlag, Wien, pp. 178
16. Gheshlaghi, F., & Mardani, A. (2021). Prediction of soil vertical stress under off-road tire using smoothed-particle hydrodynamics. *Journal of Terramechanics*, *95*, 7-14. https://doi.org/10.1016/j.jterra.2021.02.004
17. Hamza, M. A., & Anderson, W. K. (2005). Soil compaction in cropping systems: A review of the nature, causes and possible solutions. *Soil and Tillage Research*, *82*(2), 121-145. https://doi.org/10.1016/j.still.2004.08.009
18. Horn, R., Blackwell, P. S., & White, R. (1989). The effect of speed of wheeling on soil stresses, rut depth and soil physical properties in an ameliorated transitional red-brown earth. *Soil and Tillage Research*, *13*, 353e364. https://doi.org/10.1016/0167-1987(89)90043-3
19. Ibrahmi, A., Bentaher, H., Hbaieb, M., Maalej, A., & Mouazen, A. M. (2015). Study the effect of tool geometry and operational conditions on mouldboard plough forces and energy requirement: Part 1. Finite element simulation. *Computers and Electronics in Agriculture*, *117*, 258-267. https://doi.org/10.1016/j.compag.2015.08.006
20. Jimenez, K. J., Rolim, M. M., Gomes, I. F., de Lima, R. P., Berrío, L. L. A., & Ortiz, P. F. (2021). Numerical analysis applied to the study of soil stress and compaction due to mechanised sugarcane harvest. *Soil and Tillage Research*, *206*, 104847. https://doi.org/10.1016/j.still.2020.104847
21. Keller, T., Défossez, P., Weisskopf, P., Arvidsson, J., & Richard, G. (2007). SoilFlex: A model for prediction of soil stresses and soil compaction due to agricultural field traffic including a synthesis of analytical approaches. *Soil and Tillage Research*, *93*(2), 391-411. https://doi.org/10.1016/j.still.2006.05.012
22. Keller, T., Lamandé, M., Naderi-Boldaji, M., & de Lima, R. P. (2022). *Soil Compaction Due to Agricultural Field Traffic: An Overview of Current Knowledge and Techniques for Compaction Quantification and Mapping*. In: Saljnikov, E., Mueller, L., Lavrishchev, A., Eulenstein, F. (eds) Advances in Understanding Soil Degradation. Innovations in Landscape Research. Springer, Cham. https://doi.org/10.1007/978-3-030-85682-3_13
23. Keller, T., Ruiz, S., Stettler, M., & Berli, M. (2016). Determining soil stress beneath a tire: measurements and simulations. *Soil Science Society of America Journal*, *80*(3), 541-553. https://doi.org/10.2136/sssaj2015.07.0252
24. Khalid, U., Farooq, K., & Mujtaba, H. (2018). On yield stress of compacted clays. *International Journal of Geo-Engineering*, *9*(1), 1-16. https://doi.org/10.1186/s40703-018-0090-2
25. Kirby, J. M. (1999a). Soil stress measurement: Part I. Transducer in a uniform stress field. *Journal of Agricultural Engineering Research*, *72*(2), 151-160. https://doi.org/10.1006/jaer.1998.0357

26. Kirby, J. M. (1999b). Soil stress measurement. Part 2: transducer beneath a circular loaded area. *Journal of Agricultural Engineering Research*, *73*(2), 141-149. https://doi.org/10.1006/jaer.1998.0400
27. Koolen, A. J., & Kuipers, H. (1983). *Agricultural Soil Mechanics: Advanced Series in Agricultural Sciences* 13. Springer, Heidelberg, 241 pp. https://doi.org/10.1007/978-3-642-69010-5
28. Labuz, J. F., & Theroux, B. (2005). Laboratory calibration of earth pressure cells. *Geotechnical Testing Journal*, *28*(2), 188-196. https://doi.org/10.1520/GTJ12089
29. Mahboub Yangeje, H., & Mardani, A. (2022). Investigating the interaction between soil and cultivator blade by numerical simulation and validation of results by soil bin tests. *Journal of Agricultural Machinery*, *12*(4), 587-599. (in Persian with English abstract). https://doi.org/10.22067/jam.2021.70572.1041
30. Naderi-Boldaji, M., Alimardani, R., Hemmat, A., Sharifi, A., Keyhani, A., Tekeste, M. Z., & Keller, T. (2013). 3D finite element simulation of a single-tip horizontal penetrometer–soil interaction. Part I: Development of the model and evaluation of the model parameters. *Soil and Tillage Research*, *134*, 153-162. https://doi.org/10.1016/j.still.2013.08.002
31. Naderi-Boldaji, M., Kazemzadeh, A., Hemmat, A., Rostami, S., & Keller, T. (2018). Changes in soil stress during repeated wheeling: A comparison of measured and simulated values. *Soil Research*, *56*(2), 204-214. https://doi.org/10.1071/SR17093
32. Naderi-Boldaji, M., Hajian, A., Ghanbarian, D., & Bahrami, M. (2018). Finite element simulation of plate sinkage, confined and semi-confined compression tests: A comparison of the response to yield stress. *Soil and Tillage Research*, *179*, 63-70. https://doi.org/10.1016/j.still.2018.02.003
33. Naderi-Boldaji, M., Karparvarfard, S. H., & Azimi-Nejadian, H. (2023). Investigation of the predictability of mouldboard plough draught from soil mechanical strength (cone index *vs.* shear strength) using finite element modelling. *Journal of Terramechanics*, *108*, 21-31. https://doi.org/10.1016/j.jterra.2023.04.001
34. Nawaz, M. F., Bourrie, G., & Trolard, F. (2013). Soil compaction impact and modelling. A review. *Agronomy for sustainable development*, *33*, 291-309. https://doi.org/10.1007/s13593-011-0071-8
35. Or, D., & Ghezzehei, T. A. (2002). Modeling post-tillage soil structural dynamics: a review. *Soil and Tillage Research*, *64*(1-2), 41-59. https://doi.org/10.1016/S0167-1987(01)00256-2
36. Peth, S., Horn, R., Fazekas, O., & Richards, B. G. (2006). Heavy soil loading its consequence for soil structure, strength, deformation of arable soils. *Journal of Plant Nutrition and Soil Science*, *169*(6), 775-783. https://doi.org/10.1002/jpln.200620112
37. Pytka, J. A. (2013). *Dynamics of wheelesoil systems: A soil stress and deformation-based approach*. CRC Press, Taylor & Francis Group, LLC. https://doi.org/10.1201/b12729
38. Rücknagel, J., Hofmann, B., Deumelandt, P., Reinicke, F., Bauhardt, J., Hülsbergen, K. J., & Christen, O. (2015). Indicator based assessment of the soil compaction risk at arable sites using the model REPRO. *Ecological Indicators*, *52*, 341-352. https://doi.org/10.1016/j.ecolind.2014.12.022
39. Schjønning, P., Lamandé, M., Tøgersen, F. A., Arvidsson, J., & Keller, T. (2008). Modelling effects of tyre inflation pressure on the stress distribution near the soil–tyre interface. *Biosystems Engineering*, *99*(1), 119-133. https://doi.org/10.1016/j.biosystemseng.2007.08.005
40. Shahgholi, G., Ghafouri Chiyaneh, H., & Mesri Gundoshmian, T. (2018). Modeling of soil compaction beneath the tractor tire using multilayer perceptron neural networks. *Journal of Agricultural Machinery*, *8*(1), 105-118. (in Persian with English abstract).

https://doi.org/10.22067/jam.v8i1.58891
41. Shmulevich, I., Mussel, U., & Wolf, D. (1998). The effect of velocity on rigid wheel performance. *Journal of Terramechanics*, *35*(3), 189-207. https://doi.org/10.1016/S0022-4898(98)00022-6
42. Silva, R. P., Rolim, M. M., Gomes, I. F., Pedrosa, E. M., Tavares, U. E., & Santos, A. N. (2018). Numerical modeling of soil compaction in a sugarcane crop using the finite element method. *Soil and Tillage Research*, *181*, 1-10. https://doi.org/10.1016/j.still.2018.03.019
43. Söhne, W. (1953). Druckverteilung im Boden und Bodenformung unter Schlepperreifen (Pressure distribution in the soil and soil deformation under tractor tyres). *Grundl Land Technik*, *5*, 49-63. https://doi.org/10.1007/BF01512930
44. Stafford, J. V., & de Carvalho Mattos, P. (1981). The effect of forward speed on wheel-induced soil compaction: laboratory simulation and field experiments. *Journal of Agricultural Engineering Research*, *26*(4), 333-347. https://doi.org/10.1016/0021-8634(81)90075-5
45. Stettler, M., Keller, T., Weisskopf, P., Lamandé, M., Lassen, P., & Schjønning, P. (2014). Terranimo®–a web-based tool for evaluating soil compaction. *Landtechnik*, *69*(3), 132-138.
46. Taghavifar, H., & Mardani, A. (2014). Effect of velocity, wheel load and multipass on soil compaction. *Journal of the Saudi Society of Agricultural Sciences*, *13*(1), 57-66. https://doi.org/10.1016/j.jssas.2013.01.004
47. Ucgul, M., Saunders, C., & Fielke, J. M. (2017). Particle and geometry scaling of the hysteretic spring/linear cohesion contact model for discrete element modelling of soil-tool simulation. ASABE Paper No. 1701372. St. Joseph, MI: ASABE. https://doi.org/10.13031/aim.201701372
48. Van den Akker, J. J. H. (2004). SOCOMO: a soil compaction model to calculate soil stresses and the subsoil carrying capacity. *Soil and Tillage Research*, *79*(1), 113-127. https://doi.org/10.1016/j.still.2004.03.021
49. Weiler Jr, W. A., & Kulhawy, F. H. (1982). Factors affecting stress cell measurements in soil. *Journal of the Geotechnical Engineering Division*, *108*(12), 1529-1548. https://doi.org/10.1061/AJGEB6.0001393
50. Xia, K. (2011). Finite element modeling of tire/terrain interaction: Application to predicting soil compaction and tire mobility. *Journal of Terramechanics*, *48*(2), 113-123. https://doi.org/10.1016/j.jterra.2010.05.001

نشریه ماشین‌های کشاورزی
https://jame.um.ac.ir

مقاله پژوهشی

جلد ۱۴، شماره ۱، بهار ۱۴۰۳، ص ۶۷-۴۹

یک مدل اجزای محدود برهم‌کنش کاوشگر تنش-خاک زیر یک چرخ صلب متحرک

مجتبی نادری بلداجی[1*]، هادی عظیمی نژادیان[2]، مصطفی بهرامی[3]

تاریخ دریافت: ۱۴۰۲/۰۶/۰۷
تاریخ پذیرش: ۱۴۰۲/۰۷/۱۷

چکیده

تردد ماشین‌های کشاورزی با اعمال تنش بر سطح خاک دلیل اصلی تراکم خاک‌های کشاورزی است. مطالعه انتشار تنش در خاک نیاز به اندازه گیری تنش در خاک دارد، در حالی‌که تنش اندازه‌گیری‌شده با نصب هر نوع کاوشگر ممکن است با تنش واقعی خاک، یعنی تنش خاک در غیاب کاوشگر متفاوت باشد. این مطالعه با هدف شبیه‌سازی برهم‌کنش کاوشگر تنش در زیر یک چرخ صلب متحرک با استفاده از روش اجزای محدود به‌منظور بررسی تطابق تنش شبیه‌سازی‌شده با کاوشگر با تنش تجربی اندازه‌گیری‌شده در یک مخزن خاک انجام شد. خاک به‌عنوان یک ماده کشسان- خمیری مدل‌سازی و خواص آن با شبیه‌سازی نفوذ مخروط و نشست چرخ در خاک کالیبره شد. نتایج نشان داد که تنش به‌دست‌آمده از پروب با روش اجزای محدود به‌طور متوسط ۲۸ درصد بیش‌تخمینی در مقایسه با تنش تجربی برای بارهای چرخ ۶۰۰ و ۱۲۰۰ نیوتن داشته است. میانگین نسبت شبیه‌سازی‌شده تنش با کاوشگر به تنش بدون کاوشگر برای دو آزمون ۱/۲۲ به‌دست آمد که به‌طور معنی‌داری کوچک‌تر از همین نسبت تحت بارگذاری نشست صفحه دایره‌ای با مقدار ۱/۹ بود و همچنین به‌طور قابل‌توجهی بزرگ‌تر از نتیجه به‌به‌دست‌آمده از روش اجزای گسسته است. افزایش سرعت حرکت چرخ افزایشی جزئی در تنش خاک را نشان داد. نسبت بیش تخمینی تنش (همان نسبت تنش با کاوشگر به تنش بدون کاوشگر) به‌طور قابل‌توجهی با عمق افزایش یافت ولی افزایش کمی با سرعت در عمق زیر ۰/۲ متر داشت.

واژه‌های کلیدی: انباره خاک، تردد ماشین، تنش خاک، شبیه‌سازی اجزای محدود، کاوشگر تنش

۱- بخش مهندسی مکانیک بیوسیستم، دانشکده کشاورزی، دانشگاه شهرکرد، شهرکرد، ایران
۲- استادیار، بخش مهندسی مکانیک بیوسیستم، دانشکده کشاورزی، دانشگاه جهرم، جهرم، ایران
۳- دانش‌آموخته دکتری، بخش مهندسی مکانیک بیوسیستم، دانشکده کشاورزی، دانشگاه شهرکرد، شهرکرد، ایران
(*- نویسنده مسئول: Email: naderi.mojtaba@sku.ac.ir)

https://doi.org/10.22067/jam.2023.84158.1185

Journal of Agricultural Machinery

Homepage: https://jame.um.ac.ir

Research Article
Vol. 14, No. 1, Spring 2024, p. 69-82

Modeling Soil Pressure-Sinkage Characteristic as Affected by Sinkage rate using Deep Learning Optimized by Grey Wolf Algorithm

B. Golanbari[1], A. Mardani[1*], A. Hosseinpour[1], H. Taghavifar[2]

1- Department of Mechanics Engineering of Biosystems, Urmia University, Urmia, Iran
2- Department of Mechanical, Industrial and Aerospace Engineering, Concordia University, Concordia, Canada
(*- Corresponding Author Email: a.mardani@urmia.ac.ir)

Received: 09 September 2023
Revised: 01 November 2023
Accepted: 04 November 2023
Available Online: 04 November 2023

How to cite this article:
Golanbari, B., Mardani, A., Hosseinpour, A., & Taghavifar, H. (2024). Modeling Soil Pressure-Sinkage Characteristic as Affected by Sinkage rate using Deep Learning Optimized by Grey Wolf Algorithm. *Journal of Agricultural Machinery*, *14*(1), 69-82. https://doi.org/10.22067/jam.2023.84339.1188

Abstract

Due to the numerous variables that may influence the soil-machine interaction systems, predicting the mechanical response of soil interacting with off-road traction equipment is challenging. In this study, deep neural networks (DNNs) are chosen as a potential solution for explaining the varying soil sinkage rates because of their ability to model complex, multivariate, and dynamic systems. Plate sinkage tests were carried out using a Bevameter in a fixed-type soil bin with a 24 m length, 2 m width, and 1 m depth. Experimental tests were conducted at three sinkage rates for two plate sizes, with a soil water content of 10%. The provided empirical data on the soil pressure-sinkage relationship served as the basis for an algorithm capable of discerning the soil-machine interaction. From the iterative process, it was determined that a DNN, specifically a feed-forward back-propagation DNN with three hidden layers, is the optimal choice. The optimized DNN architecture is structured as 3-8-15-10-1, as determined by the Grey Wolf Optimization algorithm. While the Bekker equation had traditionally been employed as a widely accepted method for predicting soil pressure-sinkage behavior, it typically disregarded the influence of sinkage velocity of the soil. However, the findings revealed the significant impact of sinkage velocity on the parameters governing the soil deformation response. The trained DNN successfully incorporated the sinkage velocity into its structure and provided accurate results with an MSE value of 0.0871.

Keywords: Bevameter, Deep neural network, Off-road vehicle, Soil bin, Terramechanics

Introduction

A Bevameter can be used for calculating soil parameters through pressure-sinkage relationships. The obtained pressure-sinkage models are used to analyze the soil interaction with the vehicle tires. In this method, the investigation and analysis of soil-tire interaction also requires the measurement of the mechanical parameters of soil. The traction force created by the driving wheel, as well as the soil compaction due to vehicle traffic, are the results of the interaction between soil and tire. Factors such as traction, performance prediction, design, and stability of off-road vehicles can be analyzed through pressure-sinkage models (He, Wu, Ma, Wang, & Li, 2019). Therefore, any improvement in soil-tire interaction has a direct effect on the performance of off-road vehicles and equipment and reduces fuel consumption.

The experimental method is one of the essential methods for soil behavior modeling. In this research, the soil resistance versus penetration depth is measured. Researchers are interested in using these equations because many of the wheel and soil parameters are not included which results in ease of measurement. To develop pressure-sinkage

https://doi.org/10.22067/jam.2023.84339.1188

relationships of loading plates for homogeneous soil, Bekker presented Eq. 1 using the Bevameter device (Bekker, 1957).

$$P = \left(\frac{K_c}{b} + K_\varphi\right).Z^n \quad (1)$$

Where P is the vertical pressure (kPa), n is the deformation equation exponent, K_c is the modulus of cohesion of the deformed soil (kN/m^{n+1}), K_φ is the modulus of friction of the deformed soil (kN/m^{n+2}), Z is sinkage of the loading plate (cm), and b is the smallest dimension of the plate (m). To calculate the coefficients of Eq. 1 based on Bekker's method, two loading plates with different widths should be used to solve the equation.

One popular method for soft computing is an artificial neural network (ANN), which is composed of interconnected neurons following specific algorithms. These networks are inspired by the human brain's structure and functioning and are used for pattern recognition (Taghavifar & Mardani, 2014b). Neural networks encompass machine learning algorithms that classify input data and produce desired outputs. They have multiple applications including pattern recognition, data classification, prediction, modeling, control, and robotics (Haykin, 1999; Roul *et al.*, 2009). ANNs are utilized to facilitate solving complex problems in various scientific and engineering fields, mainly where conventional mathematical modeling is not successful (Taghavifar & Mardani, 2014a). Deep Neural Networks (DNNs) utilize deep architectures with multiple hidden layers and identify complex patterns and relationships in datasets. They are trained with experimental data and are then validated and tested using independent datasets. DNNs achieve high performance and accuracy by minimizing the mean square error. The iterative exploration process and backpropagation allow DNNs to establish the optimal input-output relationship. After training, the model can be extended with new input values to predict, simulate, and re-establish the identified conditions of the test method. Fernandes *et al.* (2020), conducted experiments to evaluate the accuracy of ANN models in estimating soil infiltration resistance with standardized moisture. Based on soil infiltration resistance measured in the field and on soil moisture, the models used were obtained by multiple linear and nonlinear regression and ANNs. Pham *et al.* (2019), proposed a hybrid machine learning approach called MLP-BBO to predict the stabilization coefficient of soft soil. This method was based on the multilayer perceptron (MLP) neural network and Biogeography Based Optimization (BBO). Roul *et al.* (2009), used the ANN model to predict the behavior of tillage tools in different operating conditions and soil. Zhang & Kushwaha, (1999) used the radial basis function (RBF) in the artificial neural networks to estimate the draft force of thin blades in soil under multiple input variables. Taghavifar *et al.* (2013), used a neural network to investigate the wheel's behavior with soil under the influence of movement speed, vertical load, and tire pressure. To improve tractor performance on silty clay loam soil, Pieczarka *et al.* (2018) investigated the effects of soil moisture, soil compaction, horizontal soil deformation, and vertical load on traction force using MLP and RBF neural networks. The most efficient model was the MLP neural network.

Bekker´s method is a standard method used by researchers to determine soil parameters on a large scale and is simple to calculate. However, it has some shortcomings in field tests. Although the penetration velocity of the plates in the soil affects the soil sinkage, its effect is not taken into account in Bekker's method and other methods that are developed based on it (Kruger, Els, & Hamersma, 2023). The purpose of this research is to model the pressure-sinkage relationship with deep artificial neural networks and to investigate the effect of sinkage rate (which is related to loading time and machine speed) on the soil parameters. Lastly, the results of the modeling are compared with the experimental results.

Materials and Methods

Data acquisition

The plate sinkage experiments were carried out using a Bevameter installed on the carrier

unit of a soil bin in the Terramechanics laboratory of Urmia University, Iran. The soil bin is a fixed-linear type soil bin with a 24 m length, 2 m width, and 1 m depth soil channel and provides optimal conditions for conducting experiments by eliminating boundary effects (Gheshlaghi & Mardani, 2021). The Bevameter utilized in this research consists of mechanical, electrical, and electronic parts. The mechanical part includes the chassis, worm gearbox, Rack and pinion gear mechanism, shell, shaft, one-way jack, and plates, as shown in Fig. 1. The mechanical part of the device works in such a way that the rotational movement of the gearbox is converted into linear movement by the Rack and pinion gear mechanism. The electrical and electronic parts control the system and apply the force to the soil, measure the pressure-sinkage of soil data, and process, and record the measurement data. An electric motor with a power of 5.5 kW and a nominal speed of 1430 rpm was utilized to start the system and supply the driving force. In addition to a worm gear reducer with three-speed reduction ratios (6, 12, and 19), an inverter (LS, produced by LG in South Korea) was used to control the rotational speed of the electric motor. By combining the 1:19 reduction ratio of the gearbox with the frequency adjustment of the inverter, three desired sinkage rates of 15, 30, and 45 mm/s were obtained for the experiments. To measure the force applied to the probes, an S-shaped load cell (Bongshin DBBP, made in South Korea) with a nominal capacity of 1000 kg and an accuracy of 0.02 kg was used for the experiments. A linear encoder (ATEK MLC320, made in Turkey) was utilized to measure the amount of soil deformation (sinkage). The displacement measurement system of the linear encoder is magnetic with a measurement length of 400 mm, a maximum movement speed of 300 mm s^{-1}, and a repeatability of ± 1 pulse (Mahboub Yangeje & Mardani Korani, 2021).

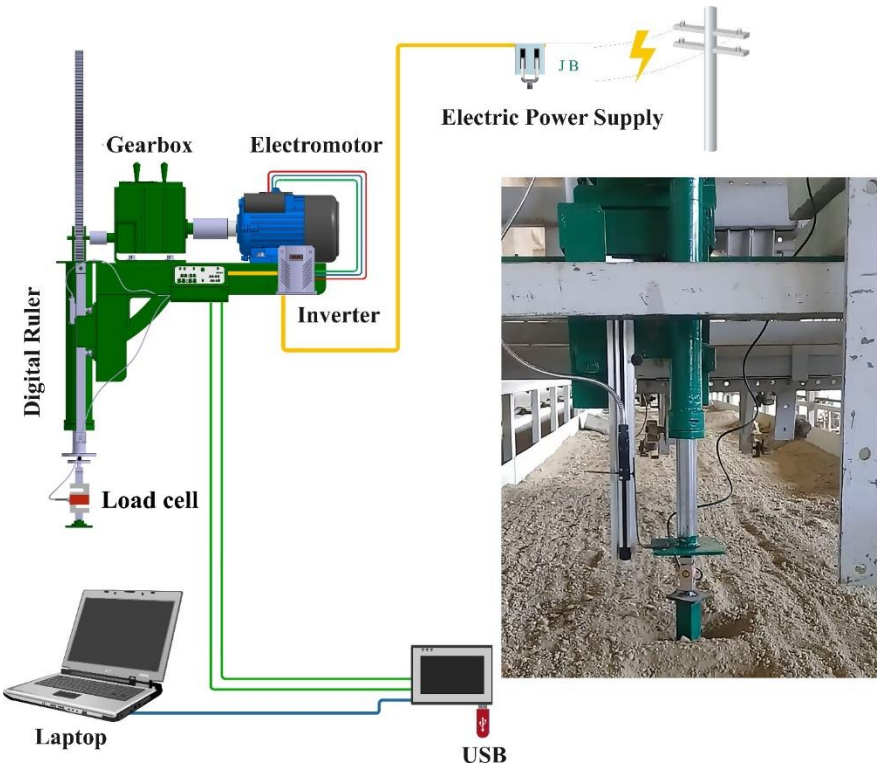

Fig.1. Bevameter installed on the soil bin carrier

Considering that the shape of the loading plates affects the pressure-sinkage relationship, the aspect ratio of the loading plates is considered in the standard range of

1.4-6, which is similar to Bekker's term pressure-sinkage patterns (Van *et al.*, 2008). The dimensions of the rectangular plates for experimental tests were 175×70 and 105×70 mm^2.

Eq. 2 is used to determine the output speed of the electric motor that is applied to the input of the gearbox to control the speed of the probe and the velocity value included in Eq. 2 for obtaining the electric motor rotation value corresponds with this speed.

$$n = \frac{i \times V \times 60}{75} \quad (2)$$

Where, n is the prediction of the rotational output speed of the electric motor, which is applied based on the sinkage rate of the plate to the gearbox input and is in revolutions per minute, i is the transmission ratio of the gearbox, and V is the optimal sinkage velocity for the test, for which three velocities of 15, 30, and 45 mm s^{-1} were used in the tests. The number 75 is a constant in the formula and represents the displacement ratio of the rack per rotation of the pinion in millimeters.

In this research, one of the Bekker loading plates was installed on the device at each stage of the experimental tests to measure soil parameters. Force is applied to the plates based on the defined conditions. The force-displacement values were simultaneously recorded in the data logger by the load cell and the digital ruler. The files recorded by the data logger were extracted as text files and transferred to the MATLAB software (Version 9.2.0.5, MathWorks) for processing. The dependent (output) variable and the independent variables (inputs) and their levels are shown in Table 1.

Table 1- Summary of inputs and output variables ranges

Input (Independent variables)	Parameter	Unit	Levels		
1	Pressure	kPa	0-250		
2	Velocity	mm s^{-1}	15	30	45
3	Plate width	mm	105	175	
Output (dependent variable)					
1	Sinkage	mm			

The soil bin was filled with clay-loam soil, which has the same texture and characteristics (Table 2) as that of the natural soil in the geographical area of the laboratory where the study took place.

Table 2- Physical characteristics of the soil in the test soil bins

Parameter	Value
Sand	35%
Silt	22%
Clay	43%
humidity	10%
Bulk density	2630 kg m^{-3}
Young's modulus	0.3 MPa
Poisson's ratio	0.29
The angle of internal friction	32
Liquid limit	42.7%
Plasticity index	13.3%

After preparing the test setup, experiments were performed in three repetitions for each level of sinkage rate. Each of the plates was installed on the Bevameter and the force was applied to the plate. The force-displacement values were recorded simultaneously with the load cell sensors and the linear encoder in the data logger.

Deep neural network presentation

The advanced capabilities of deep learning methods have made it possible to predict the interaction between soil and tools accurately without the need for simplification or the removal of influential factors. Predicting these interactions with DNNs using inputs (independent variables) has an undeniable advantage over traditional methods. The Gray Wolf Optimization (GWO) algorithm, known for its effectiveness in optimization tasks, was utilized to fine-tune the structure and hyperparameters of the DNN. In the methodology of deep neural networks (DNN)

used in this study, two approaches were employed to determine the hyperparameters of the neural network. In the first approach, a trial and error method was used to determine the total number of neurons in the hidden layers, as well as the learning rate and momentum. In the second approach, the GWO algorithm was utilized to determine the optimal architecture, momentum, and learning rate in the DNN. In the first approach, the number of hidden layers for each layer increased linearly from one to 15, and the best topology with the lowest MSE was selected as the neural network architecture. This dataset consisted of 1488 data points, and a total of 225 repetitions for each training was conducted with 1000 iterations. 15 percent of the data were randomly separated as unseen data to assess the performance of the neural network after training. Of the remaining dataset, 68% of the data was used as training data, 17% as validation data, and 15% as test data. Since the actual outputs for performance assessment after training are available, this type of data division ensures that the network is not overtrained. In Table 3, the statistical information and the span of input data are shown for the training, validation, and test sections, respectively. According to this statistical data, it can be seen that the data used for each stage of training, validation, and testing are uniform and consistent under the effects of pressure, velocity, the width of plates, and sinkage. Additionally, the standard deviation values for each variable can be seen in Table 3.

Table 3- Statistical properties of training, validation, and testing samples

Partition	Source	Minimum	Maximum	Mean	Standard deviation
Training	Pressure	3.04	249.88	118.34	66.39
	Velocity	15	45	30	11.75
	Plate width	105	175	140	35
	Sinkage	0.87	70	34	20.26
Validation	Pressure	3.39	245.18	115.84	65.80
	Velocity	15	45	30	12.7
	Plate width	105	175	140	35.05
	Sinkage	0.85	70	33.27	19.86
Testing	Pressure	3.96	249.30	126.67	69.26
	Velocity	15	45	30	11.95
	Plate width	105	175	140	35.10
	Sinkage	0.78	70	36.66	21.24

To train the network using the GWO algorithm, in the first step, the algorithm was applied to the hidden layers to achieve the best topology. Three different structures of the algorithm with 5, 10, and 15 gray wolves were used, with 20 iterations for each topology and 500 iterations for network training. In the second step, the GWO algorithm was employed on the selected topology to determine the optimal values for the learning rate and momentum. The optimization algorithm design in this stage was similar to the first stage. The search range for the number of neurons in each hidden layer for the GWO algorithm was set to 30. The overall schematic of the DNN using the GWO algorithm to find the most optimal arrangement of neurons in the hidden layers and to find the best learning rate and momentum values is shown in Fig. 2.

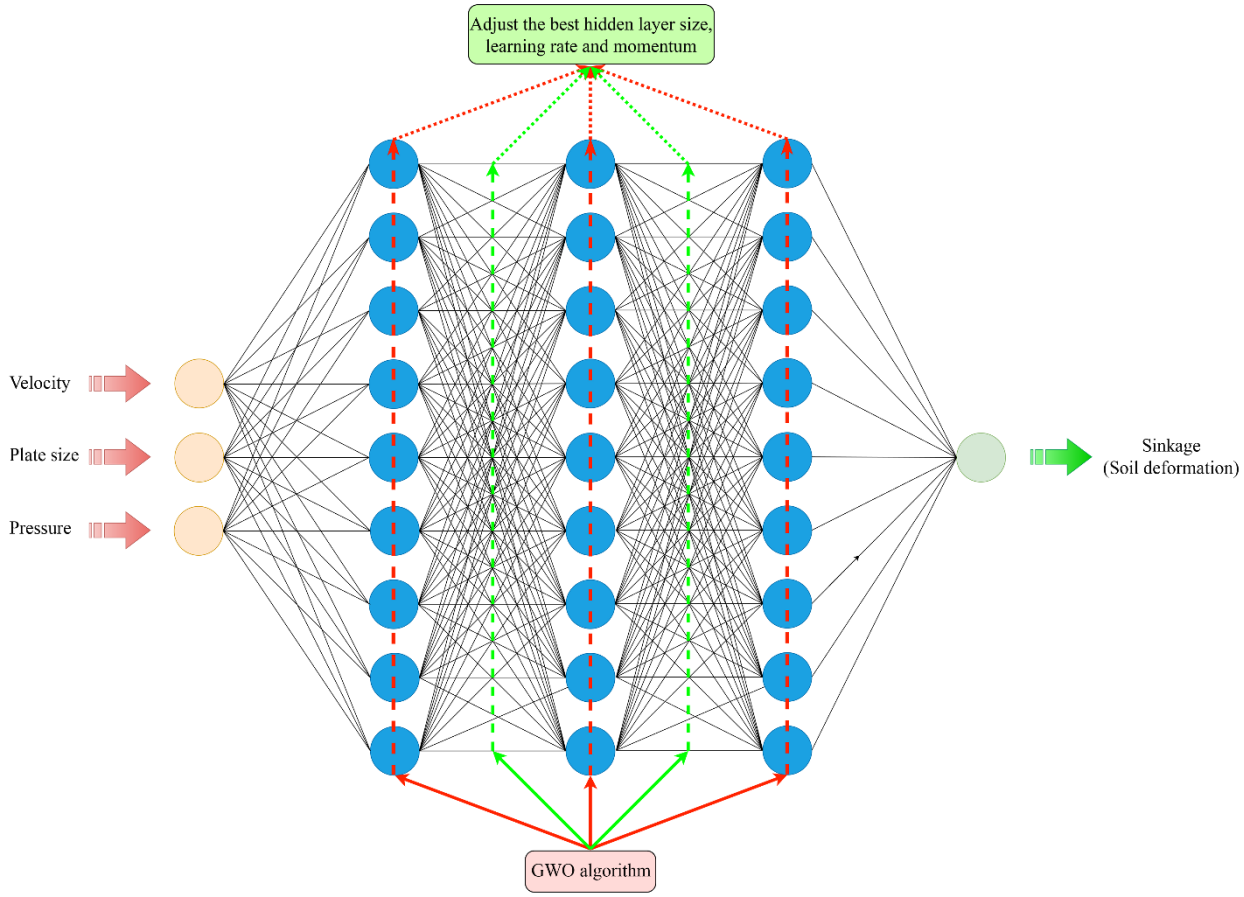

Fig.2. General multilayer perceptron DNN forward configuration with three hidden layers and applying the gray wolf algorithm to obtain the best network topology and set the learning rate and momentum

The performance of the DNN during the training, validation, and testing stages was evaluated using the Mean Squared Error (MSE), defined as Eq. 3.

$$MSE = \frac{1}{n}\sum_{i=1}^{n}\left(Y_i - \hat{Y}_i\right)^2 \quad (3)$$

Here, Y_i is the output from the field experiment (actual value) $\hat{Y}_i$ is the output obtained by the neural network (predicted value), and n is the number of iterations used in each step. Smaller values of MSE indicate better performance of the DNN. Therefore, the values close to zero were the basis of decision-making for the better performance of the neural network (Taghavifar *et al.*, 2015).

Results and Discussion

The selection of the learning algorithm for the neural network, specifically using the backpropagation algorithm, along with the choice of the activation function, is among the most crucial settings of the DNNs to achieve suitable convergence. The sigmoid activation function was selected for all three hidden layers. To choose the learning algorithm, a trial and error approach was employed, testing seven back propagation-based learning algorithms. The algorithm that resulted in the lowest Mean Squared Error (MSE) was used as the learning algorithm in the network. The results of training the neural network with various learning algorithms are presented in Table 4.

Table 4- Training functions and performance of neural networks developed based on train functions

Transfer function	Training algorithms	R	MSE
trainlm	Levenberg-Marquardt backpropagation	0.99900	0.0837
trainrp	Resilient backpropagation	0.99965	0.2711
traincgp	Conjugate gradient backpropagation with Polak-Ribiére updates	0.99955	0.3821
traingda	Gradient descent with adaptive learning rate backpropagation	0.99349	4.5175
traincgb	Conjugate gradient backpropagation with Powell-Beale restarts	0.99966	0.2884
trainoss	One-step secant backpropagation	0.99961	0.3156
trainbr	Bayesian regularization backpropagation	0.99987	0.1084

As inferred from Table 4, the Levenberg-Marquardt learning function exhibited better performance compared to other learning functions. Therefore, this algorithm was selected as the learning algorithm. It should be mentioned that all the training steps of both types of networks used in this research are similar.

As previously mentioned, one of the selected methods for determining the hyperparameters was the utilization of the GWO algorithm. The values obtained from the output of the GWO algorithm were compared with each other to select the best topology. Table 5 shows the output of the DNN from the output of the GWO algorithm.

Table 5- Features obtained in DNN training with different combinations of the number of wolves and topologies

DNN Property	GWO-Numbers of wolf								
	5	10	15	5	10	15	5	10	15
DNN-Topology	3-8-15-10-1			3-15-10-29-1			3-23-4-18-1		
Best Momentum	0.8759	0.8646	0.2605	0.5323	0.1614	0.4105	0.3045	0.9566	0.9026
Best Learning rate	0.2375	0.1263	0.5832	0.8797	0.3137	0.7187	0.6409	0.7538	0.2042
Mse Training	0.0919	0.0837	0.0991	0.0918	0.1091	0.0986	0.0969	0.0934	0.0973

As seen in Table 5, the best performance of the neural network corresponds to the topology 3-8-15-10-1, which has three inputs consisting of the penetration rate of pages into the soil, page size, and the vertical pressure applied to the pages. The network structure includes 8 neurons in the first hidden layer, 10 neurons in the second hidden layer, and 15 neurons in the third hidden layer, with the output representing soil deformation. Furthermore, the optimal values were found to be 0.864628 for momentum and 0.126314 for learning rate resulting in a mean squared error of 0.089405. The best results were achieved when the population of gray wolves in the GWO algorithm was set to 30.

Table 6 shows the soil parameters using Bekker's method at different speeds which are extracted using Eq. 1 and the data obtained from the experimental tests. The Bevameter test method lacks standardized testing procedures and requires further investigation into the factors influencing the tests (Kruger *et al.*, 2023). Sinkage rate is considered one of the key factors in modeling the dynamics of soft soil. Table 6 presents the effects of variations in sinkage rate on determining soil parameters.

Table 6- Soil parameters with the Bekker's method at different velocities

Bekker′s constant	Velocity (mm s^{-1})		
	15	30	45
K_φ (kN/m^{n+2})	205.368	236.338	254.304
K_c (kN/m^{n+1})	19.088	21.165	21.259
n	0.745	0.713	0.748

From Table 6, it can be concluded that the soil cohesion modulus (K_C) and the soil friction modulus (K_φ) both increase with the increase in the penetration speed of the plates. However, the n (sinkage exponent) does not change significantly. These results confirm that soil constants are related to sinkage rate. Fig. 3 shows the neural network regression diagram for the training, validation, and test

data. Our regression analysis demonstrates the effectiveness of our DNN model in predicting changes in soil deformation resulting from Bevameter penetration, aimed at better-characterizing soil parameters using the Bekker method. Figs 3. a-c depict scatter plots of predicted soil deformations against actual values for the training, validation, and testing datasets, respectively. Notably, the correlation coefficients (R) of these plots accentuate a strong linear relationship, with values of 0.9999 for training, 0.99983 for validation, and 0.99978 for testing. These high R values affirm the model's commendable performance in predicting soil deformation. It effectively converges, avoids significant overfitting, and generates unbiased predictions, as evidenced by the regression plots. This analysis emphasizes the potential of our model for accurately predicting soil deformation, with applications in soil parameter estimation using the Bekker method.

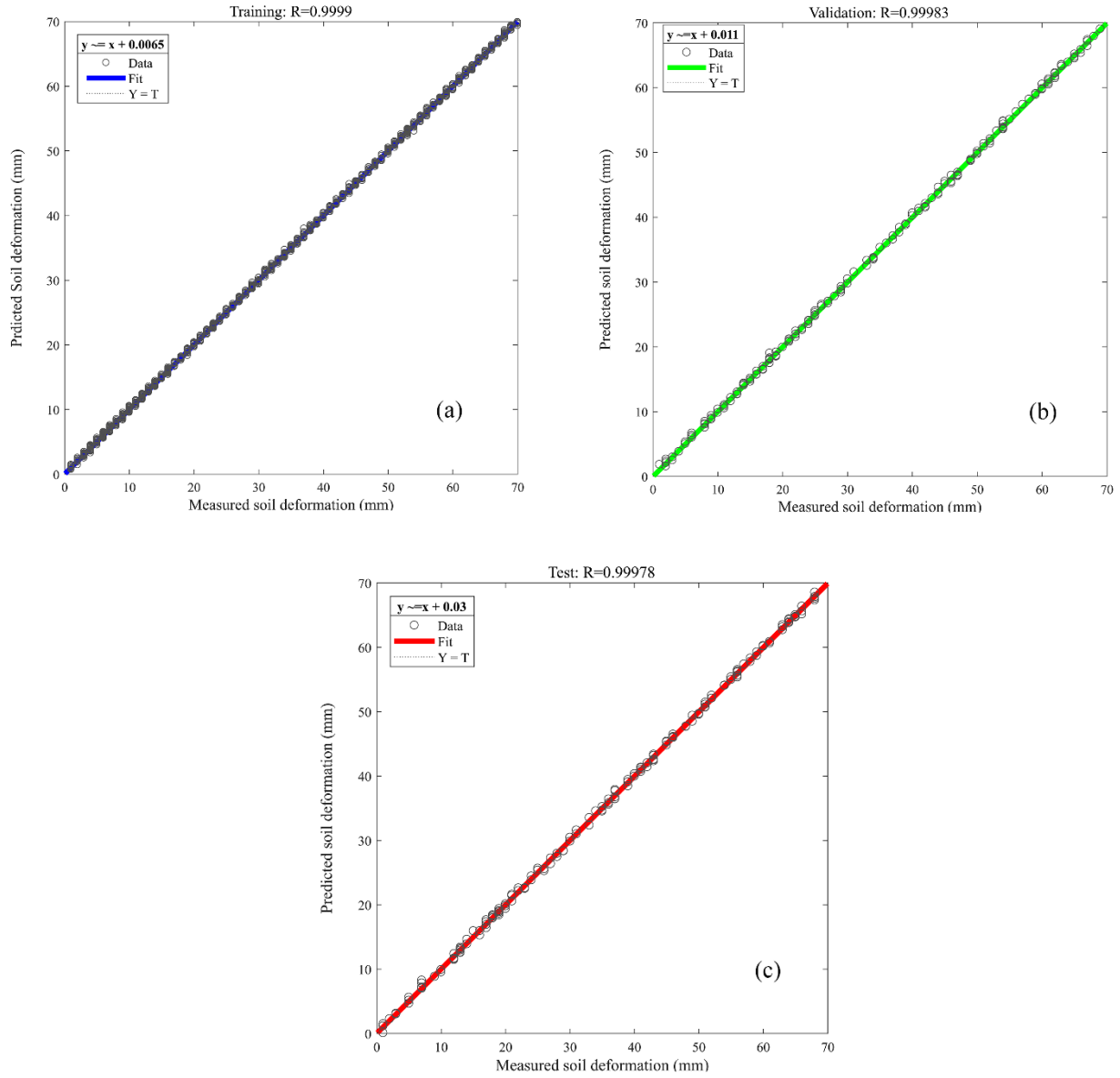

Fig.3. Regression results for neural network a. training, b. validation, and c. test data

Before starting the neural network training process, we used a cautious approach to increase the generalization capabilities of the model. We did this by randomly setting aside 15% of our data set, a common practice known as data partitioning, to serve as a validation set. By isolating a subset of the data that was not used in the model during training, we develop a measure to assess its ability to generalize beyond the examples it was exposed to during the learning phase. Essentially, the neural network was tested on this unseen data to assess its capacity to make accurate predictions beyond the scope of the training dataset. The successful results show that our model effectively learns the underlying patterns and relationships in the data without merely memorizing. Instead, it has understood the fundamental features, allowing it to generalize and make reliable predictions for new scenarios of soil deformation. This validation step is essential in any machine learning task, especially in the field of soil parameter estimation using Bekker's method. This strengthens our confidence in the model's capabilities and its potential for real-world application. Additionally, it protects the model against issues such as overfitting, where a model overfits the training data and performs poorly on new, unseen data (Fig. 4).

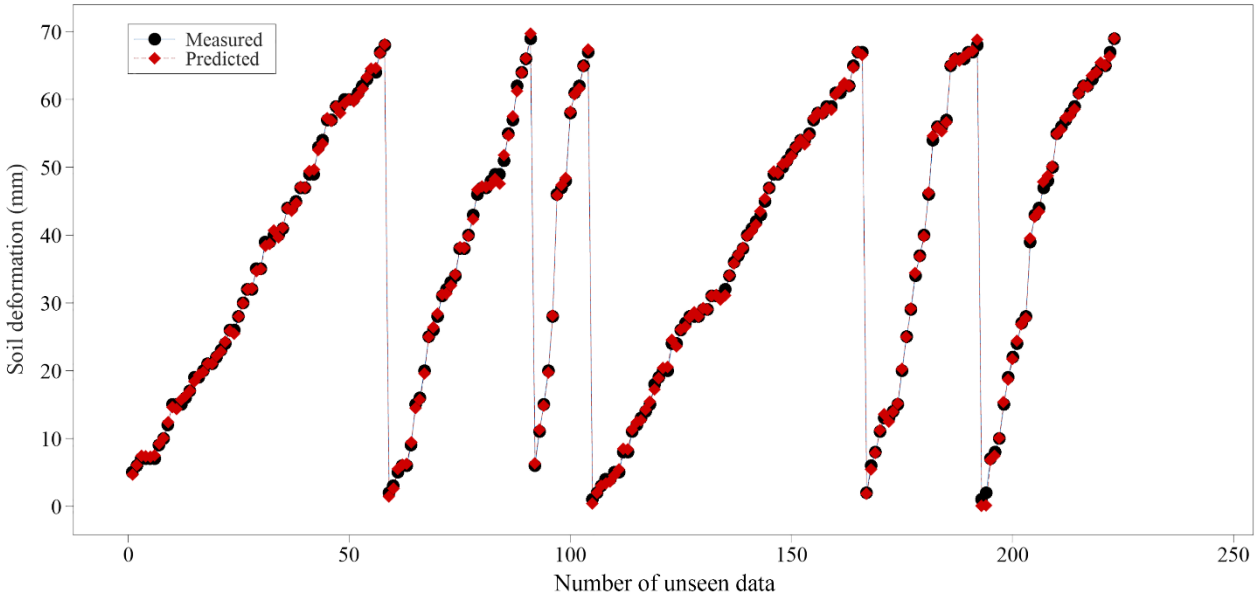

Fig.4. Trend of experimental and predicted values for soil deformation with unseen data

Figs. 5 and 6 show that sinkage increases with increased penetration velocity and pressure, for plates with 105 and 175 mm widths, respectively.

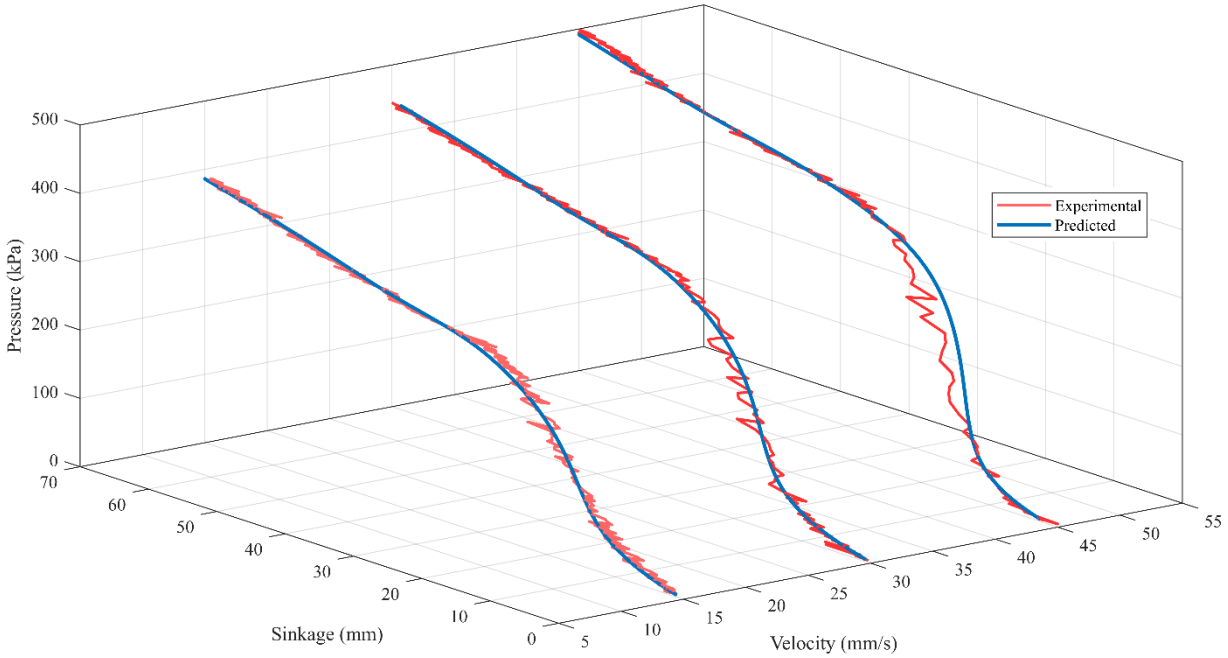

Fig.5. Pressure-sinkage diagrams for 105 × 70 (mm^2) plate size and velocities of 15, 30, and 45 mm s^{-1}

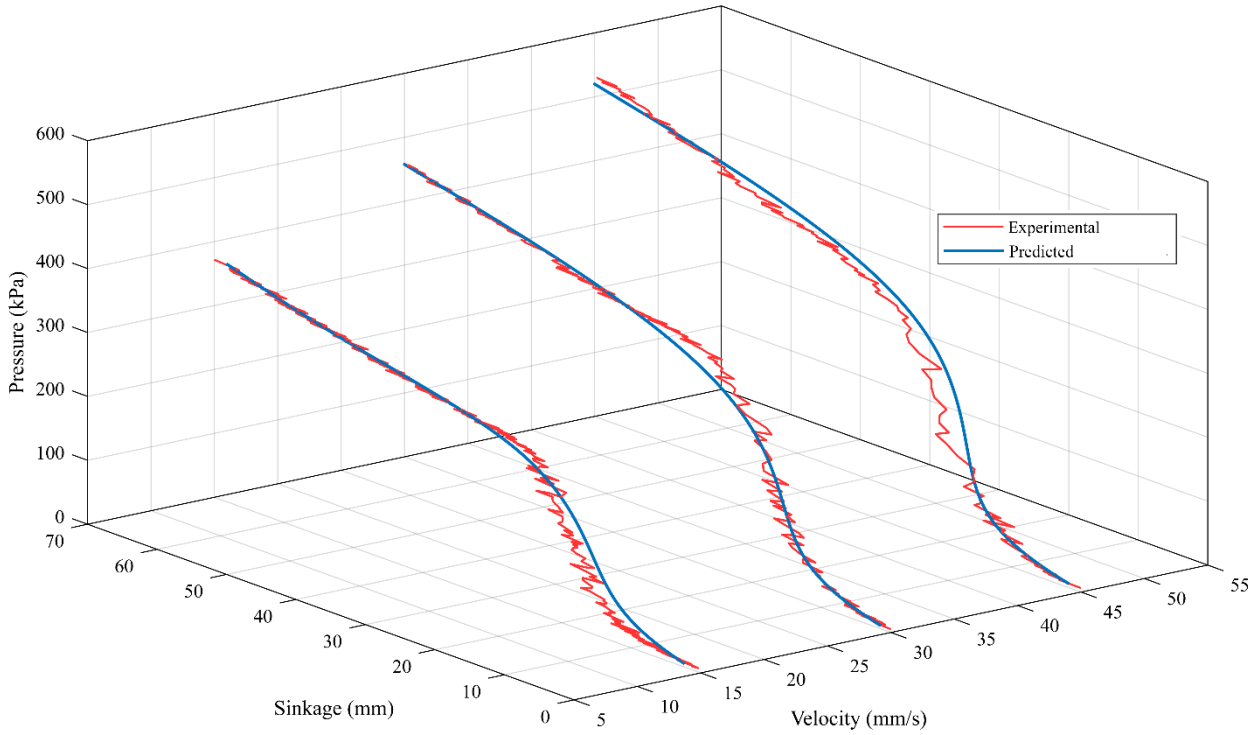

Fig.6. Pressure-sinkage diagrams for 175 × 70 (mm^2) plate size and velocities of 15, 30, and 45 mm s^{-1}

In Figs. 5 and 6, considering the trend of pressure-sinkage changes, empirical data has been utilized, and neural network-fitted (predicted) graphs have been employed. It is

observed that the neural network has been effectively trained and accurately predicts the pattern of empirical data. Furthermore, it shows that varying penetration rates result in different pressure-sinkage patterns. This notably indicates that the penetration rate plays a role in determining soil parameters. Another inference drawn from Figures 5 and 6 is that to achieve a consistent settlement after a depth of 20 to 30 millimeters, the pressure on the plates must increase with the penetration rate. Therefore, by reducing the penetration rate, a lower pressure can be applied to the plates to achieve the same depth.

In this study, three methods (Bekker model, deep neural network with hyperparameters tuning using trial and error, and deep neural network with hyperparameters determination using the Gray Wolf Optimization algorithm) were employed to determine the soil parameters at different speeds. The performance comparison of these three methods is presented in Table 7.

Table 7- Comparison of three models to estimate soil parameters

Method	MSE	RMSE
DNN-GWO	0.0837	0.2893
DNN-trial-error	1.18	1.0862
Bekker	17.30	4.1593

As it is clear from Table 7, the deep neural network achieved by adjusting the hyperparameters using the gray wolf method has performed significantly better than the other models. Using the GWO algorithm to determine the size of hidden layers in DNNs has significant advantages. It optimizes DNN architectures, which ultimately results in highly accurate models with lower mean squared error (MSE). This not only increases the predictive capability and performance of the neural network but also saves time and computational resources by automating the architecture optimization process. GWO also avoids overfitting, exploring a wide range of architectures that potentially yield superior results. Overall, GWO simplifies the process and makes DNN design more efficient and effective.

Networks trained with GWO-optimized learning rates tend to generalize better and require less manual hyperparameter tuning. Similarly, GWO's role in optimizing momentum leads to faster convergence, improved generalization, and a reduction in manual tuning efforts, ultimately streamlining neural network training and enhancing model performance.

Conclusion

To investigate the impact of factors such as the sinkage rate of plates, applied pressure on the plates, and the size of the plates on soil parameters within a soil bin, a Bevameter was employed. Experiments were conducted at three levels of penetration velocity: 15, 30, and 45 mm s^{-1}, with two plate sizes, and under dynamic loading conditions. To predict the soil sinkage with different inputs, a Multi-Layer Perceptron (MLP) deep neural network with the Backpropagation (BP) algorithm was optimized and trained using the Grey Wolf Optimization algorithm for neuron count, momentum, learning rate, and the trial and error method for learning algorithms. The optimal neural network topology had a structure of 3-8-10-15-1, consisting of three inputs and three hidden layers with the sigmoid transfer function. The development of the DNN yielded the following results:

1. A deep neural network with a structure of 3-8-15-10-1 with three inputs (sinkage rate, applied pressure on the plates, and plate size) successfully estimated sinkage with high accuracy.
2. Increasing the sinkage rate of plates resulted in higher soil modulus values.
3. A lower plate sinkage rate requires less force to reach a specific depth. In other words, for plates with fixed dimensions, to achieve the same sinkage after passing a depth of 20-30 millimeters, greater pressure on the plates is required for achieving higher plate sinkage rates.
4. The Bekker equation, in its original form, does not account for the sinkage rate parameter of the soil. Based on this research's findings, it is advisable to

consider the influence of this factor and incorporate plate sinkage rate into the equation. For achieving more accurate and realistic Bekker equation parameters, a standard sinkage rate for the plates should be considered in this context.

References

1. Bekker, M. G. (1957). Latest developments in off-the-road locomotion. *Journal of the Franklin Institute*, *263*(5), 411-423. https://doi.org/10.1016/0016-0032(57)90281-8
2. Fernandes, M. M. H., Coelho, A. P., da Silva, M. F., Bertonha, R. S., de Queiroz, R. F., Furlani, C. E. A., & Fernandes, C. (2020). Estimation of soil penetration resistance with standardized moisture using modeling by artificial neural networks. *CATENA*, *189*, 104505. https://doi.org/10.1016/j.catena.2020.104505
3. Gheshlaghi, F., & Mardani, A. (2021). Prediction of soil vertical stress under off-road tire using smoothed-particle hydrodynamics. *Journal of Terramechanics*, *95*, 7-14. https://doi.org/10.1016/j.jterra.2021.02.004
4. Haykin, S. (1999). Neural networks: a comprehensive foundation prentice-hall upper saddle river. *NJ MATH Google Scholar*.
5. He, J., Wu, D., Ma, J., Wang, H., & Li, Y. (2019). Study on the Influence Law of Loading Rate on Soil Pressure Bearing Characteristics. *Engineering Letters*, *27*(4).
6. Kruger, R., Els, P. S., & Hamersma, H. A. (2023). Experimental investigation of factors affecting the characterisation of soil strength properties using a Bevameter in-situ plate sinkage and shear test apparatus. *Journal of Terramechanics*, *109*, 45-62. https://doi.org/10.1016/j.jterra.2023.06.002
7. Mahboub Yangeje, H., & mardani Korani, A. (2021). Design and Fabrication of a Bevameter for Measuring the Soil Deformation Details. *Iranian Journal of Biosystems Engineering*, *52*(3), 487-498. https://doi.org/10.22059/ijbse.2021.318526.665385
8. Pham, B. T., Nguyen, M. D., Bui, K. T. T., Prakash, I., Chapi, K., & Bui, D. T. (2019). A novel artificial intelligence approach based on Multi-layer Perceptron Neural Network and Biogeography-based Optimization for predicting coefficient of consolidation of soil. *CATENA*, *173*, 302-311. https://doi.org/10.1016/j.catena.2018.10.004
9. Pieczarka, K., Pentoś, K., Lejman, K., & Owsiak, Z. (2018). The use of artificial intelligence methods for optimization of tractive properties on Silty Clay Loam. *Journal of Research and Applications in Agricultural Engineering*, *63*(1).
10. Roul, A. K., Raheman, H., Pansare, M. S., & Machavaram, R. (2009). Predicting the draught requirement of tillage implements in sandy clay loam soil using an artificial neural network. *Biosystems Engineering*, *104*(4), 476-485. https://doi.org/10.1016/j.biosystemseng.2009.09.004
11. Taghavifar, H., & Mardani, A. (2014a). Effect of velocity, wheel load and multipass on soil compaction. *Journal of the Saudi Society of Agricultural Sciences*, *13*(1), 57-66. https://doi.org/10.1016/j.jssas.2013.01.004
12. Taghavifar, H., & Mardani, A. (2014b). Prognostication of vertical stress transmission in soil profile by adaptive neuro-fuzzy inference system based modeling approach. *Measurement*, *50*, 152-159. https://doi.org/10.1016/j.measurement.2013.12.035
13. Taghavifar, H., Mardani, A., & Hosseinloo, A. H. (2015). Appraisal of artificial neural network-genetic algorithm based model for prediction of the power provided by the agricultural tractors. *Energy*, *93*, 1704-1710. https://doi.org/10.1016/j.energy.2015.10.066
14. Taghavifar, H., Mardani, A., Karim-Maslak, H., & Kalbkhani, H. (2013). Artificial Neural Network estimation of wheel rolling resistance in clay loam soil. *Applied Soft Computing*, *13*(8), 3544-3551.
15. Van, N. N., Matsuo, T., Koumoto, T., & Inaba, S. (2008). Experimental device for measuring sandy soil sinkage parameters. *Bulletin of the Faculty of Agriculture Saga University*, *93*(1),

91-99.
16. Wong, J. Y. (2010). Chapter 2 - Modelling of Terrain Behaviour. In J. Y. Wong (Ed.), *Terramechanics and Off-Road Vehicle Engineering (Second Edition)* (Second Edi, pp. 21-63). Butterworth-Heinemann. https://doi.org/10.1016/B978-0-7506-8561-0.00002-6
17. Zhang, Z. X., & Kushwaha, R. L. (1999). Applications of neural networks to simulate soil-tool interaction and soil behavior. *Canadian Agricultural Engineering*, *41*(2), 119.

نشریه ماشین‌های کشاورزی
https://jame.um.ac.ir

مقاله پژوهشی

جلد ۱٤، شماره ۱، بهار ۱٤۰۳، ص ۸۲-٦۹

مدل‌سازی فشار- نشست خاک تحت تأثیر سرعت نشست با استفاده از یادگیری عمیق بهینه‌سازی‌شده توسط الگوریتم گرگ خاکستری

بهزاد گلعنبری[۱]، عارف مردانی کرانی[۱*]، عادل حسین پور[۱]، حمید تقوی فر[۲]

تاریخ دریافت: ۱۴۰۲/۰۶/۱۸
تاریخ پذیرش: ۱۴۰۲/۰۸/۱۳

چکیده

با توجه به متغیرهای متعددی که بر سیستم‌های اندرکنش خاک و ماشین تأثیرگذار هستند، پیش‌بینی پاسخ مکانیکی خاک در تعامل با دستگاه‌های کششی خارج از جاده چالش برانگیز است. در این مطالعه، شبکه‌های عصبی عمیق به دلیل توانایی آن‌ها در مدل‌سازی سیستم‌های پیچیده، چندمتغیره و دینامیک به‌عنوان یک راه‌حل بالقوه برای توضیح میزان فرورفتگی خاک در نرخ‌های مختلف از بار عمودی انتخاب شد. آزمایش‌های فشار-نشست خاک با استفاده از بوامتر در یک انباره خاک از نوع ثابت با طول ۲۴ متر، عرض ۲ متر و کانال خاک عمق ۱ متر انجام شد. آزمایش‌های تجربی در سه سطح سرعت نشست، دو سطح اندازه صفحه، در محتوای آب خاک ۱۰ درصد انجام شد که داده‌های تجربی در مورد روابط فشار و نشست خاک ارائه می‌کرد. این آزمایش‌ها به‌عنوان مبنایی برای الگوریتمی بود که قادر به تشخیص تعامل بین خاک ماشین پس از یک فرآیند تکراری دقیق بود. مشخص شد که یک شبکه عصبی عمیق، به‌ویژه یک شبکه عصبی عمیق با انتشار پیش‌خور با سه لایه پنهان، انتخاب بهینه برای این منظور است. معماری شبکه عصبی عمیق بهینه‌شده به‌صورت ۱-۱۰-۱۵-۸-۳ شکل یافت که توسط الگوریتم بهینه‌سازی گرگ خاکستری تعیین شده است. در حالی‌که معادله بکر به‌طور سنتی به‌عنوان یک روش پذیرفته‌شده برای پیش‌بینی رفتار فشار- نشست خاک استفاده می‌شود، تأثیر سرعت نشست در خاک را نادیده می‌گرفت. با این حال، یافته‌های تحقیق تأثیر قابل‌توجهی از سرعت نشست بر پارامترهای حاکم بر پاسخ تغییر شکل خاک را نشان داد. شبکه عصبی عمیق آموزش‌دیده با موفقیت سرعت نشست را در ساختار خود گنجاند و نتایج دقیقی با مقدار میانگین مربعات خطای ۰/۰۸۷۱ ارائه کرد.

واژه‌های کلیدی: انباره خاک، بوامتر، ترامکانیک، شبکه عصبی عمیق، وسیله نقلیه خارج از جاده

۱- گروه مکانیک بیوسیستم دانشگاه ارومیه، ارومیه، ایران
۲- گروه مهندسی مکانیک، صنایع و هوافضا، دانشگاه کنکوردیا، کنکوردیا، کانادا
(*- نویسنده مسئول: Email: a.mardani@urmia.ac.ir)

https://doi.org/10.22067/jam.2023.84339.1188

Journal of Agricultural Machinery

Homepage: https://jame.um.ac.ir

Review Article
Vol. 14, No. 1, Spring 2024, p. 83-104

Cold Plasma Technique in Controlling Contamination and Improving the Physiological Processes of Cereal Grains (a Review)

M. Pourbagher[1], R. Pourbagher[2], M. H. Abbaspour-Fard[3*]

1- Bachelor's Degree, Department of Computer Engineering, Faculty of Engineering, Golestan Institute of Higher Education, Gorgan, Iran
2- PhD Graduate, Department of Biosystems Engineering, Faculty of Agriculture, Ferdowsi University of Mashhad, Mashhad, Iran
3- Professor, Department of Biosystems Engineering, Faculty of Agriculture, Ferdowsi University of Mashhad, Mashhad, Iran
(*- Corresponding Author Email: abaspour@um.ac.ir)

Received: 30 September 2023
Revised: 24 October 2023
Accepted: 01 November 2023
Available Online: 01 November 2023

How to cite this article:
Pourbagher, M., Pourbagher, R., & Abbaspour-Fard, M. H. (2024). Cold Plasma Technique in Controlling Contamination and Improving the Physiological Processes of Cereal Grains. *Journal of Agricultural Machinery*, *14*(1), 83-104. https://doi.org/10.22067/jam.2023.84647.1193

Abstract

Today, almost half of the total human food, especially in Asia, is directly supplied from grains, and nearly 70% of the cultivated area of the world, which is one billion hectares, is used for growing grains. Therefore, non-destructive methods must be found and developed to increase seed quality in agriculture and industry. Cold plasma is a novel and efficient method that can be used in the agricultural and food sectors for the inactivation of surface microorganisms and the excitation of seeds. This review presents a summary of the effectiveness of cold plasma treatment on the characteristics of four important cereal plants: wheat, rice, corn, and barley. The focus is on the effects of this treatment on seed germination, surface property changes, water uptake of seeds, growth parameters of root, shoot, and seedling length, biomass parameters, and metabolic activities. By examining the research conducted by the researchers, it can be seen that the cereal seeds treated with cold plasma had better germination power, water absorption, shoot length, growth efficiency, shoot and root weight, and metabolic activity. This review can provide insight into the promising trends in utilizing plasma as a method to decrease the prevalence of harmful plant diseases transmitted through seeds and reduce the dormancy of hard seeds.

Keywords: Biological feature, Cereal grain, Cold plasma, Seed treatment

Introduction

Cold atmospheric plasma, has gained significant popularity in recent years. In the last few years, cold plasma has been extensively used in agriculture or plant biological applications including cultivation, surface sterilization, seed germination, pretreatment before drying, modification of surface properties, decontamination of seeds, and disease control (Liao *et al.*, 2020).

The use of different plasma devices has enabled extensive research on the plasma treatment of seeds. These devices facilitate in-depth investigations into the physical, chemical, and biological processes triggered by plasma components (Maghsoudi, Balvardi, Ganjovi, & Amir-Mojahedi, 2023; Ranieri *et al.*, 2021). There are two methods for plasma treatment of seeds, namely direct and indirect, which are determined by the interaction between the plasma and the samples (Gómez-Ramírez *et al.*, 2017). In the indirect treatment method, the treated surface is placed at a distance from the plasma production point, and

https://doi.org/10.22067/jam.2023.84647.1193

the produced plasma is transferred to the sample surface through the fed gas flow. This system produces UV and chemical species with longer life and less reactivity. In the direct treatment method, the treated product is positioned relatively close to the plasma production point. This method produces a higher concentration of reactive species. At high voltages, it induces electrical conductivity in products with high internal moisture content and water activity. Local heating in this system can cause sensory damage such as burn symptoms or protein coagulation, as well as changes in aroma, texture, and appearance (Niemira, 2012).

Cold plasma can be readily produced through different types of electric discharges. The most frequently utilized methods include dielectric barrier discharges (DBD), plasma jets, corona discharges, gliding arcs, and microwave discharges (Adhikari *et al.*, 2020). All of these produced plasmas are non-thermal, meaning that the discharge occurs at atmospheric temperature and pressure. The jet, corona, gliding arcs, and microwave discharges can treat the surfaces of large objects and are also useful for improving the adhesion of materials in industrial processing (Kusano *et al.*, 2014). The mild operating conditions and low temperature, along with the flexible reactor shape and the ability to use gas mixtures of DBD plasma, make it an attractive option for modifying temperature-sensitive surfaces, particularly agricultural products (Fang, Wang, Shao, Qiu, & Edmund, 2011). The seeds and seedlings can also be soaked or watered using plasma-activated water (PAW), which is made by exposing liquids to plasma. Similar effects on macroscopic plant properties have been observed when comparing the use of gaseous and aqueous treatments (Sajib *et al.*, 2020; Sivachandiran & Khacef, 2017).

Cereals are a type of monocotyledonous herbaceous plant with small edible seeds. In many Asian and African countries, grains provide more than 80% of people's food. The share of cereals in the food of European people is 45-55% and in the United States, it is approximately 20-30%. Wheat, rice, and corn are the three most important crops, each accounting for roughly a quarter of the annual grain production. To feed the projected global population of 9.8 billion people by 2050, the supply of cereals must be increased by 70-100% (Godfray *et al.*, 2010).

Increasing production rates are commonly seen as the answer to meet the growing demand. However, historical data indicate that the current production rates fall short of what is needed to achieve the targets (Ray, Mueller, West, & Foley, 2013). On the other hand, desertification and adverse climatic and agricultural conditions such as drought and salt are spreading rapidly across arable lands. Therefore, to improve crop yield, researchers are trying to find suitable methods to break seed dormancy and increase the percentage and speed of seed germination, and also to find cultivars that are more resistant to drought, salinity, and disease (Radjabian, Saboora, Hhasani, & Fallah-Hosseini, 2007).

The objective of this review is to present a summary of the extensive knowledge acquired by researchers in studying the impact of cold plasma on plant seeds, which is rapidly expanding. We chose the seeds of cereal plants because their presence in the diet is essential and could ensure food security. Given the increasing attention to plasma treatment in agriculture, it is valuable to provide an overview of the hypotheses and current evidence on the impact of plasma treatments on cereal seeds. The main objectives of our review are summarized in Fig. 1.

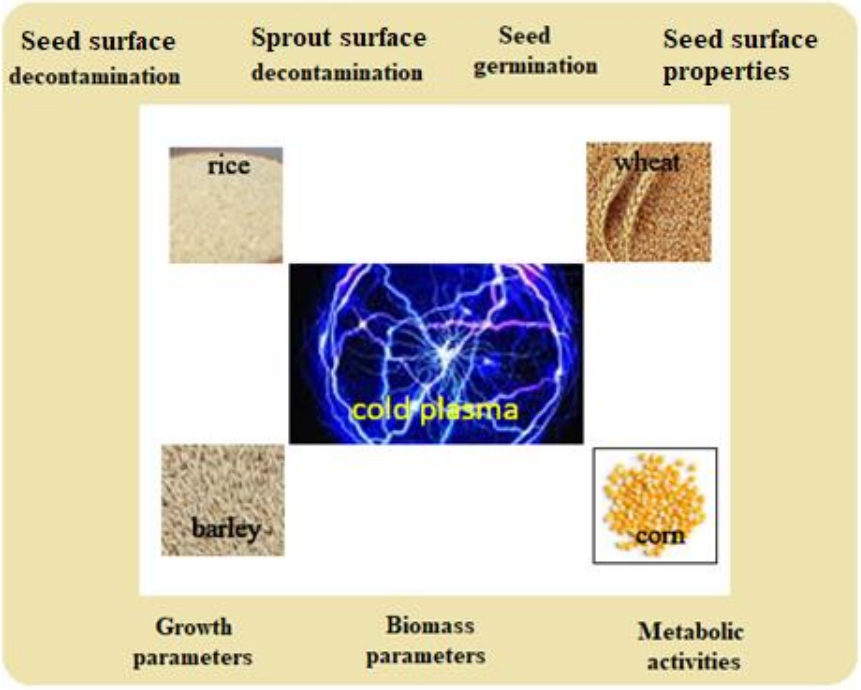

Fig.1. Schematic overview of the effects of cold plasma on cereal grains

Seed and sprout decontamination

Promising results have been reported by researchers in the use of cold plasma for decontaminating seed surfaces and plant sprouts from microbes and toxins. In a study conducted by Butscher *et al.* (2015), it was found that *Bacillus amyloliquefaciens* bacteria on wheat seeds could be effectively deactivated using this method. This was achieved by exposing the seeds to low-pressure Ar/O_2 DBD plasma at radio frequencies ranging from 8.0 to 12.8 mbar, and with power levels between 700 and 900 W for a duration of 30 s. In a study conducted by Filatova *et al.* (2014), the effectiveness of low-pressure air plasma at a frequency of 5.28 MHz for 2-10 minutes in eliminating phytopathogens from contaminated wheat seeds was demonstrated. The most favorable outcome was a 77% reduction in infection rate with a 5-minute exposure, while germination levels remained unchanged. Kabir *et al.* (2019) reported that Ar/Air and Ar/O_2 DBD plasma at a pressure of 10 torrs and 4.5 kHz frequency for 90 s led to the detoxification of cadmium in wheat. Selcuk, Oksuz, and Basaran (2008) demonstrated that treatment of seeds with air plasma generated in a vacuum chamber with frequency of 1 kHz and voltage of 20 kV for 5-20 minutes could effectively decrease the presence of two types of filamentous fungi, namely *Aspergillus* spp. and *Penicillium* spp., on the surface of corn and wheat seeds. The researchers found that a notable reduction of 3-log could be achieved with just 15 minutes of plasma treatment.

The positive impact of atmospheric pressure plasma treatment, like low-pressure plasma, was linked to its ability to effectively deactivate pathogens on the surface of cereal seeds. Plasma was able to deactivate the microorganisms on the germinated seeds based on the discharge of the DBD (Fereydooni & Alizadeh, 2022). The mechanism of inactivation is related to the intracellular accumulation of reactive oxygen species, which causes the rupture of the outer membrane of the bacterial cell, disruption of protein activity, removal of the cytoplasm from the cell, and finally the death of the bacterial cell (Mendis, Rosenberg, & Azam, 2000). Butscher, Zimmermann, Schuppler, and

von Rohr (2016) conducted a study to investigate the impact of atmospheric pressure on the deactivation of bacterial cells in wheat seeds using argon plasma. They utilized DBD plasma at pulse voltage (6-10 kV) and pulse frequency (5-15 kHz) for this purpose. The results revealed that a 5-minute plasma treatment led to a 1-log reduction in the number of bacteria, whereas a 60-minute exposure resulted in a more significant 3-log reduction. In a study by Zahoranová *et al.* (2016), it was shown that applying coplanar surface barrier discharge at atmospheric pressure for 120 s, with a frequency of 14 kHz and voltage of 20 kV, led to a significant reduction in the initial natural bacterial load on artificially contaminated wheat seeds. The bacterial load, initially measured at 5.52× 104 CFU/g, was reduced by 1 log. In addition, different effects of cold plasma treatment on the inactivation of fungi samples of *Fusarium nivale, F. culmorum, Trichothecium roseum, Aspergillus flavus, and A. clavatus were reported*. In a study conducted by Shi, Ileleji, Stroshine, Keener, and Jensen (2017), it was discovered that treating corn with DBD atmospheric pressure plasma using two gases, air, and MA65, resulted in a noteworthy decrease in aflatoxin levels. In their study, the plasma system was operated at 200 W and 50 HZ generating 90 kV. The degradation of aflatoxin in corn reached 62% and 82% after 1 and 10 minutes of HVACP treatment in RH 40% air, respectively. Moreover, the application of cold atmospheric plasma had a notable effect on the reduction of Deoxynivalenol (a prominent mycotoxin found in grains) in barley seeds. The outcomes demonstrated that the treatment of cold atmospheric plasma for 6 and 10 minutes resulted in a decrease in Deoxynivalenol concentration by 48.9% and 54.4%, respectively (Feizollahi, Iqdiam, Vasanthan, Thilakarathna, & Roopesh, 2020). It is assumed that various degradation mechanisms, including chemical reactions with reactive species generated in cold plasma (such as O_3, O, OH, NO_x), decomposition after collision with electrons and ions, and UV light are responsible for breaking down toxin molecules through cold plasma treatment (Ten Bosch *et al.*, 2017). The cold plasma system's performance can be increased to further reduce Deoxynivalenol by adjusting various process factors such as voltage and frequency, type of feed gas, relative air humidity, etc.

Los *et al.* (2018) conducted a study on the decontamination of various bacteria species (*E. coli* NCTC and *B. atrophaeus*) and fungi *P. verrucosum* DSM. Their research revealed that treatment 20 minutes of treatment of DBD plasma at 80 kV voltage showed promise in controlling both native microflora and pathogenic microorganisms on the wheat and barley seeds. DBD air plasma also resulted in a significant decrease in the initial concentration of pathogenic bacteria (*Bacillus cereus*, *B. subtilis*, and *E. coli* O157:H7) inoculated on brown rice, reducing it from 8 log CFU/mL to an undetectable level (2.3 log CFU/g) within 20 minutes (Lee *et al.*, 2016). Lee *et al.* (2018) also found similar outcomes with brown and white cooked rice. They observed reductions of 2.01-log in *Bacillus cereus* and *Escherichia coli* bacteria after subjecting the rice to 20 minutes of treatment with air plasma (250 W, 15 kHz).

Seed germination

Seed germination, as an essential factor for the survival of plant species, starts with water absorption, stimulating physiological activities that eventually result in ending the seed's dormancy (Nonogaki, 2014). Several studies have been conducted in agriculture to explore techniques for enhancing seed germination, ultimately improving crop growth and yield. Seed priming causes biological and physiological changes in both the seed and plant, which results in better germination and proper seedling establishment (Lutts *et al.*, 2016; Zulfiqar, 2021). There are many seed priming techniques including halo, hydro, osmose, hormonal, chemical, physical, and biological priming (Ali *et al.*, 2017). Recently, cold plasma seed treatment has gained attention as a physicochemical priming technology, especially for cereal crops

(Adhikari *et al.*, 2020). ROS and RNS present in plasma have a wide range of regulatory functions involved in various processes of plant growth and development, including germination, metabolism, signal transduction, nutrient uptake, improvement of seedling growth, and abiotic/biotic stress tolerance (Yong *et al.*, 2019). Treating seeds with plasma by changing the shape of the seed coat and inducing seed germination reduces germination time, enhances disease resistance, and accelerates growth and development (Nalwa, Thakur, Vikram, Rane, & Vaid, 2017; Rasooli, Barzin, Mahabadi, & Entezari, 2021).

So far, much research have been carried out on the effect of cold plasma treatment on the germination of cereal seeds. According to a study conducted by Yodpitak *et al.* (2019), it was discovered that subjecting brown rice to DBD argon plasma stimulation for 75 s resulted in a notable increase (84%) in germination rate. A study carried out by Amnuaysin, Korakotchakorn, Chittapun, and Poolyarat (2018) found that subjecting rice seeds to DBD air plasma treatment for 60 s led to a significant improvement in both vigor index and germination speed. Chen *et al.* (2016) discovered similar outcomes whereby the germination speed and early vigor of brown rice seedlings were enhanced following a 10-minute treatment of low-pressure plasma exposure. They attributed this enhancement to the increased a-amylase activity. Penado, Mahinay, and Culaba (2017) investigated the effects of atmospheric air plasma jet treatment on the germination of rice (*Oryza sativa* L.). They observed that plasma treatment led to a decrease in trichomes on the seed's surface. This could potentially enhance the seed's ability to absorb water, resulting in a significant change in seed germ length. However, the treatment did not affect the overall germination count of the seeds after the 72-h germination period.

Velichko *et al.* (2019) treated wheat seeds with atmospheric pressure plasma from a jet and dielectric barrier discharge operating in argon gas for 15 to 300 s. The plasma jet treatment resulted in a slight increase in germination, with the treated samples showing a germination rate of 98.7% compared to the control samples' rate of 97.0%. The average time it took for germination to occur decreased from 3.90 days for the control samples to 3.67 days for the treated ones. Notably, the germination time decreased significantly when the treatment time exceeded 60 seconds. The speed of germination begins to decline after treatment times exceed 30 seconds. This decline can be attributed to the influence of the hot argon stream, which reaches a temperature of 103 $^{\circ}$C. In contrast, when using atmospheric pressure DBD, this effect is minimal, and the growth properties of the seeds are solely impacted by the active species produced by the discharge. By examining the effect of plasma treatment on wheat seeds with two types of operating gases, air, and SF_6, Selcuk *et al.* (2008) showed that the germination rate of wheat seeds treated with plasma was not greatly affected. In addition, there was no noticeable variation in the germination rate among seeds that were exposed to air and SF_6 plasma gases for 5, 10, or 15 minutes. Similarly, by investigating the effect of surface discharge plasma on wheat seeds, Dobrin, Magureanu, Mandache, and Ionita (2015) reported that germination was less affected by treatment compared to growth parameters.

PAW can impact water consumption during the germination phase and lead to the production of hybrid cereal seeds with superior germination rates. In a study conducted by Chalise *et al.* (2023), the effectiveness of PAW created by gliding discharge plasma was examined concerning wheat seed germination. The findings indicated that a treatment duration of 15 minutes resulted in improved germination rates and a higher yield of wheat products. Similarly, in a study conducted by Chalise *et al.* (2023), the effectiveness of PAW created through gliding discharge plasma was examined in relation to wheat seed germination. The findings indicated that a treatment duration of 15 minutes resulted in improved germination rates and a higher yield of wheat products. Similarly, a study conducted by Wang, Cheng, and Sun (2023)

demonstrated the positive effects of treating wheat seeds with PAW generated by an atmospheric pressure Ar-O_2 plasma jet. The researchers found that a treatment duration of 3 minutes with PAW resulted in enhanced germination, vigor index, and seedling growth. Ahn, Gill, and Ruzic (2019) also proved that corn seeds hybridized with PAW can have a germination rate of nearly 100%. Kabir *et al.* (2019) discovered that the harmful effects of Cadmium on cellular and protein features were significantly reduced by treating wheat seeds with Ar/O_2 and Ar/Air plasma before germination. Therefore, plasma treatment may also contribute to the decreased uptake and movement of Cadmium in wheat plants whose seeds were previously treated by plasma. Guo *et al.* (2017) demonstrated that treating wheat seeds with DBD plasma for 4 minutes led to an impressive 27.2% increase in germination potential and a corresponding 27.6% boost in the germination rate. The research also demonstrated that plasma treatment had a positive effect on reducing damage caused by membrane lipid peroxidation. This was achieved by enhancing the activities of antioxidant enzymes such as superoxide dismutase, catalase, and peroxidase, which indicated an improved tolerance to environmental stress. Additionally, plasma treatment was found to promote the generation of abscisic acid in wheat seedlings. Hui *et al.* (2020) attributed the increase in wheat seed germination to the significant effect of active species produced by plasma on secondary metabolism during seed germination. They identified the buildup of charges caused by plasma-charged particles on the cell membrane's surface, the creation of electrostatic force, and the resulting harm to the cell membrane as the cause for enhanced permeability of the cell membrane and seed coat. This phenomenon speeds up the absorption of water and nutrients, ultimately bolstering seed germination.

Other researchers, including Jiang *et al.* (2014); Li *et al.* (2017); Los, Ziuzina, Boehm, Cullen, and Bourke (2019); Meng *et al.* (2017); Roy, Hasan, Talukder, Hossain, and Chowdhury (2018), mentioned the increase in the germination and growth of wheat seeds treated with atmospheric pressure plasma. Starič *et al.* (2022) employed both direct and indirect treatment methods to examine the germination process of wheat seeds. They generated plasma using glow and afterglow discharge techniques, with oxygen feed gas, under low-pressure conditions. Their findings indicated that plasma treatment had no significant impact on the germination rate, except for the seeds treated under 90 s which experienced a notable decrease in germination rate and root growth due to the change in the morphology of wheat grain pericarp. In another study, Sidik *et al.* (2018) investigated the effect of helium gas-fed jet plasma on corn seeds. The research demonstrated that when the seeds underwent a 3-minute treatment, they exhibited a higher germination speed and improved growth compared to the untreated seeds. However, it is worth noting that the germination rate for both treated and untreated seeds was 86%. In a study conducted by Feizollahi *et al.* (2020), barley grains were subjected to DBD plasma in humid air. The study revealed that treating the grains for either 1 or 10 minutes resulted in a reduction in root length, root surface area, shoot length, and the number of roots, compared to the untreated control group. Interestingly, a 6-minute treatment improved these parameters significantly, with seeds exposed to 6 minutes of plasma radiation exhibiting the highest germination percentage at 93.3%. In general, based on the conducted studies by Park *et al.* (2018), it has been found that cold plasma treatment can generally affect the rate of seed germination. This is achieved by altering seed water absorption, seed surface characteristics, and biological reactions within the seeds, as well as protein structure, and internal functional metabolites like gamma-aminobutyric acid.

Surface property changes and water uptake of seeds

The absorption of water by seeds is dependent on three primary factors: the seed's

composition, the permeability of its coat, and water availability (McDonald, 1994). So far, cold plasma technology has shown positive effects on both the surface characteristics and internal content of grains. The plasma treatment enhances water absorption in seeds by reducing surface energy. The seed's hydrophilicity, or its ability to absorb water, is determined by measuring the contact angle formed by a water drop. The study conducted by Chen *et al.* (2016) demonstrated that exposing brown rice to plasma resulted in increased water uptake compared to untreated brown rice. The maximum level of water uptake was observed to be 30.2% in samples that were exposed to 3 kV air plasma for 10 minutes after a germination period of 24 h. Lee *et al.* (2016) found that plasma-treated brown rice exhibited higher water absorption than regular brown rice for all soaking durations. The maximum water uptake reached 24.78% and was observed after 5 h of soaking. The increase in water uptake ratio was associated with a decrease in cooking time. The plasma treatment altered the microstructure of the rice bran layers, making it easier for water to penetrate the brown rice kernel (Chen, Chen, & Chang, 2012). Increasing the time of plasma treatment showed more effectiveness on the seeds and as a result, reduced the cooking time. In addition, the hardness of cold plasma-treated rice was significantly lower than untreated brown rice.

Tissue changes in parboiled rice under low-pressure cold plasma were analyzed by Sarangapani, Devi, Thirundas, Annapure, and Deshmukh (2015). They observed significant alterations in the surface morphology. Following the treatment, the grain's surface exhibited cracks and indentations known as "surface etching." Plasma treatment altered the grains' natural surface structure, leading to modifications in cooking and textural characteristics. The treatment of 50 W for 15 minutes induced more etching, resulting in shorter cooking time, decreased contact angle, increased water uptake ratio, and higher surface energy. Similar results were presented by Chen *et al.* (2012) who investigated the properties of the surface, cooking, texture, and iodine staining of brown rice. Their results revealed that plasma treatment causes the surface of brown rice to be etched, enabling the rice kernel to absorb water more easily during soaking. As a result of this treatment, the cooking time for brown rice is shortened, the iodine-stained area is increased, and the cooked rice has a tender texture and is more enjoyable to eat. In a study conducted by Liu, Wang, Chen, and Li (2021), it was found that subjecting milled rice to a 120 W helium plasma treatment for 20 s resulted in improved cooking properties of milled rice. This was achieved by creating a rough kernel surface, increasing the water absorption rate, weakening the protein network, and speeding up starch gelatinization. Thirumdas, Deshmukh, and Annapure (2015) analyzed the effect of air plasma at a pressure of 0.15 mbar on the water absorption and cooking time of basmati rice. The water absorption was found to be directly related to the power and time of plasma treatment, which is likely associated with the reduction of cooking time and the modification of the grain surface. The shorter cooking time of plasma-treated rice can be explained by the fragmentation of starch, the opening up of the kernel structure, and the degradation of other components. These changes allow the rice kernel to absorb more water, leading to a reduction in cooking time (Sabularse, Liuzzo, Rao, & Grodner, 1991).

Velichko *et al.* (2019) conducted a study on the surface modification and chemical structures of wheat seed coats using jet and DBD plasma treatment. They observed that the water imbibition capacity of wheat seeds increased by 20-30% after being exposed to plasma radiation for 15-30 s. This enhancement in water imbibition can be attributed to the increased hydrophilicity of the seed surface, leading to a decrease in the apparent contact angle. Bormashenko, Grynyov, Bormashenko, and Drori (2012) observed a significant change in the wettability of wheat seeds, where the contact angle decreased from 115 ° to zero. Interestingly, the amount of water absorption did not change

significantly and only the treated seeds experienced a slight increase in water absorption. The results were attributed to the oxidation of the grain surface by plasma. Sera, Spatenka, Šerý, Vrchotova, and Hruskova (2010) visually observed that plasma-treated wheat seeds at a pressure of 140 Pa exhibited quicker wetting compared to the control seeds. However, they did not provide quantitative measurements of water imbibition. In another study, Starič *et al.* (2022) investigated the changes in the morphology of the seed pericarp and the chemical characteristics of the wheat grain surface treated with plasma through SEM and AFM. The seed pericarp's morphology was changed and its roughness increased as a result of extended direct plasma treatment. The extent of functionalization was more noticeable in direct compared to indirect treatment.

The alteration in seed wettability was found to be related to the oxidation of lipid layers and the functionalization of the seed surface. Zahoranová *et al.* (2016) also reported that the water uptake in wheat seeds increased with higher exposure doses of plasma. After a 2-hour treatment with coplanar surface DBD, the water uptake ranged from 6.41 to 9.60 mg, and after 8 hours it ranged from 12.53 to 16.07 mg per seed, compared to the control. The water absorbed by the plasma-treated seeds triggers the hydrolytic amylase enzyme, helping the metabolic process by breaking down the stored starch and protein in seeds (Kikuchi, Koizumi, Ishida, & Kano, 2006). Treatment of cereal seeds with PAW also improves the surface characteristics. Chalise *et al.* (2023) reported the wettability and contact angle of wheat seeds increased and decreased significantly after being treated with PAW for 15 minutes, respectively. The increase in wettability is believed to be due to the presence of ultraviolet light and OH radicals, which are the main components of atmospheric plasma.

Growth parameters (root, shoot, and seedling length)

The parameters of root growth play a crucial role in effectively utilizing the soil and absorbing minerals, particularly for nutrients that have limited mobility. The growth of roots has a significant impact on the development of strong shoots and the overall yield of crops, particularly in soils with low nutrient levels (Wang, Thorup-Kristensen, Jensen, & Magid, 2016). The growth of roots can be influenced by cold plasma treatment, thereby altering the plants' capacity to explore soil and absorb water and nutrients (Pérez-Pizá *et al.*, 2020). The impact of cold plasma and PAW on the growth parameters is closely connected to the effects mentioned earlier regarding germination. Yodpitak *et al.* (2019) reported an increase in the height of seedlings and root growth of brown rice after 75 s of argon plasma exposure to 69% and 57% compared to the control, respectively. Additionally, the root length and seedling height decreased when the treatment time exceeded 75-100 s for all rice cultivars. The enhancement of seedling growth attributes of rice seed, such as shoot length and the contents of photosynthetic pigments of seedlings as a result of being treated with plasma for 10 s was also reported by Amnuaysin *et al.* (2018). The increase in seed permeability can be related to the improvement of nutrient absorption capacity, which potentially facilitates the growth of the seedlings. A study by Chen *et al.* (2016) determined that low-pressure plasma increased the length of brown rice seedlings by 37% compared to the control. However, there were no significant differences between the samples treated with plasma and the control group, as per the statistical analysis. For the rice variety *Oryza sativa* L., Penado *et al.* (2017) reported an improvement in the growth process of samples treated with air plasma jet considering the effect on the increase in the length of the seed shoot, which is related to the speed of seed root expansion. In another study, Liu *et al.* (2021) did not observe significant changes in the ratio of grain length to width by researching the effect of radio frequency helium plasma treatment for 20-120 s on Chinese milled rice.

The advantageous effects of using short treatment times (ranging from 4 to 7 minutes)

of surface DBD in air, nitrogen, and argon were observed in terms of the germination rate, water absorption, and lengths of roots and shoots of wheat. Conversely, prolonged exposure had detrimental effects on the seeds, leading to a significant decrease in the percentage of germination (Meng *et al.*, 2017). Similarly, according to the findings of Velichko *et al.* (2019), a brief plasma jet treatment lasting 15-60 s induced the development of the wheat seed root system while having minimal effects on sprout length. However, when the treatment time was prolonged, the high temperature of the argon flow became the primary factor affecting the growth. The hot flow of argon negatively affected the potential for plant growth. According to Filatova *et al.* (2014), the shoot length increased when exposed to RF plasma treatment in a vacuum and the germination reached a maximum point.

The effect of plasma gas type on growth parameters has also been reported in some research. In a study conducted by Selcuk *et al.* (2008), it was demonstrated that the germination percentage, shoot height, and root length of the treated seeds were not affected by either air or SF_6 gas plasmas. Wheat roots and sprout length improvement were also reported in Dobrin *et al.* (2015). According to them, the roots of the plasma-treated seeds were found to be distributed more towards longer lengths compared to the untreated samples. Furthermore, there was a significant difference in the root-to-shoot ratio between the untreated wheat (0.88) and the treated seeds (1.2). The reason is likely the gentler plasma treatment, with an average discharge power of 2.7 W. As a result, the seeds are not damaged at this low power level. The effect of air cold plasma treatment on barley germination parameters was investigated by Feizollahi *et al.* (2020). The treatment of seeds for 1 and 10 minutes resulted in a decrease in the number of roots, shoot length, root surface area, and root length compared to the untreated samples. Although not significant, the 6-minute treatment showed some improvement in root volume, average root diameter, and germination percentage. Similarly, Mazandarani, Goudarzi, Ghafoorifard, and Eskandari (2020) reported that treatment of barley seeds with 80 W DBD plasma increases the shoot height and root length by 38.55% and 31.93% compared to the untreated seeds, respectively. Investigating the effect of three types of plasma including RF, microwave, and DBD in a vacuum and atmospheric pressure conditions on the growth and germination of corn seeds, Ahn *et al.* (2019) reported that corns treated with RF plasma had a higher growth rate under vacuum conditions. Chalise *et al.* (2023) presented results indicating that wheat seeds treated with 15 minutes of PAW treatment and 5 minutes of treatment with DBD exhibited longer root and spike lengths compared to the control sample. The PAW provided the necessary reactive nitrogen species for plant growth such that nitrate and nitrite species acted as fertilizers, which is the reason behind these results.

Biomass parameters

Cold plasma treatment can lead to notable alterations in various biomass parameters. These parameters include the dry weights of roots and sprouts, stem diameter, plant height, and plant growth efficiency. In a study conducted by Sera *et al.* (2010), it was found that the shoot dry weight increased significantly after 3 minutes of microwave plasma treatment compared to samples treated for 10, 20, and 40 minutes. Moreover, the highest root-to-shoot ratio was observed after 5 minutes of plasma exposure. In their study on DBD treatment, Guo *et al.* (2018) demonstrated that all biomass parameters reached their maximum values at different discharge voltages. Furthermore, Saberi, Sanavy, Zare, and Ghomi (2019) found that 180 s of plasma treatment increased the grain and spike yield by 58 and 75%, respectively, compared to the control sample.

UV radiation in plasma only affects the growth parameters during long-term treatment. Additionally, when exposed to hot air, temperatures below 70 °C do not have a significant impact on the seedling mass (Ghaly

& Sutherland, 1984). Therefore, the type of plasma treatment influences the sprout and root lengths, dry weight, and root-to-shoot ratio. In a study conducted by Henselová, Slováková, Martinka, and Zahoranová (2012), it was found that treating maize with a diffuse coplanar surface DBD in air resulted in a 21% increase in length, a 10% increase in fresh weight, and a 14% increase in dry weight. Compared to the untreated sample, a higher weight of roots and sprouts of wheat seeds treated with surface DBD plasma was obtained by Dobrin *et al.* (2015). Chalise *et al.* (2023) showed that the growth parameters of wheat seed, including spike length, fruit number, and root length were improved through direct plasma treatment and the utilization of PAW. Moreover, increasing the duration of treatment led to higher concentrations of reactive species and a decrease in water pH, ultimately enhancing productivity. According to Hui *et al.* (2020), there was an increase in plant height growth, number of leaves, and fresh and dry weight in wheat plants treated with a combination of air and helium plasma in a vacuum setting, compared to the control group.

The growth and yield of wheat greatly depend on the number of leaves it possesses. Increasing the number of leaves enhances the plant's ability to absorb light energy, leading to improved organic matter synthesis efficiency. This is vital for the optimal growth of wheat and ultimately results in improved yield. In a study conducted by Jiang *et al.* (2014), wheat seeds were subjected to helium plasma treatment, and the researchers examined various growth parameters during the phonological growth stage of the wheat plants. The results showed that the treated plants exhibited significant improvements in plant height (21.8%), root length (11.0%), fresh weight (7.0%), stem diameter (9.0%), leaf area (13%), and leaf thickness (25.5%) compared to the control group. This suggests that the application of cold plasma treatment can enhance the growth of wheat. Furthermore, the treated wheat yielded 5.89% higher yield compared to the control group. Numerous studies have also examined the impact of cold plasma treatment on brown rice seeds. These studies consistently found that the treated seeds exhibited increased fresh weight and dry weight of shoots and roots, as well as higher growth efficiency compared to the control group (Amnuaysin *et al.*, 2018; Liu *et al.*, 2021; Park, Puligundla, & Mok, 2020).

Metabolic activities

The treatment of cold plasma and PAW also have an impact on the characteristics of the internal components of seeds or plants associated with alterations in metabolite activity. Chen *et al.* (2016) studied the changes in a-amylase and antioxidant activity and gamma-aminobutyric acid (GABA) of germinated brown rice after 3-kV DBD treatment. The increasing activities of ABTS and DPPH radicals, a-amylase, phenol, and GABA were recorded after a 24-hour germination time. Similarly, Park *et al.* (2020) also reported positive changes in DPPH, ABTS, and phenolic content of brown rice sprouts after jet plasma treatment. Researchers demonstrated that the penetration of active species through the porous seed coat inside the caryopses, where they interact with plant cells, is responsible for alterations in seed chemical properties including phenolic compound contents after plasma treatment (Sera *et al.*, 2010). Relatively high concentrations of phenolic compounds in germinated seeds may be attributed to the release of phenolic compounds bound to the cell wall, as the breakdown of the cell wall takes place during germination (Gujral, Sharma, Kumar, & Singh, 2012). During germination, a significant increase in free phenolic acid content and ferulic acid content of brown rice has been observed (Tian, Nakamura, & Kayahara, 2004).

The enhanced ability of DPPH radical scavenging may be attributed to the softening of the seed coat caused by oxidants derived from jet plasma and then the penetration of active species into the seed. This penetration may potentially benefit physiological reactions (Li *et al.*, 2017). Sookwong *et al.* (2014)

reported a decrease in the phenolic content of treated brown rice 72 and 96 h before germination. In addition, plasma processing may affect the activity of saccharolytic enzymes, potentially enhancing the production of free phenolic compounds that were partially dissolved and lost in the soaking water during the pre-germination process. High moisture in rice seeds can increase the risk of mold growth and reduce the rate of rice germination. The study of Guo *et al.* (2023) indicated that plasma treatment had no significant impact on the moisture content of rice grains during the 8-minute treatment period. Also, the electrical conductivity of rice grain leachate, which is a crucial factor in determining cell membrane permeability, showed a slight increase after a 6-minute plasma treatment.

Chen, Hung, Lin, and Liou (2015) suggested that the improvement of brown rice quality during the 3-month storage is related to the reduction of fatty acid and α-amylase of samples treated with 3–kV plasma. The reduction of oxidative damage in wheat grain tissues treated with Ar/O_2 and Ar/Air plasma through the positive regulation of antioxidant enzymes SOD and CAT and their related genes was reported by Kabir *et al.* (2019). According to research by Los *et al.* (2019), 180 s of direct plasma treatment caused an acceptable increase in nitrite and nitrate levels, an increase in titratable total acidity content, and an increase in malondialdehyde wheat grain aldehyde. After treating wheat seeds with DBD plasma, Li *et al.* (2017) observed an increase in the levels of osmotic adjustment products, proline, and soluble sugars in wheat seedlings. They also noted a decrease in malondialdehyde content. Furthermore, the activity of superoxide dismutase and peroxidase in the treated samples also showed an increase. Also, according to research by Wang *et al.* (2023), a 3-minute treatment of wheat seeds with PAW enhanced the photosynthetic pigments, free amino acids, total phenolic content, protein content, antioxidant activity, enzyme activity, and mineral content of seeds grown for 14 days. Table 1 presents an overview of the types of cereals and the parameters studied after plasma treatment.

Table 1- Summary of studies conducted on cereal seeds after treatment with cold plasma and PAW. Abbreviations: alternating current (AC); radio frequency (RF); total phenolic compounds (TPC); antioxidant activity (DPPH); gamma-aminobutyric acid (GABA); scanning electron microscope (SEM); malondialdehyde (MDA)

Cereal	Plasma source/device	Studied parameters	References
Brown rice, cultivars: ST1, PL1, KDML 105, RD 6, NS, LP	DBD (100-200 W, RF, 25-300 s, argon)	Germination percentage, root length, seedling height, TPC, vitamin E, phytosterols, triterpenoids, and anthocyanins	(Yodpitak *et al.*, 2019)
Brown rice, cultivars: KhaoDawk Mali 105	DBD (5.5 kHz, 18 kV, 10-60 s, air)	Shoot length, fresh and dry weight of shoot and roots, carotenoid, chlorophyll a, and chlorophyll b	(Amnuaysin *et al.*, 2018)
Brown rice, cultivar: Taikeng 9	DBD (high voltage DC, 1–3 kV, 1.2 mA, 800 Pa, 10 minutes, air)	Germination and vigor of the seedlings, GABA, DPPH, water uptake, α-amylase, and TPC	(Chen *et al.*, 2016)
Brown rice, cultivar: Riceberry	Jet (400 kHz, 3–5 kV, 10-14 W, 5-10 s, argon and oxygen)	TPC, GABA, germination rates, and relative quantities of chemicals	(Sookwong *et al.*, 2014)
Brown rice, cultivar: NSCI RC298	Jet (high voltage AC, 15 kV, 60 Hz, air)	SEM images, germination percent, and germ lengths	(Penado *et al.*, 2017)

Brown rice, cultivar: not specified	Jet (0-40 W, 50 -600 kHz, 10 kV, RF, argon)	Colony count of *Aspergillus flavus*	(Suhem, Matan, Nisoa, & Matan, 2013)
Brown rice, cultivar: Chindeul	DBD (15 kHz, 250 W, 5-20 minutes, air)	Aerobic bacterial count, *Bacillus cereus*, *Bacillus subtilis*, *E coli*, color changes, pH, water uptake, α-amylase activity, and hardness	(Lee *et al.*, 2016)
Brown rice, cultivar: not specified	Jet (high voltage DC, 20 kV, 58 kHz, 1.5 A, 0-10 minutes, air)	DPPH, ABTS, TPC, weight of seedlings, length of seedlings, α- amylase, and β- amylase activity	(Park *et al.*, 2020)
Rice grain, cultivar: Late indica	DBD (high voltage AC, 25 kV, 2-8 minutes)	Ochratoxin A, deoxynivalenol, electrical conductivity, MDA, seed germination, moisture content, starch content, globulin, α- amylase, albumin, prolamin, and gluten	(Guo *et al.*, 2023)
Parboiled rice, cultivar: Sb Boiled Aiyre	DBD (13.56 MHz, 30-50 W, 5-15 minutes, 0.15 mbar, air)	Moisture content, fat, protein, ash, carbohydrates, cooking time, water uptake, cooking loss, hardness, cohesiveness, color, and whiteness index	(Sarangapani *et al.*, 2015)
Brown rice, cultivar: Taikeng 9	DBD (high voltage DC, 1–3 kV, 1.2 mA, 6 Torr, 30 minutes, air)	Moisture, protein, lipid, ash, carbohydrate, cooking time, elongation ratio, width expansion ratio, water absorption, cooking loss, adhesiveness, hardness, brittleness, cohesiveness, elasticity, and chewiness	(Chen *et al.*, 2012)
Brown rice, cultivar: Nan-jing 46	DBD (40-50 kV, 90-180 s, air)	Major volatile organic compounds, fatty acids, and color change	(Liu *et al.*, 2021)
Milled Rice, cultivar: four japonica rice and two indica rice	DBD (13.56 MHz, 80-120 W, 140 pa, 20-120 s, helium)	Cooking time, hardness, adhesiveness, elasticity, gruel solid loss, enthalpy of gelatinization, water contact angle, free fatty acid content, water absorption, and chalky rice rate	(Liu *et al.*, 2021)
Basmati rice, cultivar not specified	DBD (13.56 MHz, 30-40 W, 5-10 minutes, air)	Cooking time, water uptake, hardness, stickiness, contact angle, surface energy, and hydrophilic	(Thirumdas *et al.*, 2015)
Wheat seeds, cultivar: not specified	Jet (RF 13.56 MHz, 300W, 15-300 s, argon) and DBD (22.5 kHz, 30 W, 2-10 s, argon)	Average length, dry weights of roots and sprouts, germination time, water imbibition, and contact angle	(Velichko *et al.*, 2019)
Wheat seeds, cultivar: not specified	Glow discharge (1 kHz, 20 kV, 500 mTorr, 300 W, 30 s-30 min, air or SF_6)	Inactivation of *Aspergillus spp.* and *Penicillium spp. and shoot height*	(Selcuk *et al.*, 2008)
Wheat seeds, cultivar: not specified	Surface DBD (50 Hz, sinusoidal voltage, air)	Roots and sprouts length and dry weight, number of roots, and contact angle	(Dobrin *et al.*, 2015)
Wheat seeds, cultivar: not specified	PAW (high voltage DC, 0–15 kV, 5-15 minutes, air) and DBD (50 Hz, 0–45 kV, 1-5 minutes, air)	Germination rate, contact angle, wettability, growth rate, germination potential, total number of fruits, root length, and spike length	(Chalise *et al.*, 2023)
Wheat seeds, cultivar: BARI Gom 22	Jet (10 Torrs, 5–10 kV, 3–8 kHz, 90 s, argon/air and argon/oxigen)	Root and shoot cadmium concentration, total soluble protein, enzymes SOD and CAT, SEM images, root and shoot length and dry weight, total chlorophyll, electrolyte leakage, and cell death	(Kabir *et al.*, 2019)
Wheat seeds, cultivar: Xiaoyan 22	DBD (50 Hz, 13 kV, 4 minutes, air)	Seed germination, osmotic products, lipid peroxidation, seedling growth, reactive oxygen species, DPPH, abscisic acid, and expression of drought-resistant genes under drought stress	(Guo *et al.*, 2017)

Wheat seeds, cultivar: Shannong 12	DBD (80-100 W, 130–160 Pa, 15 s, air and helium)	Seed germination, yield, and plant height	(Hui *et al.*, 2020)
Wheat seeds, cultivar: Ingenio	DBD (RF, 13.56 MHz, 50 Pa, 200 W, 30-90 s, oxygen)	Contact angle, surface morphology, surface roughness, chemical analysis of surface, water uptake, moisture, germination rate, α- amylase, root length, and number of seedlings	(Starič *et al.*, 2022)
Wheat seeds, cultivar: not specified	DBD (120 kV, 50 Hz, 30-180 s, air)	Contact angle, moisture content, pH and acidity, water uptake, MDA, hydrogen peroxide, nitrite and nitrate concentrations, and SEM	(Los *et al.*, 2019)
Wheat seeds, cultivar not specified	DBD (3×10^9 MHz, 60-100 W, 150 Pa, 15 s, helium)	Seed germination, yield, plant height, root length, fresh weight, stem diameter, leaf area, and leaf thickness	(Jiang *et al.*, 2014)
Wheat seeds, cultivar: Xiaoyan 22	DBD (50 Hz, 13 kV, 1-13 minutes, air)	Germination potential, germination rate, germination index, vigor index, root length, shoot length, fresh weight, dry weight of the seedlings, proline and soluble sugar contents of seedling, MDA, superoxide dismutase and peroxidase enzymes, and SEM	(Li *et al.*, 2017)
Wheat seeds, cultivar: Xiaoyan 22	DBD (13 kV, 50 Hz, oxygen, air, argon, and nitrogen)	Germination properties, shoot and root length, SEM, permeability, and seedlings soluble protein	(Meng *et al.*, 2017)
Wheat seeds, cultivar: Apache and Bezostaya 1	DBD (glow discharge, RF, 50 Pa, 200 W, 5-30 s and afterglow discharge, 600 W, 3-5 s, oxigen)	Germination, root growth, SEM, and fresh weight of seedlings	(Starič, Grobelnik Mlakar, & Junkar, 2021)
Wheat seeds, cultivar: not specified	glow discharge (1–6 kV, 3–5 kHz, 10 Torr, 3-15 minutes, air and air/O_2)	SEM, water absorption, seed germination, chlorophyll contents, growth Study, and yield	(Roy *et al.*, 2018)
Wheat seeds, cultivar: Jimai 23	PAW generated by plasma jet (high voltage AC, 7.0 kV, 600 W, 1-5 minutes, 98% Ar and 2% O_2)	Seed germination, pH, total soluble solids, color, vitamin C, soluble protein contents, pigments contents, enzyme activities of SOD, PPO and POD, TPC, DPPH, free amino acids, and mineral contents	(Wang *et al.*, 2023)
Wheat seeds, cultivar: Bari 21	DBD (10 Torr, 5–10 kV, 3–8 kHz, 1-12 minutes, air)	SEM, seed germination, shoots length, number of tiller, fresh and dry weight, roots length, enzyme activities of SOD, APX, relative gene of TaSOD, and TaCAT, H_2O_2 and NO concentration of root and shoot, total soluble protein and sugar, fat and moisture content, crude fiber, ash, and yield	(Hasan *et al.*, 2022)
Wheat seeds, cultivar: Eva	coplanar surface DBD (400 W, 10-600 s, air)	Germination rate, dry weight, vigor of seedlings, wettability, surface microflora, inactivation of *Fusarium nivale*, *F. culmorum*, *Trichothecium roseum*, *Aspergillus flavus*, and *A. clavatus*	(Zahoranová *et al.*, 2016)
Yellow dent corn hybrid	PAW generated by plasma jet (RF plasma 2.45 GHz, 800 W, 10 minutes, helium-air)	Germination, growth, and product yield	(Ahn *et al.*, 2019)
Dent yellow corn	DBD (50 Hz, 90 kV, 1-30 minutes, air and MA65)	SEM, NOx and ozone concentration, and aflatoxin level in corn	(Shi *et al.*, 2017)
Corn, cultivar not specified	(high voltage AC, 20 kHz, 3-10 minutes, helium)	Germination and growth rate	(Sidik *et al.*, 2018)

Raw barley grains	DBD (high voltage AC, 0–34 kV, 300 W, 2-10 minutes, air)	Reduction of deoxynivalenol, moisture content, measurements of ozone, nitrous gas, and hydrogen peroxide concentration, protein, glucan content, and germination rate	(Feizollahi *et al.*, 2020)
Barley seeds, cultivar: not specified	DBD (40-120 W, 15 s, air)	Germination parameters, SEM, water penetration, and effect of storage time	(Mazandarani *et al.*, 2020)
Wheat, cultivar: Ireland and barley with cultivar: United Kingdom	DBD (80 kV, 50 Hz, 5-20 minutes, air)	Inactivation of *Bacillus atrophaeus, E. coli, P. verrucosum, B. atrophaeus*, germination percentage, and quality properties	(Los *et al.*, 2018)

Limitations and future of cold plasma in the food industry

The introduction of any new technology into the food industry is challenging due to the perception that it is disruptive, risky, and difficult to implement in a mature and low-margin industry while facing the day-to-day pressure of staying competitive (Keener & Misra, 2016). Therefore, for atmospheric cold plasma to be successfully adopted in the food industry, it is important to consider several non-technical factors. The primary focus should be on the consumers' needs, as they desire to consume fresh and high-quality food without added chemical preservatives. Food safety and maintaining the consumers' confidence in a particular food category is established gradually and falls under the responsibility of manufacturers, distributors, processors, regulatory agencies, and retailers. Hence, the utilization of cold plasma technology in the food industry relies not only on ensuring food safety but also on satisfying the needs of consumers. Other factors that lead manufacturers, processors, and distributors to use cold plasma technology include (1) Potential extension of product shelf life and reduced consumer food waste; (2) Maximum preservation of food quality and decreased food processing and storage losses; (3) Low energy requirement, making it a more environmentally friendly option compared to current technology; (4) Reduced operational and maintenance expenses; (5) Improved food safety through the elimination of pesticide and chemical residues; and (6) Environmentally friendly technology that promotes sustainability, as generation of efficient plasma requires only air and electricity. There is a limitation of cold plasma technology in the case of high-fat foods, which is responsible for the formation of secondary metabolites. These metabolites have an impact on the shelf life of fat-rich foods (Sarangapani, Keogh, Dunne, Bourke, & Cullen, 2017). Some researchers also reported that the treatment of high-fat dairy food with cold plasma causes its oxidation (Coutinho *et al.*, 2018).

Conclusion

Thanks to its capability to operate in low-temperature conditions without causing any harm to the surface of the seed, cold plasma has gained significant popularity as a seed treatment method. Various methods are used to generate the cold plasma, which makes comparing different results somewhat difficult. This review presents a summary of the impacts of cold plasma on various types of cereal seeds. The text is made up of sections that describe the effect of plasma on seed and sprout decontamination, germination, surface property changes, growth and biomass parameters, and metabolic activities. This overview suggests that cold plasma may also have a strong presence in different agricultural sectors, particularly concerning applications for cereal seeds. Based on the reviewed works, it can be concluded that exposure to cold plasma or PAW has a significant impact on various properties of cereal seeds. Namely, germination begins with water absorption, and the ability to absorb water can be greatly affected by plasma activity. The surface properties and certain physiological parameters of seeds could also be modified. Oxidation processes by reactive species can

enhance water adsorption capability by improving seed coat wettability. Additionally, these processes may be linked to gas exchanges and electrolyte leakage in the seeds. Probably, cold plasma could effectively alter the dormancy of hard seeds by influencing seed permeability. Cold plasma can also have a positive impact on seed germination, growth, and the characteristics of seedlings. In addition, cold plasma can be used to decontaminate the surfaces of cereal seeds effectively. The findings presented in the text are summarized in Table 1. This table offers an overview of prior studies conducted on cereal family plant seeds using cold plasma.

To further explore the impact of plasma on cereal seeds, it is recommended to analyze the alterations in the surface morphology of plasma-treated cereal seeds. Additionally, it is important to examine the resulting products derived from cereals, such as flour, starch, oil, etc. Furthermore, assessing the long-term effectiveness of plasma treatment is crucial for controlling pests in stored grains.

Acknowledgments

We thank each of the authors of this article for their technical assistance.

Author Contribution Statement

Maryam Pourbaghe: Investigation, resources, data curation, writing (original draft), writing (review and editing). **Roghayeh Pourbagher:** Conceptualization, methodology, formal analysis, investigation, resources, data curation, writing (original draft), writing (review and editing), visualization. **Mohammad Hossein Abbaspour-Fard:** Conceptualization, project administration, writing (review and editing), data curation.

Competing Interests

The authors have no relevant financial or non-financial interests to disclose.

References

1. Adhikari, B., Adhikari, M., Ghimire, B., Adhikari, B. C., Park, G., & Choi, E. H. (2020). Cold plasma seed priming modulates growth, redox homeostasis and stress response by inducing reactive species in tomato (*Solanum lycopersicum*). *Free Radical Biology and Medicine*, *156*, 57-69. https://doi.org/10.1016/j.freeradbiomed.2020.06.003
2. Ahn, C., Gill, J., & Ruzic, D. N. (2019). Growth of plasma-treated corn seeds under realistic conditions. *Scientific reports*, *9*(1), 4355. https://doi.org/10.1038/s41598-019-40700-9
3. Ali, Q., Daud, M., Haider, M. Z., Ali, S., Rizwan, M., Aslam, N., Noman, A., Iqbal, N., Shahzad, F., & Deeba, F. (2017). Seed priming by sodium nitroprusside improves salt tolerance in wheat (*Triticum aestivum* L.) by enhancing physiological and biochemical parameters. *Plant Physiology and Biochemistry*, *119*, 50-58. https://doi.org/10.1016/j.plaphy.2017.08.010
4. Amnuaysin, N., Korakotchakorn, H., Chittapun, S., & Poolyarat, N. (2018). Seed germination and seedling growth of rice in response to atmospheric air dielectric-barrier discharge plasma. *Songklanakarin Journal of Science & Technology*, *40*(4).
5. Bormashenko, E., Grynyov, R., Bormashenko, Y., & Drori, E. (2012). Cold radiofrequency plasma treatment modifies wettability and germination speed of plant seeds. *Scientific Reports*, *2*(1), 741. https://doi.org/10.1038/srep00741
6. Butscher, D., Schlup, T., Roth, C., Müller-Fischer, N., Gantenbein-Demarchi, C., & von Rohr, P. R. (2015). Inactivation of microorganisms on granular materials: Reduction of Bacillus amyloliquefaciens endospores on wheat grains in a low pressure plasma circulating fluidized bed reactor. *Journal of Food Engineering*, *159*, 48-56. https://doi.org/10.1016/j.jfoodeng.2015.03.009
7. Butscher, D., Zimmermann, D., Schuppler, M., & von Rohr, P. R. (2016). Plasma inactivation of bacterial endospores on wheat grains and polymeric model substrates in a dielectric barrier

discharge. *Food Control*, *60*, 636-645. https://doi.org/10.1016/j.foodcont.2015.09.003
8. Chalise, R., Bhandari, P., Sharma, S., Basnet, S., Subedi, D. P., & Khanal, R. (2023). Enhancement of wheat yield by atmospheric pressure plasma treatment. *AIP Advances*, *13*(6). https://doi.org/10.1063/5.0156552
9. Chen, H. H., Chang, H. C., Chen, Y. K., Hung, C. L., Lin, S. Y., & Chen, Y. S. (2016). An improved process for high nutrition of germinated brown rice production: Low-pressure plasma. *Food Chemistry*, *191*, 120-127. https://doi.org/10.1016/j.foodchem.2015.01.083
10. Chen, H. H., Chen, Y. K., & Chang, H. C. (2012). Evaluation of physicochemical properties of plasma treated brown rice. *Food Chemistry*, *135*(1), 74-79. https://doi.org/10.1016/j.foodchem.2012.04.092
11. Chen, H. H., Hung, C. L., Lin, S. Y., & Liou, G. J. (2015). Effect of low-pressure plasma exposure on the storage characteristics of brown rice. *Food and Bioprocess Technology*, *8*, 471-477. https://doi.org/10.1007/s11947-014-1415-6
12. Coutinho, N. M., Silveira, M. R., Rocha, R. S., Moraes, J., Ferreira, M. V. S., Pimentel, T. C., Freitas, M. Q., Silva, M. C., Raices, R. S., & Ranadheera, C. S. (2018). Cold plasma processing of milk and dairy products. *Trends in Food Science & Technology*, *74*, 56-68. https://doi.org/10.1016/j.tifs.2018.02.008
13. Dobrin, D., Magureanu, M., Mandache, N. B., & Ionita, M. D. (2015). The effect of non-thermal plasma treatment on wheat germination and early growth. *Innovative Food Science & Emerging Technologies*, *29*, 255-260. https://doi.org/10.1016/j.ifset.2015.02.006
14. Fang, Z., Wang, X., Shao, R., Qiu, Y., & Edmund, K. (2011). The effect of discharge power density on polyethylene terephthalate film surface modification by dielectric barrier discharge in atmospheric air. *Journal of Electrostatics*, *69*(1), 60-66. https://doi.org/10.1016/j.elstat.2010.11.003
15. Feizollahi, E., Iqdiam, B., Vasanthan, T., Thilakarathna, M. S., & Roopesh, M. (2020). Effects of atmospheric-pressure cold plasma treatment on deoxynivalenol degradation, quality parameters, and germination of barley grains. *Applied Sciences*, *10*(10), 3530. https://doi.org/10.3390/app10103530
16. Fereydooni, M., & Alizadeh, H. H. A. (2022). Microscopic investigation of cold plasma effect on chickpea seed germination. *Journal of Agricultural Machinery*, *12*(2), 231-240. (in Persian with English abstract). https://doi.org/10.22067/jam.v12i2.88718
17. Filatova, I., Azharonok, V., Goncharik, S., Lushkevich, V., Zhukovsky, A., & Gadzhieva, G. (2014). Effect of RF plasma treatment on the germination and phytosanitary state of seeds. *Journal of Applied Spectroscopy*, *81*, 250-256. https://doi.org/10.1007/s10812-014-9918-5
18. Ghaly, T., & Sutherland, J. (1984). Heat damage to grain and seeds. *Journal of Agricultural Engineering Research*, *30*, 337-345. https://doi.org/10.1016/S0021-8634(84)80034-7
19. Godfray, H. C. J., Beddington, J. R., Crute, I. R., Haddad, L., Lawrence, D., Muir, J. F., Pretty, J., Robinson, S., Thomas, S. M., & Toulmin, C. (2010). Food security: the challenge of feeding 9 billion people. *Science*, *327*(5967), 812-818. https://doi.org/10.1126/science.1185383
20. Gómez-Ramírez, A., López-Santos, C., Cantos, M., García, J. L., Molina, R., Cotrino, J., Espinós, J., & González-Elipe, A. R. (2017). Surface chemistry and germination improvement of Quinoa seeds subjected to plasma activation. *Scientific Reports*, *7*(1), 5924. https://doi.org/10.1038/s41598-017-06164-5
21. Gujral, H. S., Sharma, P., Kumar, A., & Singh, B. (2012). Total phenolic content and antioxidant activity of extruded brown rice. *International Journal of Food Properties*, *15*(2), 301-311. https://doi.org/10.1080/10942912.2010.483617
22. Guo, J., He, Z., Ma, C., Li, W., Wang, J., Lin, F., Liu, X., & Li, L. (2023). Evaluation of cold plasma for decontamination of molds and mycotoxins in rice grain. *Food Chemistry*, *402*, 134159. https://doi.org/10.1016/j.foodchem.2022.134159

23. Guo, Q., Meng, Y., Qu, G., Wang, T., Yang, F., Liang, D., & Hu, S. (2018). Improvement of wheat seed vitality by dielectric barrier discharge plasma treatment. *Bioelectromagnetics*, *39*(2), 120-131. https://doi.org/10.1002/bem.22088
24. Guo, Q., Wang, Y., Zhang, H., Qu, G., Wang, T., Sun, Q., & Liang, D. (2017). Alleviation of adverse effects of drought stress on wheat seed germination using atmospheric dielectric barrier discharge plasma treatment. *Scientific Reports*, *7*(1), 16680. https://doi.org/10.1038/s41598-017-16944-8
25. Hasan, M., Sohan, M. S. R., Sajib, S. A., Hossain, M. F., Miah, M., Maruf, M. M. H., Khalid-Bin-Ferdaus, K. M., Kabir, A. H., Talukder, M. R., & Rashid, M. M. (2022). The effect of low-pressure dielectric barrier discharge (lpdbd) plasma in boosting germination, growth, and nutritional properties in wheat. *Plasma Chemistry and Plasma Processing*, *42*(2), 339-362. https://doi.org/10.1007/s11090-021-10217-z
26. Henselová, M., Slováková, Ľ., Martinka, M., & Zahoranová, A. (2012). Growth, anatomy and enzyme activity changes in maize roots induced by treatment of seeds with low-temperature plasma. *Biologia*, *67*, 490-497. https://doi.org/10.2478/s11756-012-0046-5
27. Hui, Y., Wang, D., You, Y., Shao, C., Zhong, C., & Wang, H. (2020). Effect of low temperature plasma treatment on biological characteristics and yield components of wheat seeds (*Triticum aestivum* L.). *Plasma Chemistry and Plasma Processing*, *40*, 1555-1570. https://doi.org/10.1007/s11090-020-10104-z
28. Jiang, J., He, X., Li, L., Li, J., Shao, H., Xu, Q., Ye, R., & Dong, Y. (2014). Effect of cold plasma treatment on seed germination and growth of wheat. *Plasma Science and Technology*, *16*(1), 54. https://doi.org/10.1088/1009-0630/16/1/12
29. Kabir, A. H., Rahman, M. M., Das, U., Sarkar, U., Roy, N. C., Reza, M. A., Talukder, M. R., & Uddin, M. A. (2019). Reduction of cadmium toxicity in wheat through plasma technology. *PLoS One*, *14*(4), e0214509. https://doi.org/10.1371/journal.pone.0214509
30. Keener, K., & Misra, N. (2016). Future of cold plasma in food processing. In *Cold plasma in food and agriculture* (pp. 343-360). Elsevier. https://doi.org/10.1016/B978-0-12-801365-6.00014-7
31. Kikuchi, K., Koizumi, M., Ishida, N., & Kano, H. (2006). Water uptake by dry beans observed by micro-magnetic resonance imaging. *Annals of Botany*, *98*(3), 545-553. https://doi.org/10.1093/aob/mcl145
32. Kusano, Y., Salewski, M., Leipold, F., Zhu, J., Ehn, A., Li, Z., & Aldén, M. (2014). Stability of alternating current gliding arcs. *The European Physical Journal D*, *68*, 1-9. https://doi.org/10.1140/epjd/e2014-50343-8
33. Lee, K. H., Kim, H. J., Woo, K. S., Jo, C., Kim, J. K., Kim, S. H., Park, H. Y., Oh, S. K., & Kim, W. H. (2016). Evaluation of cold plasma treatments for improved microbial and physicochemical qualities of brown rice. *LWT*, *73*, 442-447. https://doi.org/10.1016/j.lwt.2016.06.055
34. Lee, K. H., Woo, K. S., Yong, H. I., Jo, C., Lee, S. K., Lee, B. W., Oh, S. K., Lee, Y. Y., Lee, B., & Kim, H. J. (2018). Assessment of microbial safety and quality changes of brown and white cooked rice treated with atmospheric pressure plasma. *Food Science and Biotechnology*, *27*, 661-667. https://doi.org/10.1007/s10068-017-0297-6
35. Li, Y., Wang, T., Meng, Y., Qu, G., Sun, Q., Liang, D., & Hu, S. (2017). Air atmospheric dielectric barrier discharge plasma induced germination and growth enhancement of wheat seed. *Plasma Chemistry and Plasma Processing*, *37*, 1621-1634. https://doi.org/10.1007/s11090-017-9835-5
36. Liao, X., Cullen, P., Muhammad, A. I., Jiang, Z., Ye, X., Liu, D., & Ding, T. (2020). Cold plasma–based hurdle interventions: New strategies for improving food safety. *Food Engineering Reviews*, *12*, 321-332. https://doi.org/10.1007/s12393-020-09222-3

37. Liu, J., Wang, R., Chen, Z., & Li, X. (2021). Effect of cold plasma treatment on cooking, thermomechanical and surface structural properties of Chinese milled rice. *Food and Bioprocess Technology*, *14*(5), 866-886. https://doi.org/10.1007/s11947-021-02614-1
38. Liu, Q., Wu, H., Luo, J., Liu, J., Zhao, S., Hu, Q., & Ding, C. (2021). Effect of dielectric barrier discharge cold plasma treatments on flavor fingerprints of brown rice. *Food Chemistry*, *352*, 129402. https://doi.org/10.1016/j.foodchem.2021.129402
39. Los, A., Ziuzina, D., Akkermans, S., Boehm, D., Cullen, P. J., Van Impe, J., & Bourke, P. (2018). Improving microbiological safety and quality characteristics of wheat and barley by high voltage atmospheric cold plasma closed processing. *Food Research International*, *106*, 509-521. https://doi.org/10.1016/j.foodres.2018.01.009
40. Los, A., Ziuzina, D., Boehm, D., Cullen, P. J., & Bourke, P. (2019). Investigation of mechanisms involved in germination enhancement of wheat (*Triticum aestivum*) by cold plasma: Effects on seed surface chemistry and characteristics. *Plasma Processes and Polymers*, *16*(4), 1800148. https://doi.org/10.1002/ppap.201800148
41. Lutts, S., Benincasa, P., Wojtyla, L., Kubala, S., Pace, R., Lechowska, K., Quinet, M., & Garnczarska, M. (2016). Seed priming: new comprehensive approaches for an old empirical technique. *New Challenges in Seed Biology-basic and Translational Research Driving Seed Technology*, *46*.
42. Maghsoudi, H., Balvardi, M., Ganjovi, A., & Amir-Mojahedi, M. S. (2023). Investigating the Effect of Cold Plasma on some Chemical Properties of Date Fruits (*Phoenix dactylifera* L.). *Biomechanism and Bioenergy Research*, *2*(1), 56-67. https://doi.org/10.22103/BBR.2023.20459.1044
43. Mazandarani, A., Goudarzi, S., Ghafoorifard, H., & Eskandari, A. (2020). Evaluation of DBD plasma effects on barley seed germination and seedling growth. *IEEE Transactions on Plasma Science*, *48*(9), 3115-3121. https://doi.org/10.1109/TPS.2020.3012909
44. McDonald, M. B. (1994). Seed germination and seedling establishment. *Physiology and Determination of Crop Yield*, 37-60. https://doi.org/10.2134/1994.physiologyanddetermination.c3
45. Mendis, D., Rosenberg, M., & Azam, F. (2000). A note on the possible electrostatic disruption of bacteria. *IEEE Transactions on Plasma Science*, *28*(4), 1304-1306. https://doi.org/10.1109/27.893321
46. Meng, Y., Qu, G., Wang, T., Sun, Q., Liang, D., & Hu, S. (2017). Enhancement of germination and seedling growth of wheat seed using dielectric barrier discharge plasma with various gas sources. *Plasma Chemistry and Plasma Processing*, *37*, 1105-1119. https://doi.org/10.1007/s11090-017-9799-5
47. Nalwa, C., Thakur, A. K., Vikram, A., Rane, R., & Vaid, A. (2017). Studies on plasma treatment and priming of seeds of bell pepper (*Capsicum annuum* L.). *Journal of Applied and Natural Science*, *9*(3), 1505-1509. https://doi.org/10.31018/jans.v9i3.1392
48. Niemira, B. A. (2012). Cold plasma decontamination of foods. *Annual Review of Food Science and Technology*, *3*, 125-142. https://doi.org/10.1146/annurev-food-022811-101132
49. Nonogaki, H. (2014). Seed dormancy and germination—emerging mechanisms and new hypotheses. *Frontiers in Plant Science*, *5*, 233. https://doi.org/10.3389/fpls.2014.00233
50. Park, H., Puligundla, P., & Mok, C. (2020). Cold plasma decontamination of brown rice grains: Impact on biochemical and sensory qualities of their corresponding seedlings and aqueous tea infusions. *LWT*, *131*, 109508. https://doi.org/10.1016/j.lwt.2020.109508
51. Park, Y., Oh, K. S., Oh, J., Seok, D. C., Kim, S. B., Yoo, S. J., & Lee, M. J. (2018). The biological effects of surface dielectric barrier discharge on seed germination and plant growth with barley. *Plasma Processes and Polymers*, *15*(2), 1600056. https://doi.org/10.1002/ppap.201600056

52. Penado, K. N. M., Mahinay, C. L. S., & Culaba, I. B. (2017). Effect of atmospheric plasma treatment on seed germination of rice (*Oryza sativa* L.). *Japanese Journal of Applied Physics*, *57*(1S), 01AG08. https://doi.org/10.7567/JJAP.57.01AG08
53. Pérez-Pizá, M. C., Cejas, E., Zilli, C., Prevosto, L., Mancinelli, B., Santa-Cruz, D., Yannarelli, G., & Balestrasse, K. (2020). Enhancement of soybean nodulation by seed treatment with non–thermal plasmas. *Scientific Reports*, *10*(1), 4917. https://doi.org/10.1038/s41598-020-61913-3
54. Radjabian, T., Saboora, A., Hhasani, B., & Fallah-Hosseini, H. (2007). Effects of GA3 and chilling on seed germination of Ferula assa-foetida, as a medicinal plant. *Researches on Medicinal and Aromatic Plants of Iran*, *23*(3).
55. Ranieri, P., Sponsel, N., Kizer, J., Rojas-Pierce, M., Hernández, R., Gatiboni, L., Grunden, A., & Stapelmann, K. (2021). Plasma agriculture: Review from the perspective of the plant and its ecosystem. *Plasma Processes and Polymers*, *18*(1), 2000162. https://doi.org/10.1002/ppap.202000162
56. Rasooli, Z., Barzin, G., Mahabadi, T. D., & Entezari, M. (2021). Stimulating effects of cold plasma seed priming on germination and seedling growth of cumin plant. *South African Journal of Botany*, *142*, 106-113. https://doi.org/10.1016/j.sajb.2021.06.025
57. Ray, D. K., Mueller, N. D., West, P. C., & Foley, J. A. (2013). Yield trends are insufficient to double global crop production by 2050. *PloS one*, *8*(6), e66428. https://doi.org/10.1371/journal.pone.0066428
58. Roy, N., Hasan, M., Talukder, M., Hossain, M., & Chowdhury, A. (2018). Prospective applications of low frequency glow discharge plasmas on enhanced germination, growth and yield of wheat. *Plasma Chemistry and Plasma Processing*, *38*, 13-28. https://doi.org/10.1007/s11090-017-9855-1
59. Saberi, M., Sanavy, M., Zare, R., & Ghomi, H. (2019). Improvement of photosynthesis and photosynthetic productivity of winter wheat by cold plasma treatment under haze condition. *Journal of Agricultural Science and Technology*, *21*(7), 1889-1904. https://doi.org/20.1001.1.16807073.2019.21.7.8.9
60. Sabularse, V., Liuzzo, J., Rao, R., & Grodner, R. (1991). Cooking quality of brown rice as influenced by gamma irradiation, variety and storage. *Journal of Food Science*, *56*(1), 96-98. https://doi.org/10.1111/j.1365-2621.1991.tb07984.x
61. Sajib, S. A., Billah, M., Mahmud, S., Miah, M., Hossain, F., Omar, F. B., Roy, N. C., Hoque, K. M. F., Talukder, M. R., & Kabir, A. H. (2020). Plasma activated water: The next generation eco-friendly stimulant for enhancing plant seed germination, vigor and increased enzyme activity, a study on black gram (*Vigna mungo* L.). *Plasma Chemistry and Plasma Processing*, *40*, 119-143. https://doi.org/10.1007/s11090-019-10028-3
62. Sarangapani, C., Devi, Y., Thirundas, R., Annapure, U. S., & Deshmukh, R. R. (2015). Effect of low-pressure plasma on physico-chemical properties of parboiled rice. *LWT-Food Science and Technology*, *63*(1), 452-460. https://doi.org/10.1016/j.lwt.2015.03.026
63. Sarangapani, C., Keogh, D. R., Dunne, J., Bourke, P., & Cullen, P. (2017). Characterisation of cold plasma treated beef and dairy lipids using spectroscopic and chromatographic methods. *Food Chemistry*, *235*, 324-333. https://doi.org/10.1016/j.foodchem.2017.05.016
64. Selcuk, M., Oksuz, L., & Basaran, P. (2008). Decontamination of grains and legumes infected with Aspergillus spp. and Penicillum spp. by cold plasma treatment. *Bioresource Technology*, *99*(11), 5104-5109. https://doi.org/10.1016/j.biortech.2007.09.076
65. Sera, B., Spatenka, P., Šerý, M., Vrchotova, N., & Hruskova, I. (2010). Influence of plasma treatment on wheat and oat germination and early growth. *IEEE Transactions on Plasma Science*, *38*(10), 2963-2968. https://doi.org/10.1109/TPS.2010.2060728
66. Shi, H., Ileleji, K., Stroshine, R. L., Keener, K., & Jensen, J. L. (2017). Reduction of aflatoxin in corn by high voltage atmospheric cold plasma. *Food and Bioprocess Technology*, *10*, 1042-

1052. https://doi.org/10.1007/s11947-017-1873-8
67. Sidik, M. A. B., Buntat, Z., Nawawi, Z., Jambak, M. I., Buntat, Y., & Musa, F. N. (2018). *Effects of cold plasma treatment on the growth rate of corn and eggplant plants*. 2018 International Conference on Electrical Engineering and Computer Science (ICECOS), 441-446. https://doi.org/10.1109/ICECOS.2018.8605250
68. Sivachandiran, L., & Khacef, A. (2017). Enhanced seed germination and plant growth by atmospheric pressure cold air plasma: combined effect of seed and water treatment. *RSC advances*, *7*(4), 1822-1832. https://doi.org/10.1039/C6RA24762H
69. Sookwong, P., Yodpitak, S., Doungkaew, J., Jurithayo, J., Boonyawan, D., & Mahatheeranont, S. (2014). Application of oxygen-argon plasma as a potential approach of improving the nutrition value of pre-germinated brown rice. *Journal of Food and Nutrition Research*, *2*(12), 946-951. https://doi.org/10.12691/jfnr-2-12-14
70. Starič, P., Grobelnik Mlakar, S., & Junkar, I. (2021). Response of two different wheat varieties to glow and afterglow oxygen plasma. *Plants*, *10*(8), 1728. https://doi.org/10.3390/plants10081728
71. Starič, P., Mravlje, J., Mozetič, M., Zaplotnik, R., Šetina Batič, B., Junkar, I., & Vogel Mikuš, K. (2022). The influence of glow and afterglow cold plasma treatment on biochemistry, morphology, and physiology of wheat seeds. *International Journal of Molecular Sciences*, *23*(13), 7369. https://doi.org/10.3390/ijms23137369
72. Suhem, K., Matan, N., Nisoa, M., & Matan, N. (2013). Inhibition of Aspergillus flavus on agar media and brown rice cereal bars using cold atmospheric plasma treatment. *International Journal of Food Microbiology*, *161*(2), 107-111. https://doi.org/10.1016/j.ijfoodmicro.2012.12.002
73. Ten Bosch, L., Pfohl, K., Avramidis, G., Wieneke, S., Viöl, W., & Karlovsky, P. (2017). Plasma-based degradation of mycotoxins produced by Fusarium, Aspergillus and Alternaria species. *Toxins*, *9*(3), 97. https://doi.org/10.3390/toxins9030097
74. Thirumdas, R., Deshmukh, R., & Annapure, U. (2015). Effect of low temperature plasma processing on physicochemical properties and cooking quality of basmati rice. *Innovative Food Science & Emerging Technologies*, *31*, 83-90. https://doi.org/10.1016/j.ifset.2015.08.003
75. Tian, S., Nakamura, K., & Kayahara, H. (2004). Analysis of phenolic compounds in white rice, brown rice, and germinated brown rice. *Journal of agricultural and food chemistry*, *52*(15), 4808-4813. https://doi.org/10.1021/jf049446f
76. Velichko, I., Gordeev, I., Shelemin, A., Nikitin, D., Brinar, J., Pleskunov, P., Choukourov, A., Pazderů, K., & Pulkrábek, J. (2019). Plasma jet and dielectric barrier discharge treatment of wheat seeds. *Plasma Chemistry and Plasma Processing*, *39*, 913-928. https://doi.org/10.1007/s11090-019-09991-8
77. Wang, J., Cheng, J. H., & Sun, D. W. (2023). Enhancement of wheat seed germination, seedling growth and nutritional properties of wheat plantlet juice by plasma activated water. *Journal of Plant Growth Regulation*, *42*(3), 2006-2022. https://doi.org/10.1007/s00344-022-10677-3
78. Wang, Y., Thorup-Kristensen, K., Jensen, L. S., & Magid, J. (2016). Vigorous root growth is a better indicator of early nutrient uptake than root hair traits in spring wheat grown under low fertility. *Frontiers in Plant Science*, *7*, 865. https://doi.org/10.3389/fpls.2016.00865
79. Yodpitak, S., Mahatheeranont, S., Boonyawan, D., Sookwong, P., Roytrakul, S., & Norkaew, O. (2019). Cold plasma treatment to improve germination and enhance the bioactive phytochemical content of germinated brown rice. *Food Chemistry*, *289*, 328-339. https://doi.org/10.1016/j.foodchem.2019.03.061
80. Yong, H. I., Lee, S. H., Kim, S. Y., Park, S., Park, J., Choe, W., & Jo, C. (2019). Color development, physiochemical properties, and microbiological safety of pork jerky processed

with atmospheric pressure plasma. *Innovative Food Science & Emerging Technologies*, *53*, 78-84. https://doi.org/10.1016/j.ifset.2017.09.005

81. Zahoranová, A., Henselová, M., Hudecová, D., Kaliňáková, B., Kováčik, D., Medvecká, V., & Černák, M. (2016). Effect of cold atmospheric pressure plasma on the wheat seedlings vigor and on the inactivation of microorganisms on the seeds surface. *Plasma Chemistry and Plasma Processing*, *36*, 397-414. https://doi.org/10.1007/s11090-015-9684-z
82. Zulfiqar, F. (2021). Effect of seed priming on horticultural crops. *Scientia Horticulturae*, *286*, 110197. https://doi.org/10.1016/j.scienta.2021.110197

نشریه ماشین‌های کشاورزی
https://jame.um.ac.ir

مقاله مروری

جلد ۱٤، شماره ۱، بهار ۱٤۰۳، ص ۱۰٤-۸۳

تکنیک پلاسمای سرد در کنترل آلودگی و بهبود فرآیندهای فیزیولوژیکی غلات (مروری)

مریم پورباقر[۱]، رقیه پورباقر[۲]، محمدحسین عباسپورفرد[۳*]

تاریخ دریافت: ۱۴۰۲/۰۷/۰۸
تاریخ پذیرش: ۱۴۰۲/۰۸/۱۰

چکیده

امروزه تقریباً نیمی از کل نیازهای غذایی انسان به‌ویژه در آسیا مستقیماً از غلات تأمین می‌شود و نزدیک به ۷۰ درصد از سطح زیرکشت جهان کـه یک میلیارد هکتار است را غلات اشغال می‌کنند. بنابراین یافتن روش‌های غیرمخرب برای افزایش کیفیت بذر در کشاورزی و صنعت بایـد توسـعه یابـد. پلاسمای سرد روشی جدید و کارآمد در بخش کشاورزی و غذایی است که می‌توان از آن برای غیرفعال کردن میکروارگانیسم‌های سطحی و تحریک بذر استفاده کرد. این بررسی خلاصه‌ای از اثربخشی درمان با پلاسمای سرد بر ویژگی‌های چهار گیاه مهم غلات: گندم، برنج، ذرت و جـو را ارائـه می‌کنـد. تمرکز بر روی اثرات این تیمار بر روی جوانه‌زنی بذر، تغییرات خواص سطحی و جذب آب بذر، پارامترهای رشد ریشه، طول سـاقه و نهـال، پارامترهـای زیست‌توده و فعالیت‌های متابولیکی است. با بررسی تحقیقات انجام‌شده توسط محققان مشاهده می‌شود که بذر غلات تیمارشده با پلاسمای سـرد دارای قدرت جوانه‌زنی، جذب آب، طول ساقه و اندام هوایی، راندمان رشد، وزن اندام هوایی و ریشه و فعالیت متابولیکی بهتـری بودنـد. ایـن بررسـی می‌توانـد روندهای بالقوه امیدوارکننده‌ای را در استفاده از پلاسما به‌عنوان روشی برای کاهش شیوع بیماری‌های مضر گیاهی که از طریق بـذر منتقـل می‌شـود و خواب دانه‌های سخت را کاهش دهد، ارائه دهد.

واژه‌های کلیدی: پلاسمای سرد، تیمار بذر، دانه غلات، ویژگی بیولوژیکی

۱- گروه مهندسی، دانشکده مهندسی کامپیوتر، موسسه آموزش عالی گلستان، گرگان، ایران
۲- گروه مهندسی بیوسیستم، دانشکده کشاورزی، دانشگاه فردوسی مشهد، مشهد، ایران
۳- استاد، گروه مهندسی بیوسیستم، دانشکده کشاورزی، دانشگاه فردوسی مشهد، مشهد، ایران
(*- نویسنده مسئول: Email: abaspour@um.ac.ir)

https://doi.org/10.22067/jam.2023.84647.1193

مندرجات

نشریه ماشین های کشاورزی

با شماره پروانه ۸۹/۱۲۶۳۹ **و درجه علمی – پژوهشی شماره** ۳/۱۱/۳۷۸۱ **از وزارت علوم، تحقیقات و فناوری**

۸۹/۶/۱۳ **۸۹/۳/۱۷**

"بر اساس مصوبه وزارت عتف از سال ۱۳۹۸، کلیه نشریات دارای درجه "علمی-پژوهشی" به نشریه "علمی" تغییر نام یافتند."

جلد ۱۴ شماره ۱ بهار ۱۴۰۳

صاحب امتیاز: دانشگاه فردوسی مشهد

مدیر مسئول: سید محمدرضا مدرس رضوی — استاد- گروه مکانیک دانشکده مهندسی (دانشگاه فردوسی مشهد)

سردبیر: محمدحسین عباسپور فرد — استاد- گروه مهندسی مکانیک بیوسیستم (دانشگاه فردوسی مشهد)

ناشر: دانشگاه فردوسی مشهد

مقالات این نشریه در پایگاه‌های معتبر زیر نمایه می‌شود:

AGRIS، Scopus، Web of Science: Emerging Sources Citation Index™ (ESCI)، CABI، DOAJ، EBSCO، Google scholar، Internet Archive، پایگاه استنادی جهان اسلام (ISC)**، سامانه نشریات علمی ایران و پایگاه اطلاعات علمی جهاد دانشگاهی** (SID)

پست الکترونیک: jame@um.ac.ir

مقالات این شماره در سایت http://jame.um.ac.ir **به‌صورت مقاله کامل نمایه شده است.**

این نشریه به تعداد ۴ شماره در سال و به‌صورت آنلاین منتشر می‌شود.

انجمن مهندسان مکانیک ایران

نشریه علمی
ماشین های کشاورزی

جلد۱۴ شماره ۱
سال ۱۴۰۳
(شماره پیاپی: ۳۱)
شاپا: ۶۸۲۹-۲۲۲۸

عنوان مقالات

مقالات پژوهشی

مقالات مروری